Turbulence and wind velocity profiles from adaptive optics telemetry: a general and scalable solution for extremely large telescopes

LAIDLAW, DOUGLAS,JOHN

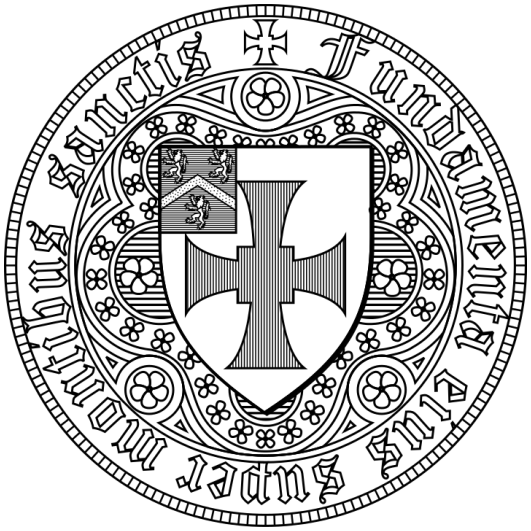

Durham University
Centre for Advanced Instrumentation

Turbulence and wind velocity profiles from adaptive optics telemetry: a general and scalable solution for extremely large telescopes

Author:
Douglas J. Laidlaw

Supervisors:
Dr Richard W. Wilson
Dr James Osborn

A thesis presented for the degree of
Doctor of Philosophy
January 16, 2020

Turbulence and wind velocity profiles from adaptive optics telemetry: a general and scalable solution for extremely large telescopes

Abstract

Advanced Adaptive Optics (AO) instruments on ground-based telescopes require accurate knowledge of the strength and velocity of atmospheric turbulence. Measuring these parameters as a function of altitude assists point spread function reconstruction, AO temporal control techniques, smart scheduling of science cases and is required by wide-field AO systems to optimise the reconstruction of an observed wavefront.

The variability of the atmosphere makes it important to have a measure of the turbulence profile in real-time. This measurement can be performed by iteratively fitting an analytically generated covariance matrix to the cross-covariance of Shack–Hartmann Wavefront Sensor (SHWFS) centroids. In this study we explore the benefits of reducing the number of cross-covariance data points and fitting to a covariance map Region of Interest (ROI). Both of these methods are based on the SLOpe Detection And Ranging (SLODAR) technique. A technique for using the covariance map ROI to measure and compensate for SHWFS misalignments is also introduced. We compare the accuracy of covariance matrix and map ROI optical turbulence profiling using simulated data from CANARY, an AO demonstrator on the 4.2 m William Herschel Telescope (WHT), La Palma. It is shown that the covariance map ROI optimises the accuracy of turbulence profiling. In addition, we show that the covariance map ROI reduces the fitting time for an Extremely Large Telescope-scale (ELT-scale) system by a factor of 72.

SLODAR spatio-temporal analysis can be used to visualise the wind velocity profile. However, the limited altitude-resolution of current AO systems makes it difficult to disentangle the movement of independent layers. We address this issue and introduce a novel technique that uses SLODAR data analysis for automated wind velocity profiling. Simulated data from CANARY is used to demonstrate the proficiency of the technique.

We apply our turbulence and wind velocity profiling techniques on-sky using data from both CANARY and the Adaptive Optics Facility (AOF). The AOF is on the 8.2 m Yepun telescope at the Very Large Telescope (VLT), Paranal. On-sky turbulence and wind velocity profiles from CANARY are compared to contemporaneous profiles from Stereo-SCIDAR, a dedicated high-resolution atmospheric profiler. Wind velocity profiles from CANARY and the AOF are compared to the European Centre for Medium-range Weather Forecasts (ECMWF). We also present AOF time sequences that show detailed examples of turbulence and wind velocity profiles at the VLT.

The software packages that we developed to collect all of the presented results are open-source. They can be configured to any tomographic AO system.

Supervisors: Dr Richard W. Wilson and Dr James Osborn

Acknowledgements

This research has been supported by the UK Programme for the European Extremely Large Telescope (ST/N002660/1).

I would like to thank the Centre for Advanced Instrumentation for granting me the opportunity to complete this research. More specifically, I am thankful to Dr Richard W. Wilson and Dr James Osborn for supervising the project. I would also like to give special thanks to Dr Tim Morris for being its unofficial supervisor. The insight and guidance I have received from my supervisors - both official and unofficial - has been central to the accomplishments of this work.

I dedicate this work to my parents and my brother. Thank you for your undying support.

Contents

Declaration

The work in this thesis is based on research carried out at the Centre for Advanced Instrumentation, the Department of Physics, University of Durham, England. No part of this thesis has been submitted elsewhere for any other degree or qualification and it is the sole work of the author unless referenced to the contrary in the text.

Some of the work presented in this thesis has been published in journals and conference proceedings. The relevant publications are listed below.

Journal publications

D. J. Laidlaw, J. Osborn, T. J. Morris, A. G. Basden, E. Gendron, G. Rousset, M. J. Townson, and R. W. Wilson. Automated wind velocity profiling from adaptive optics telemetry. Monthly Notices of the Royal Astronomical Society, 491, Issue 1, 1287-1294, 2019.

D. J. Laidlaw, J. Osborn, T. J. Morris, A. G. Basden, O. Beltramo-Martin, T. Butterley, E. Gendron, A. P. Reeves, G. Rousset, M. J. Townson, and R. W. Wilson. Optimizing the accuracy and efficiency of optical turbulence profiling using adaptive optics telemetry for extremely large telescopes. Monthly Notices of the Royal Astronomical Society, 483, Issue 4, 4341-4353, 2018.

P. Jia, J. Osborn, L. Kong, **D. J. Laidlaw**, C. Li, O. Farley, and G. Xue. Modelling synthetic atmospheric turbulence profiles with temporal variation using Gaussian mixture model. Monthly Notices of the Royal Astronomical Society, 480, Issue 2, 2466-2474, 2018.

J. Osborn, R. W. Wilson, M. Sarazin, T. Butterley, A. Chacón, F. Derie, O. J. D. Farley, X. Haubois, **D. J. Laidlaw**, M. Le Louarn, E. Masciadri, J Milli, J. Navarrete, and M. J. Townson. Optical turbulence profiling with Stereo-SCIDAR for VLT and ELT. Monthly Notices of the Royal Astronomical Society, 478, Issue 1, 825-834, 2018.

Conference proceedings

D. J. Laidlaw, J. Osborn, R. W. Wilson, T. J. Morris, T. Butterley, A. P. Reeves, M. J. Townson, E. Gendron, F. Vidal, and C. Morel. Turbulence profiling for adaptive optics

tomographic reconstructors. SPIE Astronomical Telescopes + Instrumentation, Adaptive Optics Systems V, 99093I, 2016.

L. Bardou, E. Gendron, G. Rousset, D. Gratadour, A. G. Basden, D. Bonaccini Calia, T. Buey, M. Centrone, F. Chemla, J-L. Gach, D. Geng, Z. Hubert, **D. J. Laidlaw**, T. J. Morris, R. M. Myers, J. Osborn, A. P. Reeves, M. J. Townson, and F. Vidal. Error breakdown of ELT-elongated LGS wavefront-sensing using CANARY on-sky measurements. SPIE Astronomical Telescopes + Instrumentation, Adaptive Optics Systems VI, 107031X, 2018.

A. G. Basden, L. Bardou, D. Bonaccini Calia, J-T. Buey, J. Castro, M. Centrone, F. Chemla, J-L. Gach, E. Gendron, D. Geng, Z. Hubert, G. Lombardi, **D. J. Laidlaw**, T. J. Morris, R. M. Myers, J. Osborn, A. P. Reeves, G. Rousset, A. Sevin, M. Townson, and F. Vidal. Closed loop operation with extremely elongated LGS spots in CANARY Phase D. SPIE Astronomical Telescopes + Instrumentation, Adaptive Optics Systems VI, 1070325, 2018.

O. J. D. Farley, J. Osborn, R. W. Wilson, T. Butterley, **D. J. Laidlaw**, M. J. Townson, T. Morris, M. Sarazin, F. Derie, M. Le Louarn, A. Chacón, X. Haubois, J. Navarrete, and J. Milli. Representative atmospheric turbulence profiles for ESO Paranal. SPIE Astronomical Telescopes + Instrumentation, Adaptive Optics Systems VI, 107032E, 2018.

List of figures

List of tables

Acronyms

AO Adaptive Optics

AOF Adaptive Optics Facility

CAPT CovAriance Parametrisation of optical Turbulence and SHWFS misalignments

CAW CovAriance parametrisation of Wind velocity

CCD Charge Coupled Device

CMM Covariance Mapping Matrix

DM Deformable Mirror

DSM Deformable Secondary Mirror

ECMWF European Centre for Medium-Range Weather Forecasts

ELT Extremely Large Telescope

ESO European Southern Observatory

FOV Field of View

GALACSI Ground Atmospheric Layer Adaptive Corrector for Spectroscopic Imaging

GLAO Ground-Layer Adaptive Optics

GMT Giant Magellan Telescope

GRAAL GRound-layer Adaptive optics Assisted by Lasers

GS Guide Star

HARMONI High Angular Resolution Monolithic Optical and Near-infrared Integral field spectrograph

HST Hubble Space Telescope

INT Isaac Newton Telescope

JWST James Webb Space Telescope

L3S Learn 3 Step

LGS Laser Guide Star

LMA Levenberg-Marquardt Algorithm

MCAO Multi-Conjugate Adaptive Optics

METIS Mid-infrared ELT Imager and Spectrograph

MICADO Multi-AO Imaging CAmera for Deep Observations

MOAO Multi-Object Adaptive Optics

MR Mapping Region

MUSE Multi-Unit Spectroscopic Explorer

NGS Natural Guide Star

ROI Region of Interest

RMS Root Mean Square

SCAO Single-Conjugate Adaptive Optics

SCIDAR SCIntillation Detection And Ranging

SHWFS Shack–Hartmann Wavefront Sensor

SLODAR SLOpe Detection And Ranging

SNR Signal-to-Noise Ratio

TMT Thirty Meter Telescope

VLT Very Large Telescope

WFM Wide Field Mode

WHT William Herschel Telescope

Nomenclature

ζ Angular distance from a science target.

L_0 Outer scale of atmospheric turbulence.

r_0 Fried parameter.

λ Wavelength.

h Altitude.

D Telescope primary mirror diameter.

θ GS angular separation.

$x_{\mathbf{sep}}$ Covariance map baseline in x.

$y_{\mathbf{sep}}$ Covariance map baseline in y.

γ GS separation angle in the FOV of the telescope.

$\mathbf{T}$ Transformation matrix for removing ground-layer isoplanatic turbulence.

$F_{\mathbf{md}}$ Mean logarithmic deviation.

$N_{\mathbf{L}}$ Number of turbulence profile layers.

$\mathbf{M}$ Target covariance matrix.

C_n^2 Refractive index structure constant.

L Length of covariance map ROI.

W Width of covariance map ROI.

M_0 Covariance map array.

δt Temporal offset.

$M_{\delta t}$ Temporally offset covariance map array.

$e_{\mathbf{s}}$ Theoretical CAW wind speed.

α Wind shear angle.

q Wind speed contrast.

$w_{\mathbf{s}}$ Wind speed.

$e_{\mathbf{d}}$ Theoretical CAW wind direction.

$w_{\mathbf{d}}$ Wind direction.

B Wind speed bias.

$A_{\mathbf{rms}}$ Wind speed root mean square deviation.

Ω The highest number of SHWFS frames that have been offset.

$N_{\mathbf{o}}$ The number of temporally offset covariance map arrays studied at one time.

$h_{\mathbf{max}}$ Maximum distance of NGS sub-aperture optical path intersection.

θ_0 Isoplanatic angle.

τ_0 Greenwood time delay.

ω Number of SHWFS frames that have been offset.

c The speed of light in a vacuum.

$n_{\mathbf{i}}$ Refractive index.

v The measured speed of light.

d An arbitary distance.

D_v Velocity structure function.

$v_{\mathbf{n}}$ Velocity of turbulence.

d_1 An exact point in space.

l_0 Inner scale of atmospheric turbulence.

C_v^2 Velocity structure constant.

D_n Index of refraction structure function.

z Optical path length.

ϕ Photon phase variation.

k Wavenumber.

D_ϕ Phase structure function.

β Zenith angle.

$\Psi^{\mathbf{K}}$ Kolmogorov power spectrum.

κ Spatial wavenumber.

j Arbitary length between the inner and outer scale of atmospheric turbulence.

$\Psi^{\mathbf{vK}}$ von Kármán power spectrum.

κ_0 Spatial wavenumber of outer scale atmospheric turbulence.

$K_{5/6}$ Bessel function of the third kind.

Γ Gamma function.

$\bar{h}$ Turbulence moment.

σ_ζ^2 Wavefront error.

x Horizontal cartesian coordinate.

y Vertical cartesian coordinate.

$\vec{\mathbf{e}}$ Vector of SHWFS centroids.

$\mathbf{K}$ Interaction matrix between SHWFS centroids and DM actuator commands.

$\vec{\mathbf{u}}$ Vector of DM actuator commands.

τ Elapsed time.

$\sigma^2_{\mathbf{time}}$ Mean square phase error after a time delay.

$\bar{w_{\mathbf{s}}}$ Wind speed moment.

$\hat{C}_{\mathbf{xy}}$ Cross-correlation between two time series variables.

X_n Time series variable.

Y_n Time series variable.

h_l Distance to NGS sub-aperture optical path intersection.

l Sub-aperture separation order.

$s_{\mathbf{w}}$ Distance between the centres of two adjacent SHWFS sub-apertures.

a_l Distance to LGS sub-aperture optical path intersection.

$n_{\mathbf{a}}$ Distance to LGSs.

$n_{\mathbf{d}}$ Number of SHWFS sub-apertures in one dimension.

C_ϕ Spatial covariance of phase.

σ_ϕ^2 Phase variance.

f Frame rate.

$s_{\mathbf{a}}$ SHWFS sub-aperture numbering.

$s_{\mathbf{b}}$ SHWFS sub-aperture numbering.

$\mathbf{A}$ Analytically generated covariance matrix.

$\mathbf{B}$ Analytically generated covariance matrix after the removal of ground-layer isoplanatic turbulence.

$b_{\mathbf{w}}$ Altitude spacing between the fitted layers during optical turbulence profiling.

$N_{\mathbf{m}}$ Number of calculations required to analytically generate a covariance matrix.

$k_{\mathbf{c}}$ Number of GS combinations.

$n_{\mathbf{s}}$ Number of SHWFS sub-apertures.

$m_{\mathbf{n}}$ Number of SHWFS sub-aperture baselines.

$N_{\mathbf{r}}$ Number of calculations required to analytically generate a covariance map ROI during CAPT 1.

$r_{\mathbf{n}}$ Number of sub-aperture separation pairings within one axis of the covariance map ROI along γ.

$s_{\mathbf{n}}$ Number of sub-aperture separation pairings within one axis of the covariance map ROI.

$R_{\mathbf{w}}$ Fraction of validated wind velocity measurements.

Δt Maximum temporal offset.

$m_{\mathbf{o}}$ Offset order.

— 1 —

Introduction

The technology that exists today allows us to study the cosmos in great detail. In the last couple of decades there have been tremendous discoveries made using advanced astronomical instrumentation. However, to answer some of the most profound questions about the universe, scientists require innovative upgrades to the current class of telescopes.

The diffraction-limited angular resolution of an optical telescope is inversely proportional to the diameter of its primary mirror. However, the resolution of a ground-based telescope is also limited by the blurring effect of atmospheric turbulence. To mitigate these effects, advanced ground-based telescopes now use Adaptive Optics (AO) instruments. The success of AO has led to the ongoing design and construction of the largest ground-based telescopes ever built. These telescopes are known as Extremely Large Telescopes (ELTs). The ELTs will advance astronomical knowledge and allow for detailed studies of subjects including the early universe, dark matter, dark energy and supermassive black holes. They will also make detailed observations of exoplanets. To assure ELT science goals are met, AO control techniques must be optimised.

1.1 Space and ground-based telescopes

One of the most anticipated telescopes is the 6.5 m (primary mirror diameter) James Webb Space Telescope (JWST; Clampin, 2008). It will be the largest space telescope ever built and is the successor to the 2.4 m Hubble Space Telescope (HST; Newman, 1990). However, there are a number of arguments for why the next generation of telescopes should be ground-based. To date, it is estimated that the total cost of the JWST will be nearly $10 billion (USD) and if it meets its launch date in 2021, it will have taken roughly 25 years to design and build. The JWST also has the added risk of having to make the journey into space. Not only does this endanger the telescope, but all of its optics must also remain aligned as it endures tremendous vibrations during take-off. After take-off, there is no viable solution to fixing or upgrading any of the JWST instruments. To maintain orbit positioning many space-based telescopes must also use propellant. This forces an upper limit on their lifetime. The JWST aims to have a mission time of 10 years.

Compared to a ground-based telescope, the greatest advantage of a space-based telescope is that it can make astronomical observations without having to look through atmospheric

turbulence. The atmosphere is opaque at many wavelengths but ground-based telescopes can still study a large range in the optical and infrared part of the spectrum (Hardy, 1998). Ground-based telescopes are primarily limited by atmospheric turbulence as it blurs and distorts the wavefront from a science target. For example, the spherical wavefront of light from a star will travel many light years before it reaches Earth. By the time it reaches a telescope like the JWST, its curved wavefront can be assumed flat and the only thing limiting the resolution of the image are the optics onboard. For a ground-based telescope, optical and infrared wavefronts will become perturbed as they travel through atmospheric turbulence. This results in a significant loss in image resolution. The source of this image blurring is the constant mixing of different temperatures throughout the atmosphere, causing the wavefront to travel through regions of varying refractive index (Hardy, 1998). The strength of air-temperature mixing changes with altitude and atmospheric turbulence typically occurs in discrete layers. A significant fraction of the integrated turbulence strength is in the ground-layer (Butterley et al., 2006; Osborn et al., 2010; Guesalaga et al., 2014; Martin et al., 2016a; Ono et al., 2016; Farley et al., 2018; Laidlaw et al., 2018). As it is blown by the wind, atmospheric turbulence is also non-stationary and, therefore, wavefront perturbations are continuously evolving.

1.2 Adaptive optics

To mitigate the effects of atmospheric turbulence, advanced ground-based optical telescopes now come equipped with AO systems (Tyson, 2010). These AO systems are capable of measuring the strength of wavefront perturbations across a 2D Field of View (FOV). Sources used to measure wavefront references are known as Guide Stars (GSs). This information is then relayed to one or more Deformable Mirrors (DMs) – situated in the optical path of the telescope – that change their shape to correct for the measured perturbations. The system works to restore the flat wavefront in real-time.

AO systems have been shown to significantly improve image resolution. In 2004, NACO, an AO instrument on the 8.2 m Yepun telescope at the Very Large Telescope (VLT), Paranal, provided the first-ever direct image of an exoplanet (Chauvin et al., 2004). NACO also performed the first-ever spectroscopic study of a directly observed exoplanet (Janson et al., 2010). The AO system at the Yepun telescope has since been upgraded and is now referred to as the Adaptive Optics Facility (AOF). The AOF is one of the most advanced AO systems ever built for ground-based astronomy. It will test future AO technologies as well as capture high resolution images of stars, galaxies, planets and exoplanets. The continuing success of AO means that, at certain wavelengths, ground-based telescopes can compete with those that are space-based. As ground-based telescopes can be easily accessed and therefore maintained, this has motivated the design of future telescopes that have the largest primary mirrors ever built. Within the next decade we will enter the era of ELTs. There are currently three ELTs under construction: the 24.5 m Giant Magellan Telescope (GMT), Las Campanas (Bouchez et al., 2018); the 30 m Thirty Meter Telescope (TMT), Mauna Kea (Boyer, 2018); and the 39.3 m European ELT, Cerro Armazones (Tamai et al.,

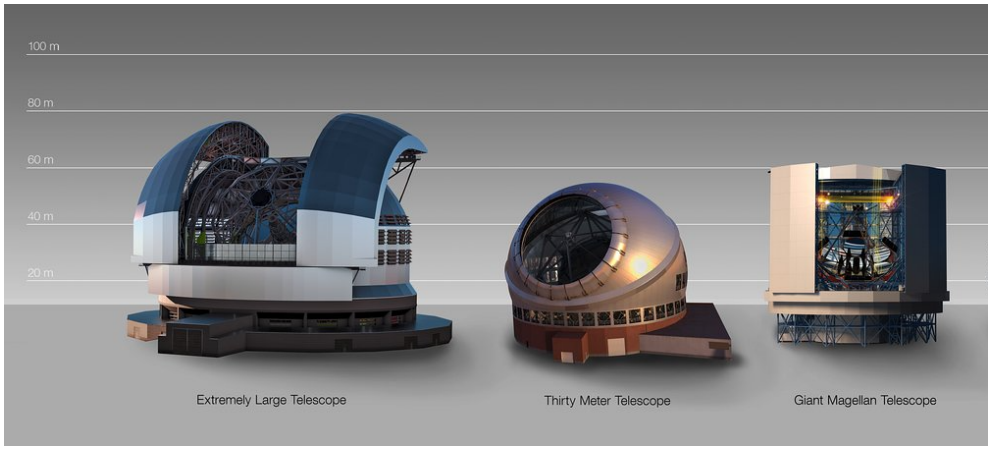

Figure 1.1: A conceptual drawing of the 24.5 m GMT, the 30 m TMT and the 39.3 m European ELT (ESO, 2017).

2018). Figure 1.1 shows a conceptual drawing of the three ELTs being constructed. They will all have sophisticated AO systems and it is planned that each ELT will see first-light before 2030.

1.3 Turbulence and wind velocity profiling

The GSs used for wavefront sensing typically have an angular separation from the science target. These observations require the system to calculate DM commands in the direction of the science target. For certain AO modes, a proposed technique for calculating these commands is to tomographically reconstruct the 3D volume of turbulence. This AO correction technique needs to know the vertical distribution of optical turbulence strength (Neichel et al., 2009). To optimise wavefront reconstruction it relies on having an accurate turbulence profile measurement (Villecroze et al., 2012; Martin et al., 2016b). The variability of the atmosphere also makes it important for this turbulence profile measurement to be continuously updated (Jia et al., 2018). To reduce temporal errors, predictive control algorithms can help mitigate the latency between the measurement of a wavefront and its successive DM correction. These algorithms commonly require both the turbulence and wind velocity profile (Sivo et al., 2014; Jackson et al., 2015). Additional applications for turbulence and wind velocity profiling include queue scheduling of science cases, performance monitoring, site characterisation and the forecasting of atmospheric parameters (Masciadri et al., 2013). Subsequent measurements can be used to validate and calibrate forecasts (Sivo et al., 2018).

It has been shown that turbulence and wind velocity profiles can be measured with the SCIntillation Detection And Ranging (SCIDAR; Vernin and Roddier, 1973) and the SLOpe Detection And Ranging (SLODAR; Wilson, 2002) techniques. The SCIDAR technique makes this measurement by studying atmospheric scintillation patterns from double star targets (Shepherd et al., 2013; Osborn et al., 2013; Osborn et al., 2018). The SLODAR

technique is of particular interest to the ELTs because it requires GS wavefront measurements and can therefore be used in tandem with certain AO systems (Cortés et al., 2012; Guesalaga et al., 2014; Martin et al., 2016a; Ono et al., 2016; Laidlaw et al., 2018; Laidlaw et al., 2019). However, ELT AO systems require thousands of measurements across each wavefront. This makes it a challenge for the ELTs to perform efficient turbulence and wind velocity profiling.

1.4 Synopsis

Chapter 2 discusses the recommended reading material for the proceeding chapters.

In Chapter 3 we introduce our SLODAR fitting technique for turbulence profiling. Using wavefront sensor data from individual GSs, we are able measure the optical turbulence profile as well as wavefront sensor misalignments. Simulated data from CANARY, an AO demonstrator for ELT-scale technologies on the 4.2 m William Herschel Telescope (WHT), La Palma, is used to test the accuracy of the fitting algorithm. We investigate how we can optimise both the accuracy and efficiency of our turbulence profiling technique. The developed algorithm is shown to be applicable to an ELT-scale AO system.

In Chapter 4 we introduce a novel fitting technique for automated wind velocity profiling from SLODAR data analysis. Simulated data from CANARY is used to demonstrate the proficiency of the technique. We consider how robust the fitting algorithm is when measuring profiles that are experiencing wind shear.

In Chapter 5 our turbulence and wind velocity profiling techniques are used to study on-sky data from CANARY and the AOF. The results from CANARY are compared to contemporaneous profiles that were measured using the SCIDAR technique. Wind velocity profile measurements from CANARY and the AOF are compared to the European Centre for Medium-range Weather Forecasts (ECMWF). We also show time sequences from the AOF, demonstrating why turbulence and wind velocity profile measurements need to be updated regularly. The algorithms that we developed to complete this study have been implemented in an open-source Python package. This open-source package has analysed data from both CANARY and the AOF, and can be configured to recover astro-meteorological parameters from any tomographic AO system.

Chapter 6 summarises the conclusions drawn from this study. Future work is also discussed.

— 2 —

Theoretical considerations

2.1 Atmospheric turbulence

As the Sun heats the Earth, solar radiation is transferred to the wind. The transfer of solar radiation into the atmosphere is non-uniform. Therefore, individual pockets of air can have a range of energies. A higher energy implies that the air is less dense, i.e. there are less gaseous elements occupying a given space. If photons (light particles) pass through a region of zero density, i.e. a vacuum, they will travel at the speed of light, c. To a good approximation, this means that light from celestial objects is unperturbed as it travels through outer space. However, in a non-zero density medium, photons will interact with the surrounding matter and travel slower than the speed of light. The ratio for how fast light propagates through a medium is known as its refractive index and is given by

$$n_{\mathrm{i}} = \frac{c}{v} \tag{2.1}$$

v is the measured speed of the photons. In air, n_{i} increases with its density. Therefore, light from a celestial object traverses many different regions of refractive index as it travels through the atmosphere. This causes perturbations across its once-flat wavefront. If a celestial object is monitored by a ground-based telescope, sections of its wavefront will arrive at different times and the image will appear distorted.

2.1.1 Kolmogorov theory

A widely accepted model for the statistical properties of fully-developed turbulence was proposed by Kolmogorov in 1941 (Kolmogorov, 1941). The proposal studied the mean-square velocity difference between two points in space separated by an arbitrary distance, d. Kolmogorov then made three assumptions about the local atmosphere: it is isotropic, homogenous and incompressible. The third assumption implies that the divergence of its flow velocity is zero. This allows for the dynamics of the atmosphere to have the velocity structure function,

$$D_v(d) = \left\langle [v_{\mathrm{n}}(d_1 + d) - v_{\mathrm{n}}(d_1)]^2 \right\rangle, \tag{2.2}$$

where v_{n} and d_1 are the velocity of the turbulence and a point in space, respectively.

The atmosphere can be modelled as discrete layers of turbulence at a range of altitudes. Within each layer, energy is injected at the largest spatial scale - the outer scale, L_0. The

outer scale breaks down to smaller and smaller sizes before reaching the inner scale, l_0. At the inner scale, energy is lost to the friction between gaseous elements. If d is within the inertial range, i.e. $l_0 < d < L_0$, then

$$D_v(d) = C_v^2 d^{2/3}. \tag{2.3}$$

C_v^2 is a measure of the energy in the turbulence and is known as the velocity structure constant.

The index of refraction structure function is similar to Equations 2.2 and 2.3, and is given by (Tatarskii, 1961)

$$D_n(d) = \left\langle [n_\mathrm{i}(d_1 + d) - n_\mathrm{i}(d_1)]^2 \right\rangle = C_n^2 d^{2/3}. \tag{2.4}$$

C_n^2 is the refractive index structure constant and it details the strength of atmospheric turbulence. It should be noted that the value of C_n^2 is not always a constant - it varies in both time and space throughout the atmosphere.

2.1.2 The Fried parameter

Along an optical path length, z, the phase delay is given by

$$\phi = k \int n_\mathrm{i}(z) dz. \tag{2.5}$$

For light coming from a celestial object that is observed by a ground-based telescope, z is the propagation distance through atmospheric turbulence. k is the wavenumber and is equal to $2\pi/\lambda$, where λ is the wavelength being observed. The phase structure function can be calculated using the same process outlined in Section 2.1.1 such that

$$D_\phi(d) = \left\langle [\phi(d_1 + d) - \phi(d_1)]^2 \right\rangle. \tag{2.6}$$

Equations 2.5 and 2.6 can be used to show that (Roddier, 1999)

$$D_\phi(d) = 2.91 k^2 \sec(\beta) d^{5/3} \int C_n^2(h) dh, \tag{2.7}$$

where h is the altitude above the telescope and β is the zenith angle, i.e. $\sec(\beta)$ is the air mass. The Fried parameter (Fried, 1965), r_0, was introduced to characterise the strength of integrated turbulence. It can simplify Equation 2.7 such that

$$D_\phi(d) = 6.88 \left(\frac{d}{r_0} \right)^{5/3}, \tag{2.8}$$

where

$$r_0 = \left[0.42 k^2 \sec(\beta) \int C_n^2(h) dh \right]^{-3/5}. \tag{2.9}$$

The resolution of a telescope will be limited by atmospheric effects if the diameter of its primary mirror, D, is larger than the Fried parameter. When $D > r_0$, the telescope will have the effective resolution of a telescope with $D = r_0$. Typical r_0 values at $\lambda = 0.5\,\mu$m are around 0.1 m (Laidlaw et al., 2018). However, its exact value can vary greatly throughout the night (Osborn et al., 2018).

2.1.3 Spatial power spectra

The Kolmogorov power spectrum for refractive index fluctuations can be written as (Tatarskii, 1961)

$$\Psi^{\mathrm{K}}(\kappa) = 0.033 C_n^2 \kappa^{-11/3}. \tag{2.10}$$

κ is the spatial wavenumber and is equal to $2\pi/j$, where $l_0 < j < L_0$. The von Kármán power spectrum was introduced to constrain the model with a finite outer scale and is given by

$$\Psi^{\mathrm{vK}}(\kappa) = 0.033 C_n^2 \left(\kappa^2 + \kappa_0^2\right)^{-11/6}. \tag{2.11}$$

κ_0 is the value of $2\pi/L_0$. It is currently thought that, in the free atmosphere, L_0 is on the order of 10 to 100 m (Ziad et al., 2004; Maire et al., 2007). The modified von Kármán power spectrum constrains the Kolmogorov model to have a finite inner scale. However, it is believed that the inner scale is on the order of 0.1 to 1 cm (Tyson, 2010). This study concentrates on telescopes that have primary mirror diameters greater than or equal to 4.2 m. Therefore, the effects of the inner scale are negligible throughout. For the von Kármán model, Equation 2.8 has been shown to have the analytical expression (Tokovinin, 2002)

$$D_\phi(d) = \left(\frac{L_0}{r_0}\right)^{5/3} \times \frac{\Gamma(11/6)}{2^{11/6}\pi^{8/3}} \left[\frac{24}{5}\Gamma\left(\frac{6}{5}\right)\right]^{5/6} \times \left[\frac{\Gamma(5/6)}{2^{1/6}} - \left(\frac{2\pi d}{L_0}\right)^{5/6} K_{5/6}\left(\frac{2\pi d}{L_0}\right)\right]. \tag{2.12}$$

Γ is the gamma function and $K_{5/6}$ is the modified Bessel function of the third kind.

2.2 Principles of adaptive optics

2.2.1 Guide stars

Atmospheric wavefront perturbations can be measured when a ground-based telescope uses a wavefront sensor (see Section 2.2.2) to monitor a bright object in the sky. These objects are commonly referred to as Guide Stars (GSs).

2.2.1.1 Natural guide stars

Stars are categorised as Natural Guide Stars (NGSs) and can be treated as point sources. Science targets are not always bright point sources and so, to measure the wavefront perturbations across a science target, nearby NGSs are often used. However, not all science targets have appropriate NGS asterisms. For example, there might be a large angular distance between a science target and the nearest NGS (see Section 2.2.1.3 and Figure 2.2). The lack of suitably bright NGSs means that only a fraction of the night sky is available to NGS Adaptive Optics (AO) systems.

Figure 2.1: Photograph of the 4-LGS system of the AOF on the 8.2 m Yepun telescope at the VLT, Paranal (Kamphues, 2016).

2.2.1.2 Laser guide stars

To increase sky-coverage, advanced AO systems can employ Laser Guide Stars (LGSs). The two main types of LGSs are Rayleigh and sodium (Morris et al., 2014; Oberti et al., 2018). This study only considers sodium LGSs. These lasers are launched at the ground and have a wavelength of 589.2 nm. Atoms in the sodium layer of the mesosphere - at an altitude of approximately 90 km - are excited by these photons, creating an artificial star. As the photons from the laser are refracted by atmospheric turbulence during uplink, the artificial stars created do not provide useful tip-tilt information. A nearby NGS is required to measure tip-tilt. However, as these are low-order aberrations and can therefore be observed more easily than high-order aberrarions, a faint NGS can be used. The 4-LGS system of the Adaptive Optics Facility (AOF) at the Very Large Telescope (VLT), Paranal, is shown in Figure 2.1.

Sodium LGSs are relatively close to the telescope (roughly 90 km away at zenith) and so their projected pupil size gets smaller with altitude. This is referred to as the cone effect (see Section 2.3.3). The sodium layer of the mesosphere is approximately 10 km thick and so LGSs can also appear elongated. The length of LGS elongation is dependent on the diameter of the telescope primary mirror and the angle at which they are viewed from. The largest aperture we use to study LGSs is the 4-LGS system of the AOF on the 8.2 m Yepun telescope. LGS elongation will not significantly impact the data analysis routines performed during this study (Bardou et al., 2018; Basden et al., 2018).

2.2.1.3 Isoplanatic angle

An angular distance between a science target and a GS results in their wavefronts propagating through different volumes of atmospheric turbulence. This is illustrated for a NGS system in Figure 2.2. The similarity between their wavefronts is related to the size of their separation angle, ζ. For a theoretical Root Mean Square (RMS) wavefront error of

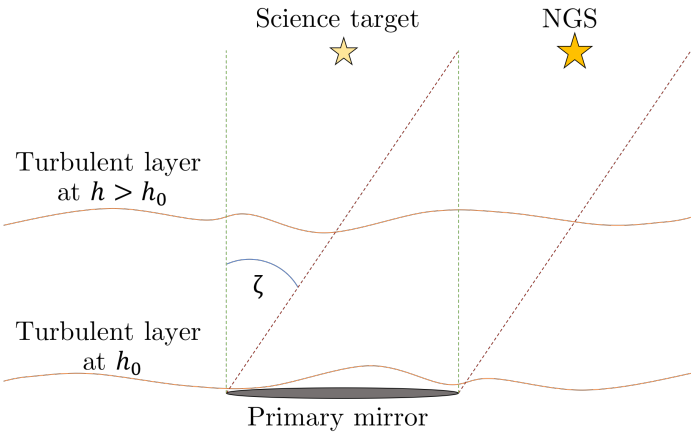

Figure 2.2: Origin of anisoplanatism. NGS and science target wavefronts propagate through different volumes of turbulence at $h > h_0$, where h_0 is the altitude of the ground-layer. The angular distance from the science target is given by ζ.

1 radian, the separation angle is referred to as the isoplanatic angle, θ_0. The isoplanatic angle is equal to (Roddier, 1999)

$$\theta_0 = \frac{0.314 r_0}{\bar{h} \sec \beta}. \tag{2.13}$$

In Equation 2.13, $\bar{h}$ is the turbulence moment, where

$$\bar{h} = \left[\frac{\int_0^\infty C_n^2(h) h^{5/3} dh}{\int_0^\infty C_n^2(h) dh} \right]^{3/5}. \tag{2.14}$$

The isoplanatic angle is therefore dependent on r_0, the zenith angle, β, and the shape of the turbulence profile. An expression for the wavefront error, σ_ζ^2, can be written as a function of the angular distance from the science target, ζ, such that (Roddier, 1999)

$$\sigma_\zeta^2(\zeta) = (\zeta/\theta_0)^{5/3}. \tag{2.15}$$

At the VLT it has been shown that, at $\lambda = 0.5\,\mu$m, typical values for θ_0 are between 1 and 2 arcseconds (Osborn et al., 2018).

2.2.2 Shack-Hartmann wavefront sensor

A Shack-Hartmann Wavefront Sensor (SHWFS) can be used to measure atmospheric wavefront perturbations across the telescope aperture. It uses a lenslet array, i.e. a grid of many small lenses, that is optically conjugate to the telescope pupil. We refer to these lenslets as sub-apertures. If a SHWFS is monitoring a GS then each sub-aperture focusses a section of the incoming wavefront down to a spot. An illustration of this is shown in Figure 2.3. If there is a plane wavefront then the spots will have zero displacement and will form a regular grid. However, the grid will no longer be regular when the SHWFS is monitoring a perturbed wavefront. By imaging these spots onto a detector - commonly a Charge Coupled

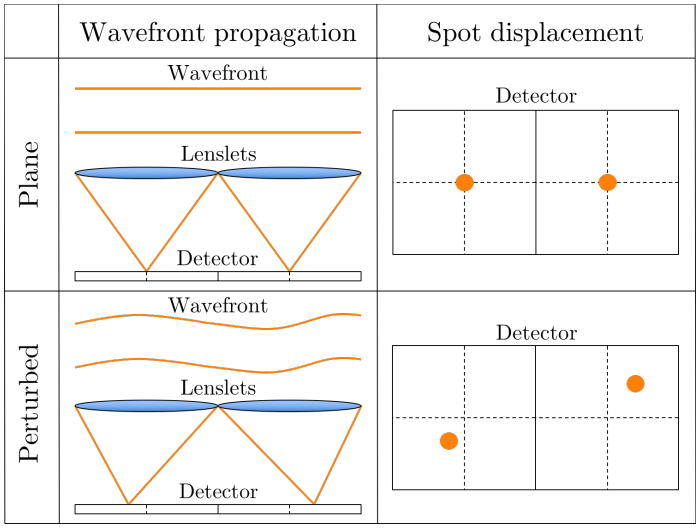

Figure 2.3: SHWFS lenslets measuring tip-tilt aberrations across a wavefront. The illustration shows the propagation of a plane wavefront (top left) and its zero spot displacement (top right). When the wavefront is perturbed, e.g. by atmospheric turbulence (bottom left), the spots have non-zero displacement (bottom right).

Device (CCD) - x and y spot displacement can be calculated using a centroiding algorithm. These centroiding calculations produce orthogonal measurements of the wavefront gradient across each sub-aperture.

An example of a SHWFS lenslet array is shown in Figure 2.4. This 7×7 SHWFS (dimensions in sub-apertures) has the same layout as the SHWFSs used on-sky by CANARY, an AO demonstrator on the 4.2 m William Herschel Telescope (WHT), La Palma. Sub-apertures that have insufficient illumination are set as inactive. Sub-aperture 25 is inactive because its light-path is blocked by the central obscuration, i.e. the secondary mirror.

2.2.3 Deformable mirrors

The Deformable Mirror (DM) is responsible for correcting phase aberrations and restoring a plane wavefront. It has a reflective surface that can change its shape through the push and pull of actuators. The largest possible actuator displacement is referred to as its stroke. The DM actuators are behind its surface and receive their commands from a reconstruction algorithm (see Section 2.2.4). If the DM is applying zero correction then its actuators are said to be in their rest position.

To perform wavefront correction one or more DMs are placed in the optical relay. A popular choice today is to replace the secondary mirror with a DM. These DMs feature large stroke and because of their relatively large diameter, they can contain a high number of actuators. This optical component has been adopted by the AOF and its secondary mirror is instead referred to as a Deformable Secondary Mirror (DSM; Oberti et al., 2018). An illustration of how a DSM can restore a plane wavefront is shown in Figure 2.5.

1	2	3	4	5	6	7
8	9	10	11	12	13	14
15	16	17	18	19	20	21
22	23	24	25	26	27	28
29	30	31	32	33	34	35
36	37	38	39	40	41	42
43	44	45	46	47	48	49

Figure 2.4: Pupil mask showing the active sub-apertures for a 7×7 SHWFS conjugate to the pupil of a telescope (grey). Inactive sub-apertures are also shown (white). Sub-apertures that have insufficient illumination are set as inactive. This SHWFS has the same sub-aperture layout as the SHWFSs used by CANARY, an AO demonstrator on the 4.2 m WHT, La Palma.

When a SHWFS is observing spots that have undergone wavefront reconstruction, the system is being operated in closed-loop. If a SHWFS is observing spots that have not undergone wavefront reconstruction, the system is being operated in open-loop.

2.2.4 Wavefront reconstruction

Below we outline the technique for using an interaction matrix to perform wavefront reconstruction. As a stable plane wave is required, measuring the interaction matrix usually involves recreating the system on an optical bench.

To measure the influence of a specific DM actuator, a voltage is applied to it while the rest of the DM is in its rest position. A plane wave is then passed through the system. SHWFS measurements are made with a voltage applied to this actuator, and this process is then repeated for each actuator. This process results in a matrix that relates DM actuator position to SHWFS spot displacement. This matrix is known as the interaction matrix and, in terms of the vector of SHWFS centroids, $\vec{\mathbf{e}}$, it is given by

$$\vec{\mathbf{e}} = \mathbf{K}\vec{\mathbf{u}}. \tag{2.16}$$

In Equation 2.16, $\mathbf{K}$ and $\vec{\mathbf{u}}$ are the interaction matrix and the vector of DM actuator commands, respectively. It is assumed that the movement of each actuator has a linear

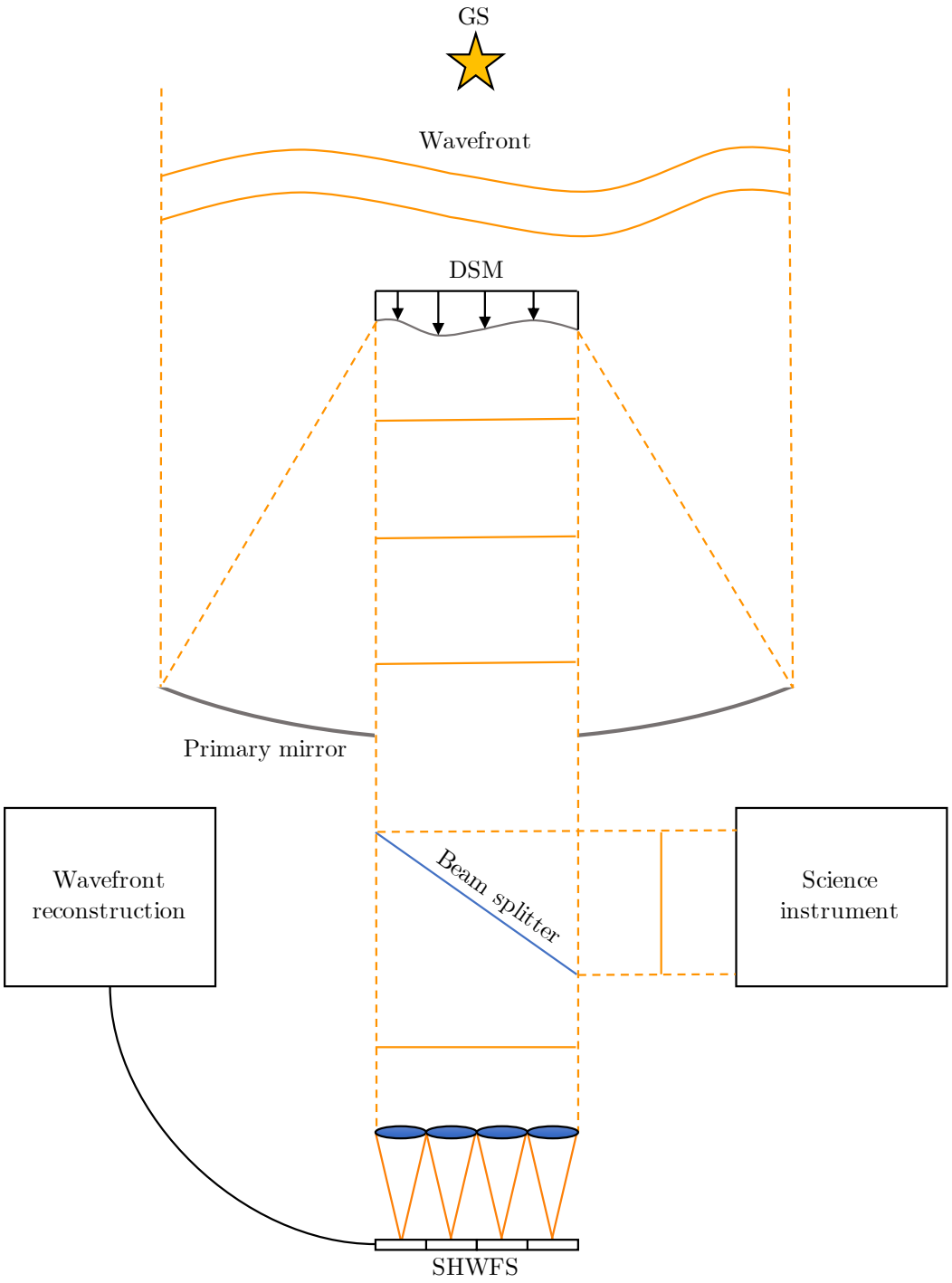

Figure 2.5: Illustration of a DSM restoring a plane wavefront. In this example, the perturbed wavefront is first measured by a SHWFS. A wavefront reconstruction algorithm then closes the loop by passing commands to the DSM. If the science target is (or is nearby) the GS, it can not be picked off and instead a fraction of its light must be redirected to the science instrument with a beam splitter, e.g. a dichroic.

response in the SHWFS, i.e. the response in the SHWFS is linear in both the amplitude and the spatial displacement of the spot.

By inverting the interaction matrix in Equation 2.16, SHWFS measurements can be used to estimate DM commands that will mitigate wavefront perturbations. Similarly, if the DM actuator commands are known while operating a closed-loop system, Equation 2.16 can be used to calculate open-loop centroids. Open-loop centroids that come from this calculation are referred to as pseudo open-loop.

2.2.5 Coherence time

The wind causes atmospheric phase aberrations to evolve in both time and space. This implies that wavefront reconstruction must be a fast process that is continuously updating. For the illustration shown in Figure 2.5 there are a number of steps involved. The system has to measure SHWFS centroids, calculate DM commands and then accurately move DM actuators into their correct position. Each step introduces a time delay and this puts an upper limit on the update rate of the system. This update rate is directly related to the size of the system, e.g. having more SHWFS centroids results in an increased computational workload. However, the required update rate is related to atmospheric conditions. If we express distance, d, as a product of the wind speed moment, $\bar{w_{\mathrm{s}}}$, and the elapsed time, τ, then Equation 2.8 becomes

$$D_\phi(\tau) = \sigma^2_{\mathrm{time}}(\tau) = 6.88\left(\frac{\tau \bar{w_{\mathrm{s}}}}{r_0}\right)^{5/3}. \tag{2.17}$$

The wind speed moment is given by

$$\bar{w_{\mathrm{s}}} = \left[\frac{\int_0^\infty C_n^2(h) w_{\mathrm{s}}(h)^{5/3} dh}{\int_0^\infty C_n^2(h) dh}\right]^{3/5}. \tag{2.18}$$

Equation 2.17 is equal to the mean square phase error, σ^2_{time}, if a wavefront correction is applied after time τ. In Equation 2.18, $w_{\mathrm{s}}(h)$ is the wind speed at altitude h.

A time delay that is commonly acceptable is known as the coherence time, τ_0. It is found when $\sigma^2_{\mathrm{time}}(\tau) = 1\,\mathrm{rad}$, i.e. when the mean square phase error is 1 radian. The coherence time is given by (Greenwood, 1977; Roddier, 1999)

$$\tau_0 = 0.314 r_0 / \bar{w_{\mathrm{s}}}. \tag{2.19}$$

Assuming that wavefronts can be measured exactly, the mean square phase error can be written as

$$\sigma^2_{\mathrm{time}}(\tau) = (\tau/\tau_0)^{5/3}. \tag{2.20}$$

From Equation 2.17, the desired update rate for a closed-loop system is therefore dependent on the shape of both the turbulence and wind speed profile. At the VLT it has been shown that, at $\lambda = 0.5\,\mu\mathrm{m}$, typical values for τ_0 are around 5 ms (Osborn et al., 2018).

Predictive control algorithms can reduce temporal errors by mitigating the latency between the measurement of a wavefront and its successive DM correction. These algorithms use

the Taylor frozen-flow approximation (Taylor, 1938) to predict how atmospheric phase aberrations will evolve. This allows for DM corrections to be scheduled ahead of time. To optimise their performance, these control algorithms commonly require optical turbulence and wind velocity profile information (Jackson et al., 2015; Sivo et al., 2018).

2.2.6 Tomographic adaptive optics

Single-conjugate Adaptive Optics (SCAO) uses one GS to correct over a narrow FOV. This is the mode illustrated in Figure 2.5. To increase the AO corrected FOV, many different configurations have been developed. Discussed in this study are the techniques known as Ground-Layer Adaptive Optics (GLAO), Multi-Object Adaptive Optics (MOAO) and Multi-Conjugate Adaptive Optics (MCAO). All of these techniques involve the use of multiple GSs. We assume that each GS is being observed by an independent SHWFS.

2.2.6.1 Ground-layer adaptive optics

GLAO corrects for ground-layer turbulence (Tokovinin, 2004). The majority of integrated turbulence strength is often found in the ground-layer (Farley et al., 2018) and so GLAO can significantly improve image resolution.

When conjugate to a telescope aperture, multiple SHWFSs will all measure the same ground-layer turbulence. DM commands can therefore be calculated from mean centroid measurements. So that this mean is more statistically representative of the turbulence in the ground-layer, the GSs in GLAO often have large angular separations. Having large angular separations helps reduce common-path aberrations at non-zero altitudes. This can be visualised by studying Figure 2.6. This schematic diagram shows turbulent layers at altitudes h_0 and h_1, where $h_1 > h_0$.

2.2.6.2 Multi-object adaptive optics

MOAO was developed as a technique for correcting within a large FOV. It uses multiple SHWFSs to tomographically reconstruct the turbulence volume above the telescope. After individual science targets are selected, data from the SHWFSs can be used with a DM to perform wavefront correction along each line of sight. As the DMs are correcting for wavefront perturbations in multiple science directions (that are not necessarily in the direction of the GSs), they must be in open-loop with respect to the SHWFSs. An illustration of a 2-GS MOAO system is shown in Figure 2.7.

MOAO uses multiple GSs to increase its FOV. This means it can observe multiple science targets in a single exposure, making it a much more efficient system compared to SCAO. It is, however, a much more complex system. To ensure optimal performance the whole system must be accurately characterised and calibrated. The capability of MOAO has been previously demonstrated on CANARY (Gendron et al., 2011; Vidal et al., 2014; Martin et al., 2017).

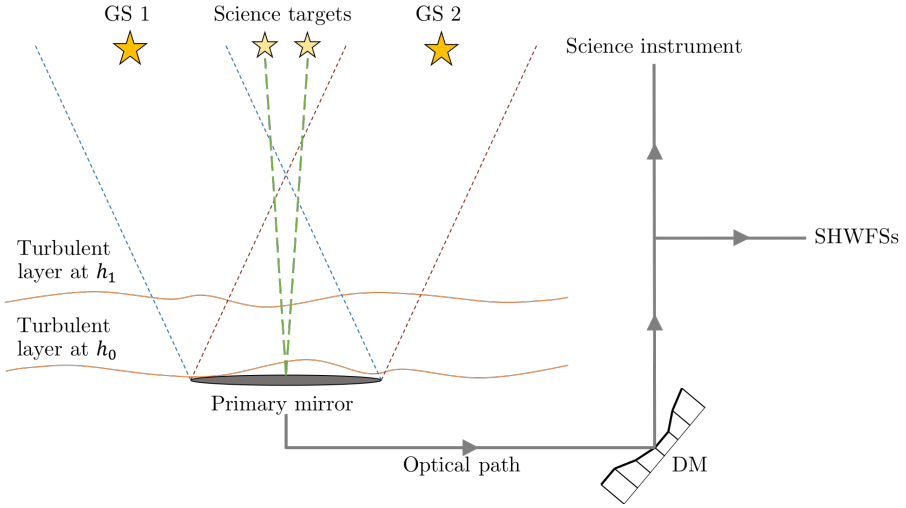

Figure 2.6: Schematic diagram of a 2-GS GLAO system. Independent SHWFSs are being used to study each GS. Ground-layer turbulence is common to all SHWFSs and so DM commands can be calculated from mean centroid measurements.

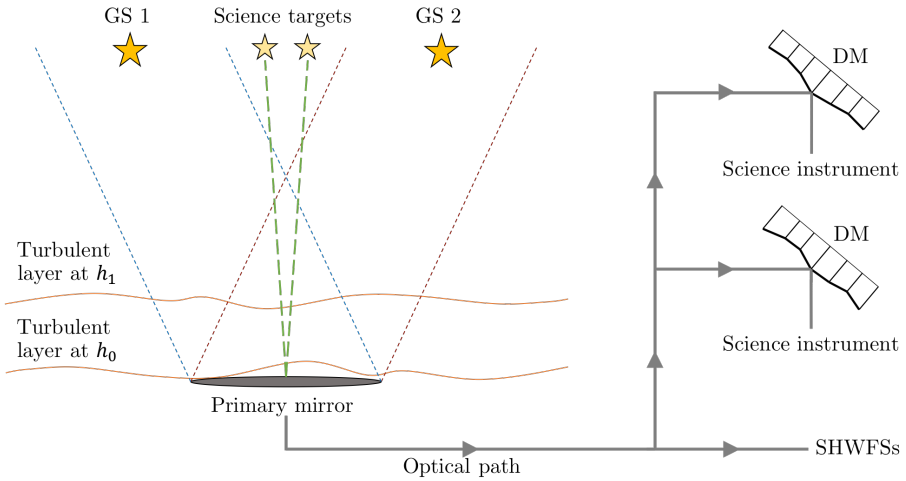

Figure 2.7: Schematic diagram of a 2-GS MOAO system. Independent SHWFSs are being used to study each GS. The SHWFSs are in open-loop with the DMs. This allows the MOAO system to pick off individual science targets within a large FOV.

To tomographically reconstruct the turbulence volume above the telescope, a proposed technique uses SHWFS data to calculate turbulence strength as a function of altitude (Vidal et al., 2010). Precise wavefront reconstruction is reliant on the accuracy of the turbulence profile measurement (Villecroze et al., 2012; Martin et al., 2016b). It has been shown that SHWFS data can also be used to measure optical misalignments (Martin et al., 2016a). Accounting for SHWFS misalignments helps optimise the accuracy of the turbulence profile measurement (Laidlaw et al., 2018).

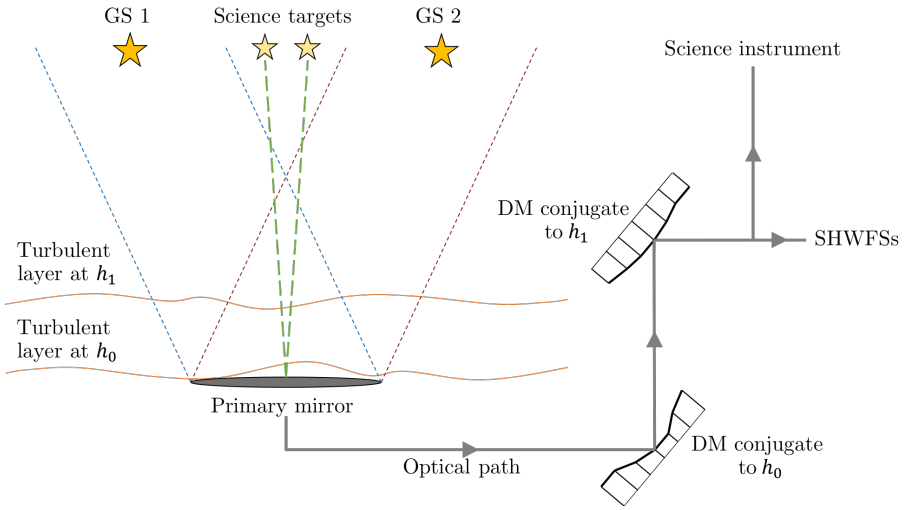

Figure 2.8: Schematic diagram of a 2-GS MCAO system. Independent SHWFSs are being used to study each GS. Each DM is optically conjugate to an exact altitude. This allows the MCAO system to correct for a large continuous FOV.

2.2.6.3 Multi-conjugate adaptive optics

MCAO aims to correct over a large continuous FOV. It does this by splitting the required correction onto multiple DMs. Each DM is optically conjugate to a specific altitude (Beckers, 1988). Figure 2.8 illustrates an MCAO system and it can be seen that by having multiple SHWFSs, a larger section of the turbulent layer at h_1 can be measured and therefore corrected. To correct for the majority of the integrated turbulence strength, one of the DMs is usually conjugate to the ground-layer. However, it is possible to have DMs that can change their position so that they can select the altitudes at which they are optically conjugate. This optimises the system as it allows the DMs to correct for the strongest layers of turbulence (Tallon et al., 1992). Selecting the correct altitudes requires an accurate measurement of the optical turbulence profile. The altitudes of the strongest layers can change (Osborn et al., 2018) and so, to fully optimise the system, the turbulence profile measurement must be updated regularly (Jia et al., 2018).

2.2.7 Simulating atmospheric turbulence

Simulations play a significant role in the development of AO systems. The layout of an AO system is complex and therefore optical alignment is time-consuming. Components such as SHWFSs are also expensive. By testing optical layouts and data analysis techniques in simulation, AO scientists are able to freely alter specific variables so that they can estimate performance. Simulations can also be used to test the sensitivity of a AO system to, for example, optical misalignments. All of the AO simulations within this study are made using the existing software package Soapy* (Reeves, 2016). We discuss the operation of our Soapy simulations below.

*https://github.com/AOtools/soapy

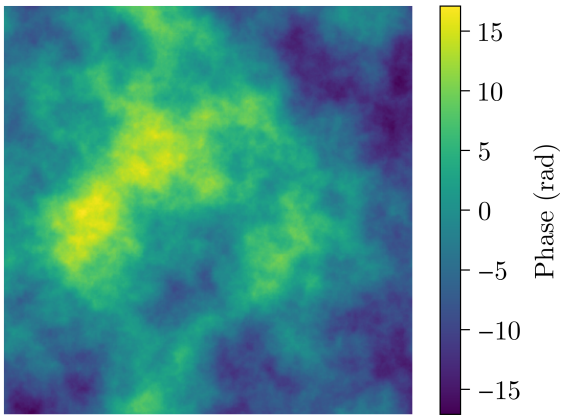

Figure 2.9: Simulated atmospheric phase screen with dimensions equivalent to 39×39 m. L_0 is 25 m and r_0 is equal to 0.1 m at $\lambda = 0.5\,\mu$m.

The atmosphere can be modelled with a number of turbulent layers at discrete altitudes. Each of these layers is generated as a random phase screen that adheres to theoretical von Kármán statistics (Schmidt, 2010). Soapy is therefore described as a Monte Carlo simulation. Simulated GSs then have their phase distorted by having their light propagate through specific sections of the pre-generated phase screens. This light propagation can can be approximated by summing up the phase distortion from each layer (Hardy, 1998). When simulating LGSs, the distance to each LGS must be known so that the cone effect can be correctly modelled. The phase across each SHWFS sub-aperture can then be used to calculate spot displacement.

To model wind, the generated phase screens must move with a specified velocity. This is simulated by each phase screen moving a number of steps in x and y. The number of steps taken corresponds to its wind velocity and the frame rate of the system. It is assumed that the phase screen is frozen as it moves across the pupil. This is known as the Taylor frozen-flow approximation (Taylor, 1938). In our Soapy simulations, wind velocity is simulated using infinite phase screens (Assémat et al., 2006). Infinite phase screens work by taking values from the edges of a pre-existing phase screen, and calculating how these values evolve if they abide von Kármán statistics. By repeatedly calculating new values for the rows and columns in x and y, respectively, phase screen velocity can be simulated while its dimensions remain unchanged.

Figure 2.9 shows a simulated atmospheric phase screen with L_0= 25 m and r_0= 0.1 m at $\lambda = 0.5\,\mu$m. The dimensions of this phase screen are equivalent to 39×39 m.

2.3 Techniques for turbulence and wind velocity profiling

Turbulence and wind velocity profiling have multiple applications within AO. In this section we introduce the atmospheric turbulence and wind velocity profiling techniques

that are addressed during this study.

Used in conjunction with the turbulence profile, the wind velocity profile can enable predictive control algorithms that significantly improve image resolution (see Section 2.2.4). Although it is not fully investigated in this study, it is also believed that by measuring the wind velocity profile, the altitude-resolution of the turbulence profile can be improved (Wang et al., 2008). Having accurate measurements of the turbulence strength as a function of altitude is a requirement for optimising MOAO and MCAO wavefront reconstruction techniques (see Sections 2.2.6.2 and 2.2.6.3).

A further benefit of turbulence and wind velocity profiling is that it assists the queue scheduling of sciences cases, i.e. it allows for σ_{ζ}^2 and σ_{time}^2 to be calculated (see Sections 2.2.1.3 and 2.2.4). If, for example, an AO system is targetting a high-resolution exoplanet image, it is favourable to make this observation while the turbulence strength is relatively weak and slow-moving. So that science cases can be scheduled ahead of time, turbulence and wind velocity profile measurements can be used to help forecast upcoming conditions (Masciadri et al., 2017; see Section 2.3.1). Forecasts may in turn be validated and calibrated by subsequent measurements. It should also be noted that if we know the turbulence and wind velocity profile, AO system performance can be estimated. These estimations can come from the analysis of simulations (see Section 2.2.7).

2.3.1 Forecasts

Previous studies have shown that wind velocity profile measurements are well correlated with forecast models (Osborn et al., 2017; Sivo et al., 2018). In this study we compare against the non-hydrostatic model generated by the European Centre for Medium-Range Weather Forecasts (ECMWF). Wind velocity profiles from 2014 and 2017 are used (Haiden et al., 2014; Haiden et al., 2017).

The ECMWF uses advanced numerical weather prediction techniques and requires meteorological data from multiple sources, e.g. aircraft and weather balloons. The model gives an hourly forecast and is refreshed every six hours. The ECMWF monitors pressure levels and gives the wind velocity profile in discrete layers with the altitude-spacing near the ground being tens of metres. The altitude-spacing increases with altitude and above the tropopause (approximately 17 km) it is hundreds of metres.

2.3.2 Scintillation detection and ranging

SCIntillation Detection And Ranging (SCIDAR; Vernin and Roddier, 1973) is a technique for high-resolution turbulence and wind velocity profiling. It studies scintillation intensity patterns from double star targets and, therefore, it is not possible for the SCIDAR technique and an AO system to run in tandem. The SCIDAR technique is therefore used by instruments that are dedicated profilers, e.g. the Stereo-SCIDAR instrument at the VLT (Osborn et al., 2018). One of the most appealing features of the SCIDAR technique is that

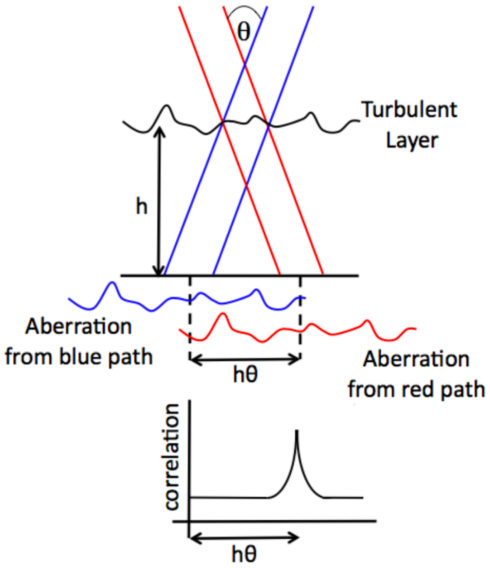

Figure 2.10: Illustration of the how SCIDAR is able to triangulate the turbulence profile. The red and blue wavefronts are from individual stars. By calculating the cross-correlation of the scintillation intensity patterns, the turbulent layer at altitude h is measured. The amplitude of the cross-correlation peak corresponds to the strength of the turbulent layer. This image has been taken from Shepherd et al., 2013.

it can measure high-resolution turbulence and wind velocity profiles. With regard to atmospheric tomography, resolution refers to the altitude-spacing between each measurement. Typical values for SCIDAR altitude-spacing are between 100 and 300 m. In this study we take measurements from the Stereo-SCIDAR instrument (Shepherd et al., 2013) that, in 2014, was on the 2.5 m Isaac Newton Telescope (INT), La Palma (Osborn et al., 2015).

2.3.2.1 Turbulence profiling

The SCIDAR technique performs turbulence profiling by measuring atmospheric scintillation intensity patterns from double star targets. These intensity patterns are imaged onto a CCD. The Stereo-SCIDAR instrument uses this technique however, it images the scintillation patterns from each star onto an independent CCD. The main benefits of using independent CCDs include an increased Signal-to-Noise Ratio (SNR) and having an improved tolerance to the magnitude difference between the two stars (Shepherd et al., 2013). The turbulence profile can be expressed by calculating the cross-correlation between the two intensity patterns. The cross-correlation function is given by

$$\hat{C}_{\mathrm{xy}} = \frac{1}{N-1}\sum_{n=1}^{N}(X_n - \bar{X})(Y_n - \bar{Y}), \tag{2.21}$$

where, for SCIDAR applications, X_n and Y_n are the intensity measurements made by each pixel. An illustration of how SCIDAR triangulates the turbulence profile is shown in Figure 2.10.

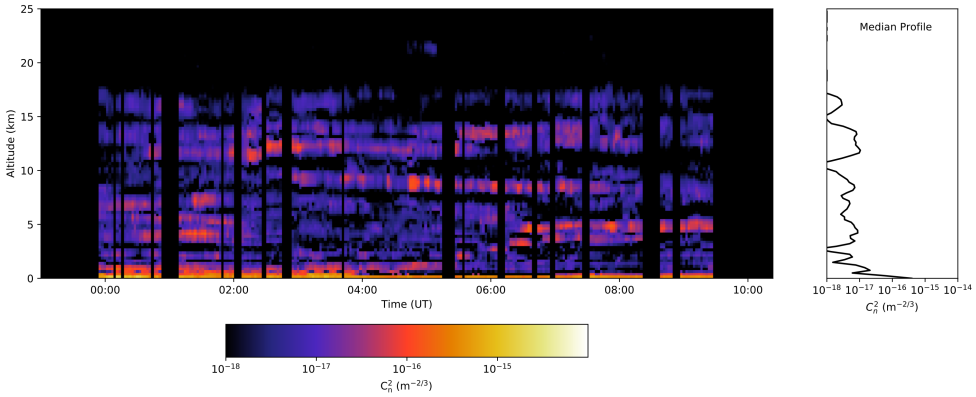

Figure 2.11: The turbulence profiles measured on 08/03/2017 by the Stereo-SCIDAR instrument at the VLT, Paranal. The median turbulence profile is shown on the right. This image has been taken from Osborn et al., 2018.

It is possible to generate theoretical scintillation cross-correlation response functions. Using these theoretical functions, SCIDAR is able to calculate the pseudo-inverse of on-sky cross-correlation measurements. This allows for the turbulence strength to be measured as a function of altitude. An example of how the turbulence profile evolves with time is shown in Figure 2.11. These measurements were made by the Stereo-SCIDAR instrument at the VLT (Osborn et al., 2018).

2.3.2.2 Wind velocity profiling

The SCIDAR technique can also measure the wind velocity profile (Shepherd et al., 2013; Osborn et al., 2017). This requires the measurements of the scintillation intensity patterns described in Section 2.3.2.1. The wind velocity profile can be visualised by using Equation 2.21 to calculate the cross-correlation between scintillation intensity patterns that have a positive temporal offset. This calculation is then repeated but with a negative temporal offset. The three cross-correlation functions previously described (negative, zero and positive) are then added together and averaged as a function of pixel separation. An example of the resultant array is shown in Figure 2.12. In Figure 2.12, the length and orientation of an arrow indicates the velocity of the corresponding layer. Therefore, if turbulent peaks can be tracked from negative to positive temporal offsets, the wind velocity profile can be measured. To reduce the likelihood of false detections, Stereo-SCIDAR typically tracks peaks across a range of temporal offsets, e.g. every frame offset between -2 and $+2$ is calculated (Osborn et al., 2017).

It should also be mentioned that, when measuring the wind velocity profile, the altitude of each layer can be defined by where it crosses the point of zero temporal offset (see Figure 2.12). This technique can update and potentially improve the altitude resolution of the turbulence profile measurement.

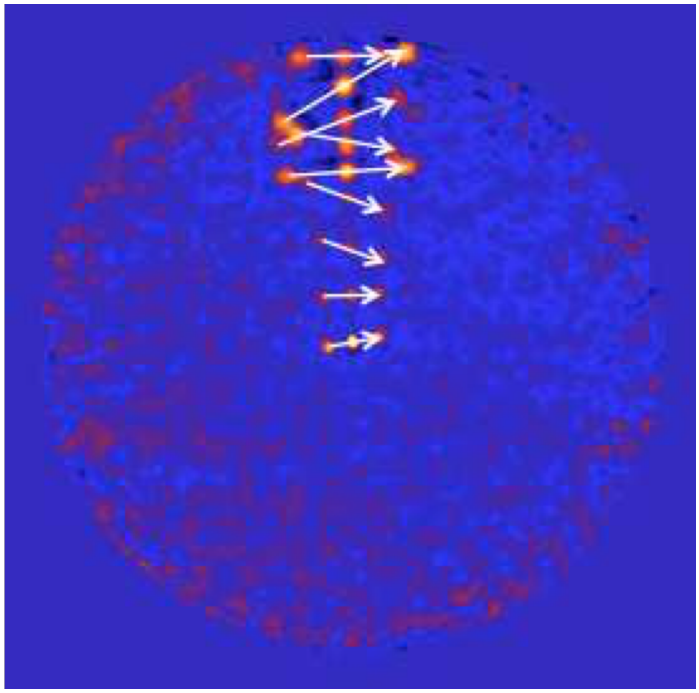

Figure 2.12: An example of a Stereo-SCIDAR cross-correlation function that has been used to calculate the wind velocity profile. The colourscale is the cross-correlation measurement and the axes are a function of pixel separation in x and y. The ground-layer is in the centre of the image and the turbulence profile (at zero temporal offset) is shown along the vertical direction. The turbulence profile altitude increases towards the top of the image. To indicate the wind velocity profile, white arrows have been drawn to show the movement of the turbulent layers. This image has been taken from Shepherd et al., 2013.

2.3.3 Slope detection and ranging

SLOpe Detection And Ranging (SLODAR) is a stereoscopic technique that uses SHWFS data to measure turbulence and wind velocity profiles. It can therefore run in tandem with a number of AO instruments. When used in tandem with an AO system, the required SHWFS data is referred to as AO telemetry.

The SLODAR technique has been detailed in previously published literature (Wilson, 2002; Butterley et al., 2006). It has been demonstrated with dedicated optical turbulence profilers numerous times. For example, since 2009 there has been a dedicated SLODAR instrument at the VLT (Wilson et al., 2009). In 2010, the technique was used to make high-resolution measurements of the VLT surface layer (roughly the first 100 m) (Osborn et al., 2010). There have also been a number of campaigns that have demonstrated the SLODAR technique using on-sky AO telemetry. Using on-sky data from 2011, 2012 and 2013, the SLODAR technique has studied measurements from the 5-LGS MCAO system at the 8 m Gemini South telescope, Cerro Pachón. Results from this campaign have concentrated on frozen-flow, the outer scale, the turbulence profile and the wind velocity profile (Cortés et al., 2012; Guesalaga et al., 2014; Guesalaga et al., 2016). In 2016, turbulence and outer scale profiles were studied using RAVEN, an MOAO demonstrator at the 8.2 m

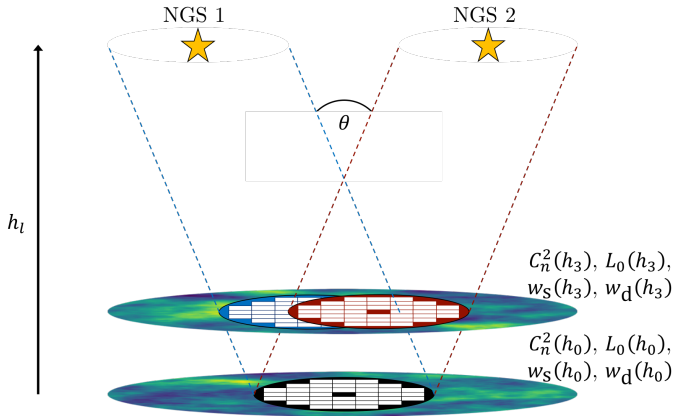

Figure 2.13: Sub-aperture optical paths of two 7×7 SHWFSs to NGS 1 (black to blue) and NGS 2 (black to red). The two turbulent layers are at altitudes of 0 and $3D/7\theta$ km.

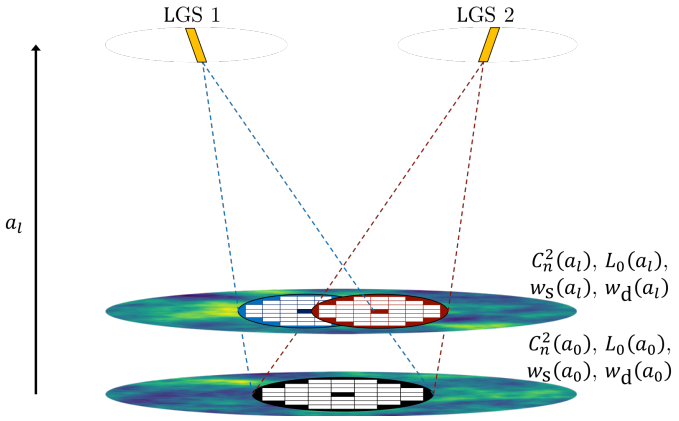

Figure 2.14: Sub-aperture optical paths of two 7×7 SHWFSs to LGS 1 (black to blue) and LGS 2 (black to red). The two turbulent layers are at altitudes of 0 and $3D/7\theta$ km.

Subaru Telescope, Hilo (Ono et al., 2016). The on-sky asterism for RAVEN consisted of 3 NGSs and 1 on-axis LGS. The SLODAR technique has also been applied to NGS and LGS data from CANARY, the MOAO demonstrator at the 4.2 m WHT, La Palma (Martin et al., 2016a). More recently, turbulence and wind velocity profiles from CANARY have been compared against contemporaneous profiles from Stereo-SCIDAR (Laidlaw et al., 2018; Laidlaw et al., 2019).

Like SCIDAR, SLODAR uses a crossed-beam triangulation method for measuring the optical turbulence profile. However, SLODAR triangulates the turbulence profile by studying SHWFS centroids. It requires sufficiently bright objects for wavefront sensing and can use a combination of NGSs and LGSs. The optical phase gradient for each GS is measured at the ground by an independent SHWFS. Figure 2.13 illustrates the sub-aperture optical paths of two optically aligned 7×7 SHWFSs that are observing independent NGSs. In Figure 2.13, the distance to NGS sub-aperture optical path intersection is given by h_l, where

$$h_l = \frac{l s_w}{\theta}. \tag{2.22}$$

Table 2.1: Physical parameters of CANARY, AOF and ELT-scale AO systems.

	CANARY	AOF	ELT-scale
Pupil diameter (m)	4.2	8.2	39.0
Active sub-apertures per SHWFS	36	1240	4260
Sub-aperture baselines per SHWFS	129	4989	17101
SHWFS dimensions (sub-apertures)	7×7	40×40	74×74

In Equation 2.22, θ is the angular separation between the NGSs. The distance between the centres of two adjacent sub-apertures is given by s_{w}. SLODAR is applicable to all position angles in the FOV of the telescope however, it should be noted that Equation 2.22 is only valid for position angles of 0, 90, 180 and 270°. Two altitudes of sub-aperture optical path intersection are shown in Figure 2.13. The sub-aperture separation order is denoted l. In Figure 2.13, the red and blue meta-pupils are separated by 3 sub-apertures and so at this altitude $l = 3$. The maximum distance of sub-aperture optical path intersection, $h_{\max}$ (h_6 for the configuration shown in Figure 2.13), is therefore $(D - s_{\mathrm{w}})/\theta$.

It has been shown that the SLODAR method can utilise LGSs (Cortés et al., 2012). The cone effect (see Section 2.2.1.2) is illustrated in Figure 2.14. Due to the cone effect, the distance to LGS sub-aperture optical path intersection, a_l, does not scale linearly with l. For optically aligned SHWFSs with LGS position angles of 0, 90, 180 or 270°,

$$a_l = \frac{l s_{\mathrm{w}} n_{\mathrm{a}}}{\theta n_{\mathrm{a}} + l s_{\mathrm{w}}}. \tag{2.23}$$

n_{a} is the distance to each LGS. Equation 2.23 assumes that n_{a} is the same for both LGSs.

For SLODAR data analysis, the maximum observable altitude is dependent on the distance to the GSs, the GS angular separation, the diameter of the telescope and the diameter of the SHWFS sub-apertures. In this study we consider the systems used to operate CANARY and the AOF. We also consider the requirements for an Extremely Large Telescope-scale (ELT-scale) system. In particular, we concentrate on the European ELT. This is the European Southern Observatory (ESO) 39 m class telescope that is currently under construction in Cerro Armazones (Tamai et al., 2018). Table 2.1 lists the physical parameters for the CANARY, AOF and ELT-scale AO systems. These parameters can be used to calculate the maximum observable altitude during SLODAR data analysis. If an ELT-scale instrument and CANARY were to observe the same NGS asterism, $h_{\max}$ would be larger for the ELT-scale instrument by a factor of 10.7. The ELT-scale instrument would also have an improved altitude resolution. $h_{l+1} - h_l$ for CANARY and an ELT-scale instrument would be $0.6/\theta$ and $0.53/\theta$, respectively.

2.3.3.1 Covariance matrix

SLODAR uses SHWFSs to record centroids over some time interval. These centroids detail the wavefront perturbations from each GS as atmospheric turbulence is blown across their light-path. Individual sub-aperture optical paths will therefore observe the same patch of turbulence at the altitudes where they intersect (see Figures 2.13 and 2.14). The turbulence

Table 2.2: Values set for the simulated system parameters in the Soapy configuration file.

NGS apparent magnitude	10
Air mass	1
Monochromatic wavelength	$0.5\,\mu$m
Frame rate	150 Hz
Number of frames	10,000
Throughput	30%
Read-out noise	1 electron per pixel

at these altitudes will cause centroids from independent SHWFSs to move similarly. The similarity between centroid values is entirely dependent on the relative strength of the turbulence at each altitude.

The cross-covariance between all SHWFS centroids results in an array referred to as the covariance matrix. This can be calculated using Equation 2.21, where X_n and Y_n are the SHWFS centroid measurements. The amplitude of cross-covariance peaks correspond to the strength of each turbulent layer. To estimate the correct turbulence strength the SHWFS centroids must be recorded in open-loop or pseudo open-loop. From simulated open-loop centroids, a 2-NGS CANARY covariance matrix is shown in Figure 2.15a. Table 2.2 lists the values used in the Soapy configuration file. The optical turbulence profile in Figure 2.15a corresponds to Figure 2.13, i.e. two layers have been simulated at altitudes of 0 and $3D/7\theta\,$km (3/7 comes from there being 7 sub-apertures across each SHWFS, with their meta-pupils separated by 3 sub-apertures at h_3). Both turbulent layers have $L_0 = 25\,$m and $r_0 = 0.1\,$m. Orthogonal measurements from NGS 1 and NGS 2 are given by x_1, y_1 and x_2, y_2, respectively. Tip-tilt aberrations are decorrelated and so orthogonal cross-covariance measurements have a relatively low SNR. The cross-covariance between sub-apertures from the same SHWFS, i.e. the autocovariance, give a measure of the integrated turbulence strength. The strongest response to the vertical structure of the optical turbulence profile is between equivalent planes of independent SHWFSs, e.g. $\mathrm{cov}(x_1, x_2)$ and $\mathrm{cov}(y_1, y_2)$.

2.3.3.2 Covariance map

We define baseline as the sub-aperture separation between two optically aligned SHWFSs. The baseline in x and y is given by x_{sep} and y_{sep}, respectively. The cross-covariance between equivalent planes of independent SHWFSs, e.g. x_1x_2 and y_1y_2 in Figure 2.15a, can be averaged as a function of x_{sep} and y_{sep}. The resultant array is known as a covariance map. The covariance map from Figure 2.15a is shown in Figure 2.15b. The covariance map contains all the high SNR information for the vertical structure of the optical turbulence profile. If there are random errors in the centroid values, e.g. due to shot noise, then averaging baselines increases the SNR of the optical turbulence profile.

Any two GSs in the FOV of the telescope are separated by a position angle, γ. In Figure 2.13, $\gamma = 0\,$rad and as shown in Figure 2.15b, the optical turbulence profile is primarily projected over sub-aperture separations that are determined by γ.

2.3.3.3 Covariance map region of interest

Measurements within the covariance map can be extracted along the vector projected by γ – a covariance map Region of Interest (ROI). This requires γ to be known with respect to the geometry of the SHWFS lenslet array. The covariance map ROI in Figure 2.15c is taken from the centre of x_1x_2 and y_1y_2 in Figure 2.15b, and along positive y_{sep}. In reality, the GS position angle can have any value and so the optical turbulence profile is not always projected across exact baselines (as it is in Figure 2.15). The ROI can compensate for this by encapsulating a larger extent of the map, i.e. its length and width can be increased. The length and width of the ROI are denoted by L and W, respectively. Both L and W are in units of the distance between two adjacent sub-apertures, s_{w}. Figure 2.15c has $L = n_{\text{d}} = 7$ and $W = 1$, where n_{d} is the number of SHWFS sub-apertures in one dimension. If L is greater than n_{d}, this implies that, for the configuration in Figure 2.15c, the ROI includes negative y_{sep} data points. For example, $L = (n_{\text{d}} + 1)$ is the same ROI in Figure 2.15c but with the inclusion of $x_{\text{sep}}, y_{\text{sep}} = (0, -1)$ in both x_1x_2 and y_1y_2 from Figure 2.15b. $L > n_{\text{d}}$ can be thought of as extending the ROI to data points that are projected along $\gamma + \pi$.

There are current as well as forthcoming AO systems that utilise more than two GSs. This introduces the capability of analysing the optical turbulence profile at multiple altitude resolutions. The covariance map ROI studies the optical turbulence profile in a multi-GS system by stacking the ROI from each GS combination into a single array.

2.3.3.4 Turbulence profiling

The phase structure function from Equation 2.12 can be related to the phase covariance function, $C_\phi(d)$, by

$$D_\phi(d) = 2\big(\sigma_\phi^2 - C_\phi(d)\big). \tag{2.24}$$

The phase variance is given by σ_ϕ^2. Using Equation 2.12, the analytical expression for phase covariance is therefore (Beghi et al., 2008)

$$C_\phi(d) = \left(\frac{L_0}{r_0}\right)^{5/3} \times \frac{\Gamma(11/6)}{2^{5/6}\pi^{8/3}} \left[\frac{24}{5}\Gamma\left(\frac{6}{5}\right)\right]^{5/6} \times \left(\frac{2\pi d}{L_0}\right)^{5/6} K_{5/6}\left(\frac{2\pi d}{L_0}\right). \tag{2.25}$$

$C_\phi(d)$ is the spatial covariance of phase between two points at a distance d. The covariance for each turbulent layer depends on r_0, L_0, h, sub-aperture separation and optical misregistrations. Equation 2.25 can therefore be used to calculate an analytical expression for the covariance between sub-apertures.

In Equation 2.25, d is the separation distance between two sub-apertures. At non-zero altitudes covariance values can be generated by calculating the distance between meta-pupil sub-apertures (see Figures 2.13 and 2.14). Therefore, by writing an algorithm that can calculate sub-aperture separation distances between all meta-pupils, it is possible to analytically generate SHWFS spatial covariance for any turbulence profile. This implies that the arrays shown in Figure 2.15 can be analytically generated. By adjusting d, we can also calculate the spatial covariance between misaligned SHWFSs.

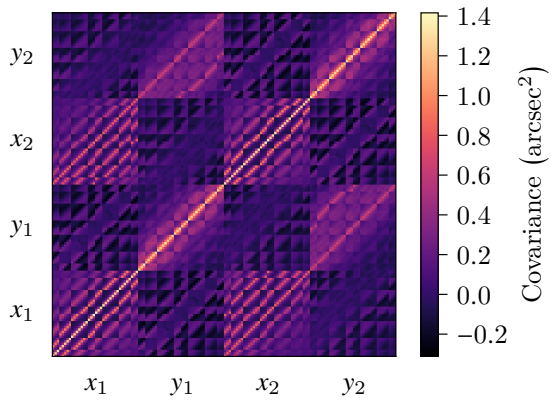

(a) Covariance matrix from two 7×7 SHWFSs observing turbulent layers at altitudes of 0 and $3D/7\theta$ km. Both layers have $r_0 = 0.1$ m and $L_0 = 25$ m.

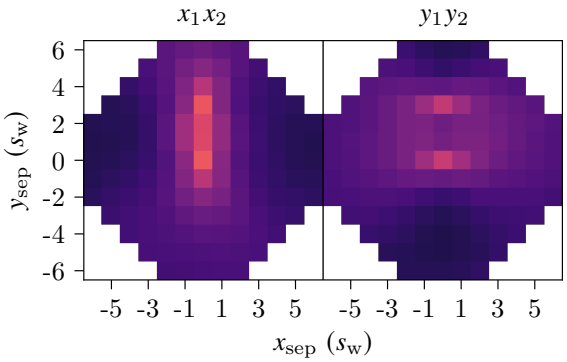

(b) The covariance map from (a). This shows the average covariance between x_1x_2 and y_1y_2 as a function of baseline.

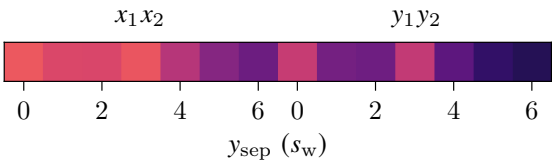

(c) The covariance map ROI from the data points in (b). In this example, the length and width of the ROI are given by $L = n_{\text{d}} = 7$ and $W = 1$, respectively.

Figure 2.15: Techniques for expressing the optical turbulence profile from the cross-covariance of SHWFS centroids. The centroids were simulated using CANARY-scale SHWFSs.

Being able to analytically generate sub-aperture covariance makes it possible to iteratively fit a model to SHWFS cross-covariance measurements. This is the idea of the learn stage within learn and apply MOAO tomography (Vidal et al., 2010). Previous studies have shown that the turbulence profile can be measured using covariance matrix fitting (Vidal et al., 2010; Martin et al., 2016a; Laidlaw et al., 2018). Covariance matrix fitting can also be used for measuring SHWFS misalignments (Martin et al., 2016a; Laidlaw et al., 2018). Other studies have shown that a covariance map ROI can be used to perform optical turbulence profiling (Butterley et al., 2006; Cortés et al., 2012; Guesalaga et al., 2014; Ono et al., 2016; Guesalaga et al., 2016; Laidlaw et al., 2018). The optimal SLODAR technique for turbulence profiling - in terms of accuracy and efficiency - is the subject of Chapter 3.

2.3.3.5 Wind velocity profiling

The SLODAR technique can express the wind velocity profile in a similar way to the SCIDAR method (discussed in Section 2.3.2.2). We refer to the covariance map array (as outlined in Section 2.3.3.2) as M_0. Calculating the cross-covariance between temporally offset SHWFS centroid measurements causes each turbulent layer to be independently shifted away from its M_0 origin. This can be visualised by studying h_3 in Figure 2.13. If Taylor frozen-flow is assumed and the SHWFS observing NGS 2 has its centroids temporally offset, this corresponds to the phase observed by the red meta-pupil being shifted with the movement of the turbulent layer. In covariance-space this corresponds to the turbulent layer being linearly displaced from its M_0 origin. Each turbulent layer has its own displacement vector. The angle of the displacement vector is the direction in which the turbulent layer is passing across the light-path of the telescope. For the example above, the angle of the h_3 displacement vector is $w_\mathrm{d}(h_3)$. The magnitude of its change in baseline location is $\omega w_\mathrm{s}(h_3)/f$, where f is the frame rate, ω is the number of frames that have been offset and $w_\mathrm{s}(h_3)$ is the wind speed.

A covariance map with a negative temporal offset can be stacked alongside its positive reciprocal. Having both positive and negative temporal offsets allows for the wind direction of each layer to be studied. If displacement vectors are large enough, turbulent layers can be displaced so that they no longer appear within a temporally offset covariance map. The inclusion of both positive and negative offsets helps reduce the likelihood of losing turbulent layer peaks. For example, imagine a layer near the edge of the covariance map (close to h_max) in Figure 2.15b. If this layer has a wind direction of 0° then, for a relatively small displacement vector, its peak will not appear in a covariance map that has a positive temporal offset. However, its peak will appear in a covariance map that has an equal but negative temporal offset.

Figure 2.16 shows CANARY covariance maps that have been calculated from temporally offset centroids. A single layer has been simulated at the ground with r_0= 0.1 m and L_0= 25 m. The centroids were simulated using Soapy and the system was parameterised by the values listed in Table 2.2. The covariance map with a negative temporal offset is highlighted by having its values multiplied by -1. In an optically aligned system the

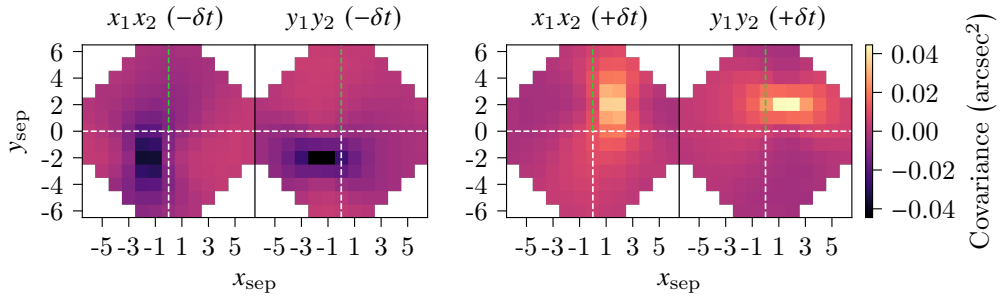

Figure 2.16: Temporally offset covariance maps from simulated SHWFS centroids. A turbulent layer has been simulated at 0 km with a wind direction of 37°. The layer is characterised by $r_0 = 0.1$ m and $L_0 = 25$ m. Broken lines have been overlaid to indicate $x_{\text{sep}}, y_{\text{sep}} = (0, 0)$ (white) and the GS position angle, γ (green).

ground-layer is centred in M_0 at $x_{\text{sep}}, y_{\text{sep}} = (0, 0)$, i.e. where the broken lines are centred in Figure 2.16. It can be seen in Figure 2.16 that after introducing a temporal offset the ground-layer has been shifted away from this location. The ground-layer was simulated to have a wind direction of 37°. The measured temporally offset covariance map array is referred to as $M_{\delta t}$, where δt denotes the temporal offset ω/f. Therefore, as with SCIDAR (see Section 2.3.2.2), if turbulent layer peaks can be tracked from negative to positive temporal offsets, the wind velocity profile can be measured (Wang et al., 2008; Sivo et al., 2018; Laidlaw et al., 2019).

2.3.3.6 Outer scale profiling

The SLODAR technique is able to use SHWFS GS measurements to triangulate atmospheric turbulence strength as a function of altitude (see Section 2.3.3). These atmospheric aberrations have an outer scale, L_0. As mentioned in Section 2.1.3, investigations indicate that the outer scale in the free atmosphere is on the order of 10 to 100 m (Ziad et al., 2004; Maire et al., 2007; Martin et al., 2016a; Ono et al., 2016). However, using the SLODAR technique, the existing class of telescopes do not have the spatial scale to construct an un-biased L_0 profile (Ono et al., 2016). It has been shown that there is no significant difference in SLODAR data analysis when the outer scale is over roughly three times the diameter of the telescope pupil (Guesalaga et al., 2016). For these reasons it is common practice for the existing class of telescopes to assume that, at non-zero altitudes, $L_0 = 25$ m (Ono et al., 2016; Laidlaw et al., 2018).

In Figure 2.17 we show how the outer scale influences the shape of the theoretical cross-covariance function. The cross-covariance values are plotted as a function of separation in both positive and negative directions, i.e. the values for a corresponding covariance map ROI with $L = 2 \times n_{\text{d}} - 1$ (see Section 2.3.3.3). CANARY, AOF and ELT-scale AO systems (see Table 2.1) are shown for L_0 values of 10, 25, 40, 55 and 70 m. Figure 2.17a and Figure 2.17b show that for its expected values at non-zero altitudes, L_0 does not play a critical role when applying SLODAR data analysis to the current class of telescopes. The

shape of the functions also imply that it is a very difficult parameter to measure, especially if the turbulence does not abide von Kármán statistics. This can happen if the turbulence is not fully developed (Lehtonen et al., 2018) or if the cross-covariance measurements have insufficient numerical sampling (Martin, 2014). Throughout this study we will assume that at non-zero altitudes, $L_0 = 25\,\mathrm{m}$. ELT-scale telescopes might not be able to make this approximation (see Figure 2.17c). Either through ELT SLODAR data analysis or a dedicated outer scale profiler, it is possible that they will be required to measure $L_0(h)$.

2.4 Current and future telescopes

In this section we review the telescopes and AO systems that are considered during this study. The physical parameters for these AO systems are listed in Table 2.1. However, it should be noted that the open-source algorithms we have developed (described in Chapters 3 and 4) can be configured to any tomographic AO system.

2.4.1 William Herschel telescope

Since 2010, the 4.2 m WHT has hosted CANARY, an MOAO (see Section 2.2.6.2) demonstrator for ELT-scale technologies. Using the learn and apply algorithm (see Section 2.3.3.4; Vidal et al., 2010), CANARY has successfully demonstrated NGS MOAO (Gendron et al., 2011). Its SHWFS data has also been used to study the turbulence, wind and outer scale profile (Martin et al., 2016a). More recently, turbulence and wind velocity profiles from CANARY have been directly compared to SCIDAR measurements (Laidlaw et al., 2018; Laidlaw et al., 2019).

Throughout this study the CANARY system operates four open-loop 7×7 SHWFSs. The sub-aperture layout for each of these SHWFSs is shown in Figure 2.4.

Recent studies from CANARY have concentrated on the effects of sodium LGS elongation (see Section 2.2.1.2; Bardou et al., 2018; Basden et al., 2018). The launch telescope is 40 m away from the WHT so that ELT elongation can be replicated. A photograph of the WHT with its sodium LGS is shown in Figure 2.18.

2.4.2 Very large telescope

The AOF is hosted by the 8.2 m Yepun telescope at the VLT, Paranal. As part of the AOF, two AO systems have been installed: GRound-layer Adaptive optics Assisted by Lasers (GRAAL; Paufique et al., 2010) and Ground Atmospheric Layer Adaptive Corrector for Spectroscopic Imaging (GALACSI; Stuik et al., 2006). Both of these AO systems have four 40×40 SHWFSs. The AOF also has four side-launched sodium LGSs (see Section 2.2.1.2). To perform AO correction, the AOF has a DSM with 1170 actuators (see Section 2.2.3).

In Section 5.2, we study data from GALACSI. These observations were made during its commissioning phase in mid-June 2017. The GALACSI data was recorded while it was

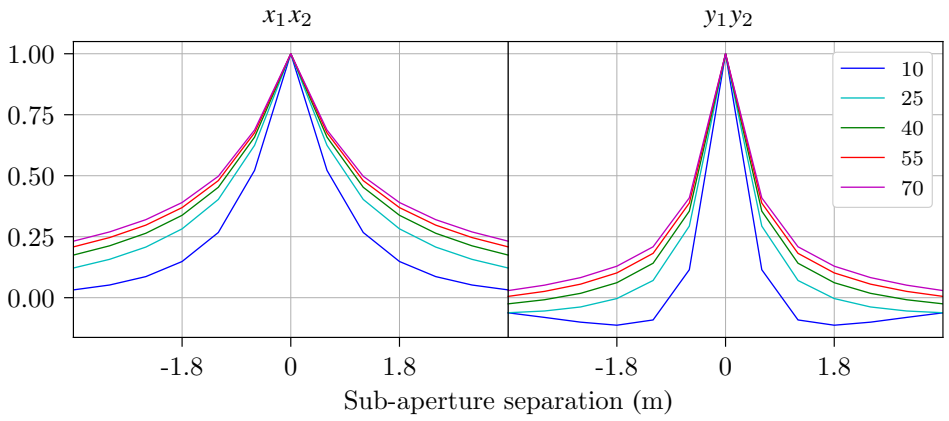

(a) Theoretical sub-aperture cross-covariance for CANARY. The analytically generated layer is at 0 km and is shown for L_0 values of 10, 25, 40, 55 and 70 m.

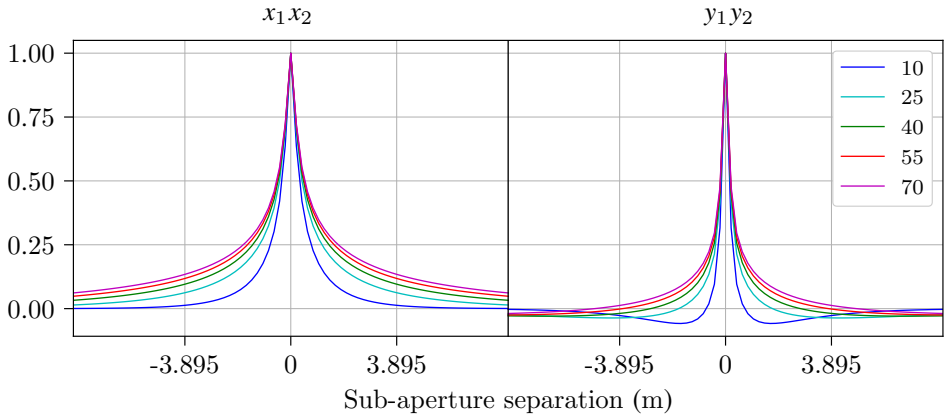

(b) Theoretical sub-aperture cross-covariance for the AOF. The analytically generated layer is at 0 km and is shown for L_0 values of 10, 25, 40, 55 and 70 m.

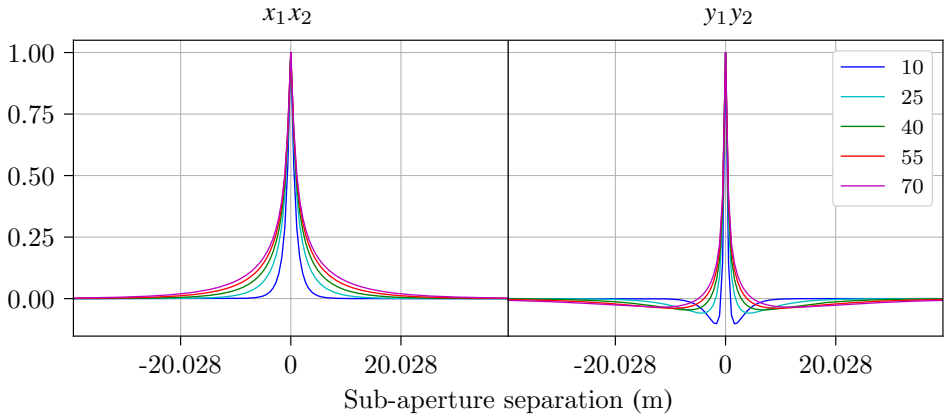

(c) Theoretical sub-aperture cross-covariance for an ELT-scale system. The analytically generated layer is at 0 km and is shown for L_0 values of 10, 25, 40, 55 and 70 m.

Figure 2.17: Normalised theoretical cross-covariance for CANARY, AOF and ELT-scale systems, over a range of L_0 values.

Figure 2.18: Photograph of the sodium LGS used by CANARY on the 4.2 m WHT, La Palma (Bardou, 2018).

Figure 2.19: Photograph of the four sodium LGSs used by the AOF on the 8.2 m Yepun telescope at the VLT, Paranal (Horálek, 2018).

being operated as a GLAO module (see Section 2.2.6.1) for the Multi-Unit Spectroscopic Explorer (MUSE; McDermid et al., 2008). Its SHWFSs were monitoring each LGS in closed-loop. Figures 2.1 and 2.19 show photographs of the 4-LGS system of the AOF.

2.4.3 Extremely large telescope

In this study we concentrate on the European ELT. This is the 39 m class telescope currently being constructed by ESO in Cerro Armazones (Tamai et al., 2018). It is scheduled to begin operations before 2030. There are three first-light instruments planned for the European ELT: High Angular Resolution Monolithic Optical and Near-infrared Integral field spectrograph (HARMONI), the Mid-infrared ELT Imager and Spectrograph (METIS) and the Multi-AO Imaging CAmera for Deep Observations (MICADO).

We perform our ELT investigation using parameters originally planned for the HARMONI

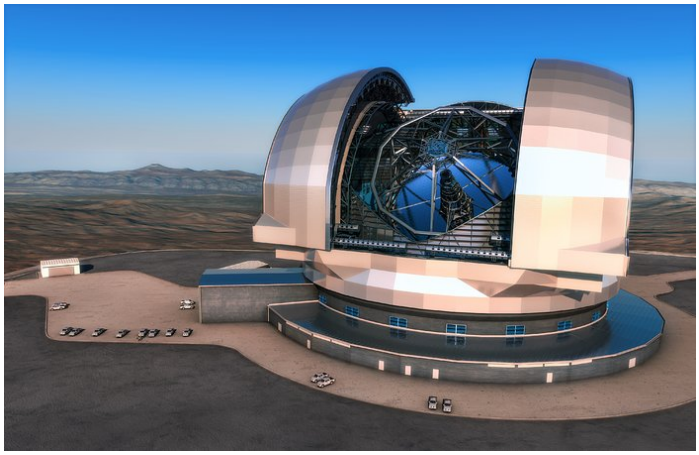

Figure 2.20: A conceptual drawing of the 39 m European ELT (Calçada, 2014). Current plans state that it will see first-light before 2030.

AO system. This system uses 74×74 SHWFSs. However, these dimensions are subject to change and so we refer to this system as ELT-scale. A conceptual drawing of the European ELT is shown in Figure 2.20. Current designs state that it will have six LGSs.

— 3 —

Turbulence profiling from adaptive optics telemetry

The optical turbulence profile can be recovered by iteratively fitting an analytical model to the measured covariance matrix (Vidal et al., 2010). Covariance matrix fitting can also be used for Adaptive Optics (AO) parameter estimation, e.g. measuring Shack–Hartmann Wavefront Sensor (SHWFS) misalignments (Martin et al., 2016a). The optical turbulence profile can be used to optimise Multi-Object Adaptive Optics (MOAO; see Section 2.2.6.2) and Multi-Conjugate Adaptive Optics (MCAO; see Section 2.2.6.3) correction techniques. Therefore, to assure science goals are met, forthcoming Extremely Large Telescope (ELT) AO systems must be updated regularly with an accurate measurement of the optical turbulence profile (Jia et al., 2018). However, the covariance matrix from an ELT-scale AO system will contain millions of cross-covariance measurements. This makes it a challenge to perform efficient ELT covariance matrix fitting. Further benefits of optical turbulence profiling include queue scheduling of science cases and performance monitoring.

Previous studies have shown that a covariance map Region of Interest (ROI) can be used to perform SLOpe Detection And Ranging (SLODAR) data analysis (see Section 2.3.3.3). In this chapter we introduce our methodology and study how many baselines must be included within a covariance map ROI to optimise turbulence profiling accuracy. This leads us to further explore the benefits of using a covariance map ROI for SLODAR data analysis. The covariance map ROI is compared to its covariance matrix counterpart throughout. Three different scales of AO systems are considered: CANARY, a MOAO pathfinder on the 4.2 m William Herschel Telescope (WHT; see Section 2.4.1), La Palma; the Adaptive Optics Facility (AOF) on the 8.2 m Yepun telescope at the Very Large Telescope (VLT; see Section 2.4.2), Paranal; and an instrument designed for the 39 m European ELT (see Section 2.4.3), Cerro Armazones. The physical parameters for each AO system are listed in Table 2.1.

In Section 3.4 we assess the sensitivity of the two SLODAR methods, i.e. covariance matrix and map ROI fitting, with respect to SHWFS misalignments in rotation and lateral shift. It has been shown that the covariance matrix can be used to measure SHWFS misalignments (Martin et al., 2016a). If these misalignments can be measured they can be compensated for during the optical turbulence profiling procedure. We build upon this work and show in Section 3.5 that, with a modified fitting procedure, the covariance map ROI can also measure and compensate for SHWFS misalignments.

In Section 3.6 we compare the turbulence profiling accuracy of the two SLODAR methods. This comparison is made using simulated Natural Guide Star (NGS) and Laser Guide Star (LGS) data from CANARY. In addition, we investigate the optimal size of the covariance map ROI. Quantitative analysis is presented in Section 3.7.1 for the reduction in computational time when performing SLODAR data analysis with a covariance map ROI instead of a covariance matrix. The potential benefits for an ELT-scale instrument are considered in Section 3.7.2.

3.1 Covariance mapping matrix

Covariance maps are often calculated by averaging common baselines in the covariance matrix (see Section 2.3.3.2). This usually involves using an algorithm that loops through covariance matrix regions, making it a slow process. Traditionally, this algorithm calculates the separation distance of each sub-aperture with respect to all other sub-apertures, and then places each covariance measurement into its correct location within the covariance map. The mean at each separation distance is then calculated. Here a tool known as the Covariance Mapping Matrix (CMM) is introduced. This tool eradicates the need to loop over covariance matrix regions. It also offers an efficient technique for passing from centroid-space to a covariance map ROI. It should be noted that the CMM is applicable to all pupil masks and can account for inactive sub-apertures in any location.

In Figure 2.15, the covariance matrix was calculated using 2 SHWFSs that each had 49 sub-apertures (see Figure 2.4). However, the circular pupil and central obstruction had reduced the number of active sub-apertures to 36. The cross-covariance between centroids along specific axes form a Mapping Region (MR) within a covariance matrix, e.g. for Figure 2.15b, the MRs in Figure 2.15a are x_1x_2 and y_1y_2. To simplify notation, the sub-aperture axes that make up a MR will be referred to as s_a and s_b. A CANARY-scale MR is shown in Figure 3.1a. The sub-aperture separation distance in x and y is given by x_sep and y_sep, respectively. The first step in the creation of the CMM is to include inactive sub-apertures. The adaptation of this is shown in Figure 3.1b. From here, it is possible to shift the array so that x_sep is aligned at every y_sep. An example of a CANARY-scale CMM is shown in Figure 3.1c.

3.1.1 Simplified baseline averaging

If the geometry of the SHWFSs is known, the CMM can be pre-computed. This makes it trivial to transform a MR into a covariance map. The CMM is simply filled with data points from the MR, which are subsequently summed along s_b. The resulting one-dimensional array can then be re-shaped into a covariance map. To find the average cross-covariance values the final step is to divide by the number density at each sub-aperture separation (an array that can also be pre-computed). In Figure 3.2 we demonstrate how the CMM calculates the covariance map from a MR.

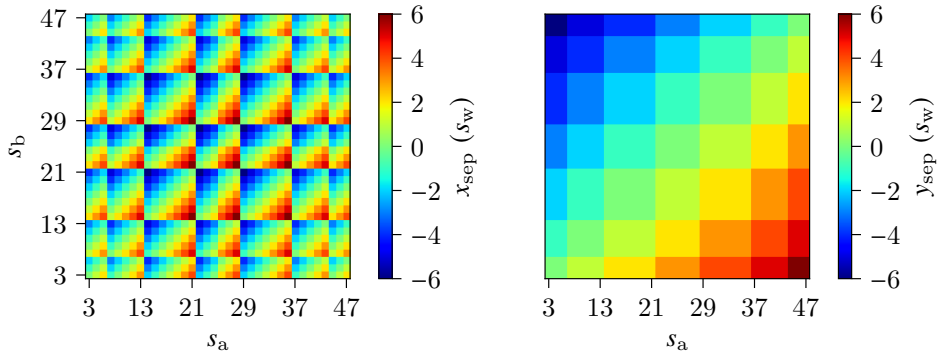

(a) MR for active sub-apertures expressed in terms of x_{sep} (left) and y_{sep} (right).

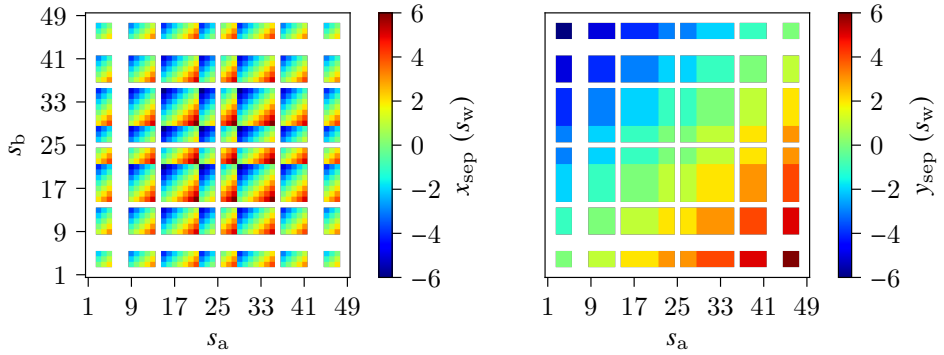

(b) MR with inactive sub-apertures accounted for. Whitespace indicates an inactive sub-aperture.

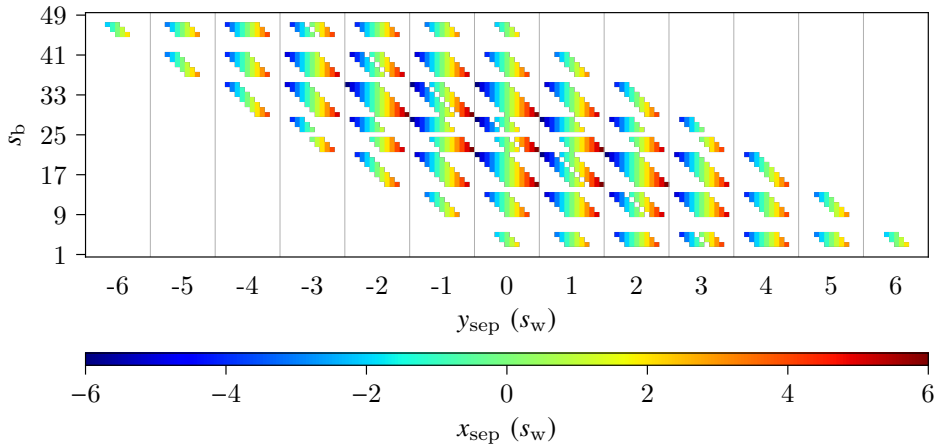

(c) CMM expressed in terms of x_{sep}

Figure 3.1: The process by which an algorithm can calculate the CMM for any pupil mask. The outlined process is for a CANARY-scale pupil mask (see Sections 2.2.2 and 2.3.3.1)

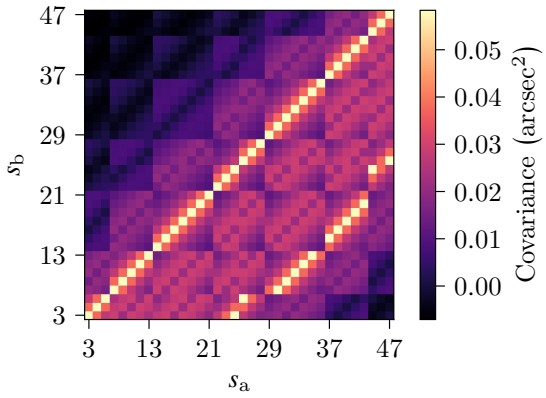

(a) An example MR. Here we show the y_1y_2 MR from Figure 2.15a.

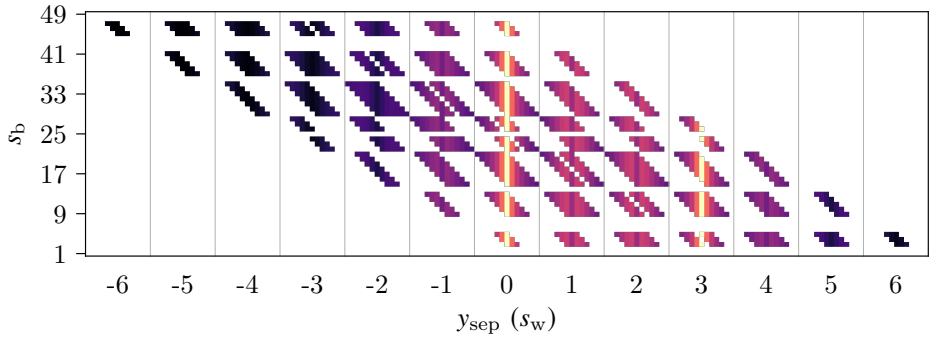

(b) The CMM filled with the data points shown in (a). We can calculate the the required CMM by using the steps that are outlined in Section 3.1.

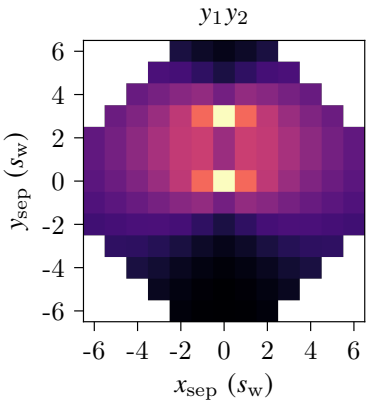

(c) The covariance map calculated from the CMM shown in (b). The covariance map is calculated from (b) by finding the mean along the vertical axis and then reshaping the array.

Figure 3.2: The process used by the CMM to calculate the covariance map from a MR.

To transform a MR to a covariance map ROI, the Guide Star (GS) position angle, γ, must be calculated along with its vector coordinates in x_{sep} and y_{sep}. Once the CMM is filled with the MR, x_{sep} and y_{sep} coordinates can be used to reference the data points that are required to calculate the covariance map ROI. At this point, the same process as above follows but with only the specified baselines considered.

3.1.2 Directly calculate baseline cross-covariance

The CMM can also be viewed in terms of sub-aperture numbering for the SHWFS axes that make up its respective MR. To illustrate, the CMM from Figure 3.1c is shown for s_{a} and s_{b} numbering in Figure 3.3. As in Section 3.1.1, knowing the required baselines allows for the CMM to be used as a reference table. These positions can be transferred to Figure 3.3 that then tell the system which s_{a} and s_{b} combinations to calculate the cross-covariance between.

To demonstrate, consider the ground-layer. If the SHWFSs are optically aligned then the peak of this layer is found by calculating the average cross-covariance between all sub-apertures at $x_{\text{sep}} = y_{\text{sep}} = 0$. First, the CMM in Figure 3.1c is used which indicates that these baselines lie directly along its central column. Figure 3.3 is then referred to which shows that these baselines correspond to the cross-covariance between equivalent sub-aperture numbers in s_{a} and s_{b}. The average cross-covariance between these sub-apertures is then calculated to solve for the covariance map ROI value at $x_{\text{sep}} = y_{\text{sep}} = 0$. This process can be repeated for all sup-aperture separations within the covariance map ROI.

Using the CMM significantly reduces the number of required calculations. For the configuration in Figure 2.15, the difference in the number of calculations between a MR and the covariance map ROI is greater than an order of magnitude. When the covariance map ROI is compared to the entire covariance matrix, this difference is almost two orders of magnitude.

3.2 Subtracting ground-layer isoplanatic turbulence

It has been documented that turbulence statistics for the ground-layer deviate from the Kolmogorov model (Guesalaga et al., 2014; Lehtonen et al., 2018). This is largely attributed to turbulence within the dome being slow-moving and not fully developed. If the ground-layer has non-Kolmogorov statistics then its cross-covariance function will differ from the analytical model. This prevents accurate measurements of turbulent layers at non-zero altitudes. However, it is possible to mitigate the ground-layer by subtracting ground-layer isoplanatic turbulence. To perform this subtraction, the mean centroid in x and y is calculated at each frame for each sub-aperture location. All centroids from every SHWFS then have their respective mean centroid subtracted, i.e. each sub-aperture baseline has common-motion removed. Subtracting ground-layer isoplanatic turbulence simultaneously

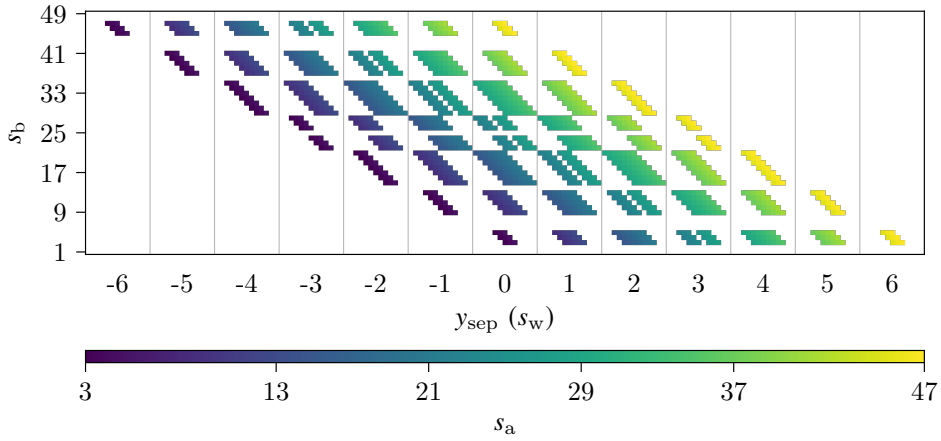

(a) CMM expressed in terms of s_a.

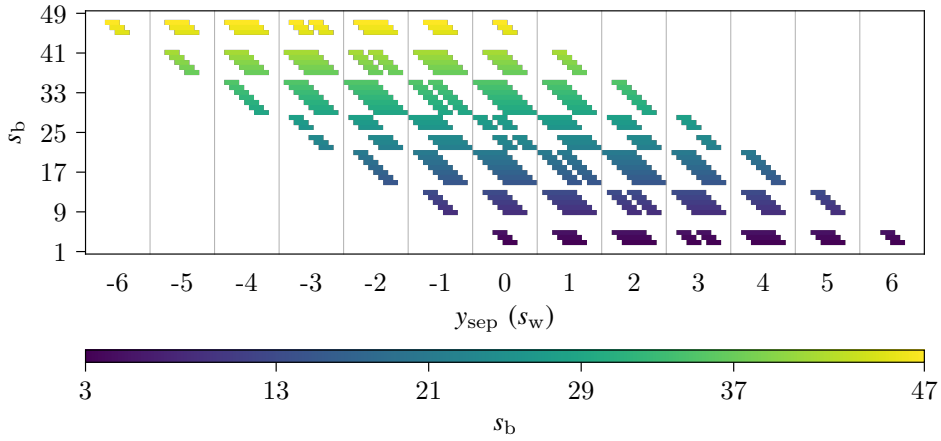

(b) CMM expressed in terms of s_b.

Figure 3.3: CMMs expressed in terms of sub-aperture numbering. In conjunction with Figure 3.1c, this numbering system can be used by a CANARY-scale pupil mask to directly calculate SHWFS cross-covariance values at specific baselines.

removes vibration artefacts. These vibration artefacts are remnants of wind-shake and telescope tracking errors, and are seen as a linear addition to cross-covariance measurements with independent values at xx and yy.

Removing ground-layer isoplanatic turbulence is a linear subtraction. Therefore, the transformation matrix, $\mathbf{T}$, used to perform this subtraction can be directly applied to an analytically generated covariance matrix. Having $\mathbf{A}$ and $\mathbf{B}$ represent an analytically generated covariance matrix before and after ground-layer mitigation, respectively, implies that

$$\mathbf{B} = \mathbf{T} \cdot \mathbf{A} \cdot \mathbf{T}^{\mathrm{T}}. \tag{3.1}$$

The transformation matrix for a 2-GS CANARY system (see Figure 2.15a) is shown in Figure 3.4. It has dimensions of 144×144 as each SHWFS has 36 sub-apertures that record centroids in orthogonal directions. An analytical covariance map ROI with subtracted

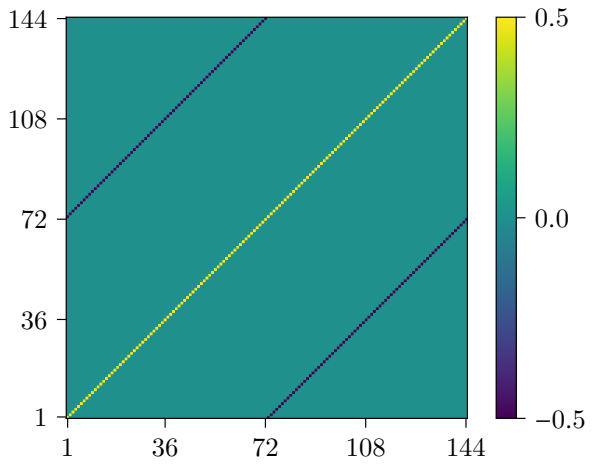

Figure 3.4: Transformation matrix, **T**, for a 2-GS CANARY system.

ground-layer isoplanatic turbulence can be calculated by averaging specific baselines within **B** (see Section 2.3.3.3). By subtracting ground-layer isoplanatic turbulence, the analytical model can therefore independently study turbulent layers at non-zero altitudes.

3.3 Covariance parametrisation of optical turbulence and Shack-Hartmann wavefront sensor misalignments

To measure the turbulence profile we use a fitting technique that first subtracts ground-layer isoplanatic turbulence. It has been shown that this approach is robust and that it minimises tomographic error (Martin et al., 2012). Learn 3 Step (L3S; Martin et al., 2016a) is another example of an advanced fitting technique that first subtracts ground-layer isoplanatic turbulence. The technique that we have developed derives from L3S and is referred to as CovAriance Parametrisation of optical Turbulence and SHWFS misalignments (CAPT; Laidlaw et al., 2018).

We use the Levenberg-Marquardt Algorithm (LMA; Levenberg, 1944) to iteratively fit an analytical model to SHWFS cross-covariance measurements (see Section 2.3.3.4). The software package we have developed is capable of using AO telemetry to measure the optical turbulence profile and SHWFS misalignments in real-time. The user chooses how many layers to fit and the altitudes at which these layers are fitted. Multiple GS combinations can be fitted to simultaneously. This software package is open-source* (example test cases are included in the open-source package). The software is written in Python and it uses the NumPy (Oliphant, 2006) and SciPy (Jones et al., 2001) libraries. The three steps of CAPT for an NGS system are as follows.

1. Using the transformation matrix, **T**, remove centroid common-motion and calculate the chosen cross-covariance array, e.g. a covariance matrix or a covariance map ROI.

*https://github.com/douglas-laidlaw/capt

The LMA fits to this cross-covariance array with analytically generated covariance that is ground-layer subtracted (see Section 3.2). The fit is performed by iteratively adjusting the vertical turbulence profile, $C_n^2(h)$. It is assumed that the outer scale for each layer is 25 m (see Section 2.3.3.6).

2. $C_n^2(h > 0)$ from point 1 is used to analytically generate a covariance array that dissociates ground-only turbulence from the complete cross-covariance array (the measured cross-covariance array with no ground-layer mitigation). The LMA fits analytically generated covariance to the measured ground-only cross-covariance array. The fit is performed by iteratively adjusting $C_n^2(0)$, $L_0(0)$ and vibration artefacts. Vibration artefacts are fitted as linear additions to xx and yy covariance (see Section 3.2).

3. Using the parameters recovered from points 1 and 2, the LMA fits analytically generated covariance to the complete cross-covariance array by iteratively adjusting SHWFS shift and rotation misalignments.

A block diagram of the CAPT fitting process is shown in Figure 3.5. As mentioned previously, the fitting technique we have adopted closely resembles L3S. The differences between CAPT and L3S are listed below.

- The first and second steps of L3S remove tip-tilt in both the measured and analytically generated cross-covariance arrays. We found that this did not improve the results and so tip-tilt removal was not included in the first and second steps of CAPT (CAPT 1 and CAPT 2, respectively).
- The first step of L3S fits $C_n^2(h > 0)$ and $L_0(h > 0)$. Although CAPT is capable of fitting an outer scale profile, we do not fit $L_0(h)$ for reasons discussed in Section 2.3.3.6. We fit $C_n^2(0)$ during CAPT 1 to help account for possible SHWFS misalignments. However, the measurement of $C_n^2(0)$ is taken from CAPT 2.
- The third step of L3S fits vibrational artefacts. We are able to complete this measurement in CAPT 2 as the system is not tip-tilt subtracted. L3S also fits xx, yy and xy vibration artefacts. CAPT does not fit xy vibrational artefacts as it assumes that these centroids are orthogonal and are therefore decorrelated.
- The third step of L3S fits SHWFS magnification. We do not fit this parameter during the third step of CAPT (CAPT 3) as this study concentrates on the parameterisation of SHWFS misalignments.

The outer scale measurement in CAPT 2 is not considered physical because it is likely that ground-layer turbulence is not fully developed (see Section 3.2). It is fitted to account for the likelihood that the ground-layer follows non-Kolmogorov statistics.

During CAPT 1 and CAPT 2, the covariance map ROI has its length and width equal to $L = n_\mathrm{d}$ and $W = 1$, respectively. During CAPT 3, $L = n_\mathrm{d} + 1$ and $W = 3$. The ROI in CAPT 3 is increased so that it has enough spatial information to detect SHWFS misalignments. These are the dimensions of the covariance map ROI unless stated otherwise. The

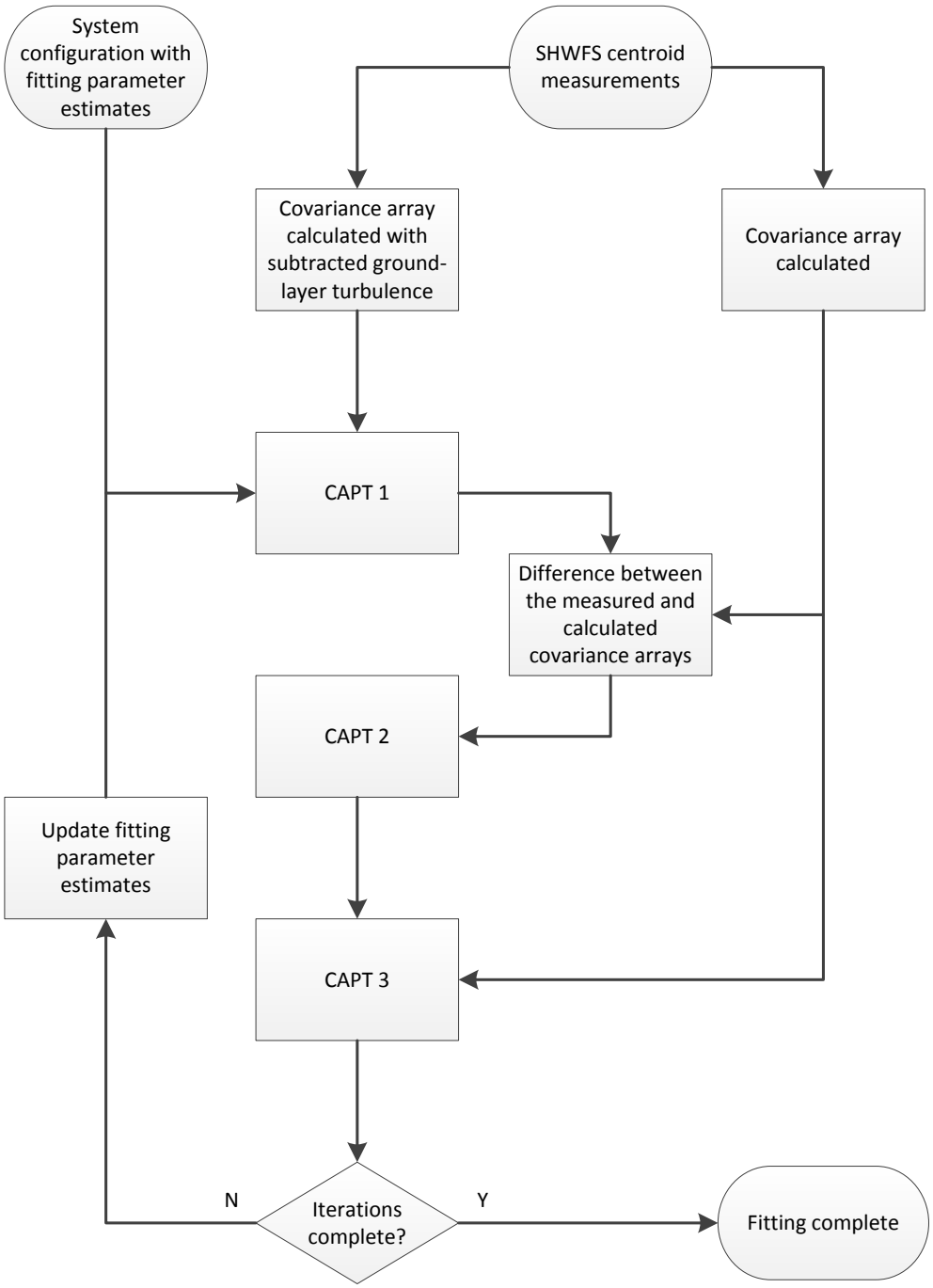

Figure 3.5: Block diagram of the steps involved in the CAPT fitting process.

noise-floor for $C_n^2(h)dh$ is set at $10^{-16}\,\mathrm{m}^{1/3}$, i.e. measurements of $C_n^2(h)dh < 10^{-16}\,\mathrm{m}^{1/3}$ are made equal to $10^{-16}\,\mathrm{m}^{1/3}$.

The uplink of LGSs through atmospheric turbulence results in the loss of tip-tilt information (see Section 2.2.1.2). This causes each SHWFS to have an independent tip-tilt term after CAPT 1 ground-layer mitigation. The result of this is a cross-covariance discontinuity within each xx and yy measurement. During LGS optical turbulence profiling, CAPT 1 fits linear additions to each xx and yy term to account for this discontinuity. In CAPT 2 this fitted parameter is used to help dissociate the ground-layer. It is also included during CAPT 3.

The vertical structure of the optical turbulence profile is dependent on sub-aperture separation. An unknown SHWFS misalignment will therefore directly impact the accuracy of CAPT. SHWFS shift and rotation misalignments are fitted during CAPT 3 however, the optical turbulence profile is recovered during CAPT 1 and CAPT 2. This implies that if an unknown misalignment exists between the SHWFSs, the optical turbulence profile will be imprecisely recovered which will lead to CAPT 3 being unable to recover systematic uncertainties. We found that a solution to this problem is to iterate through CAPT several times, i.e. run CAPT 1 and CAPT 2, take misalignment measurements from CAPT 3, put them back into CAPT and repeat (see Section 3.5). The idea is that, after a number of iterations, CAPT will converge on an accurate measurement of $C_n^2(h)$ and the SHWFS misalignments. At the first iteration every layer in the fitted model has a starting point of $r_0 = 0.2\,\mathrm{m}$ and $L_0 = 25\,\mathrm{m}$. Vibrational artefacts and SHWFS misalignments have a starting point of zero. As we iterate through CAPT a number of times, the starting point of each fitted parameter is equal to its measurement from the previous iteration (see Figure 3.5).

3.4 Shack-Hartmann wavefront sensor misalignments and the degradation of optical turbulence profiling

In a physical AO system it is unrealistic to assume perfect optical alignment. It is therefore important to quantify the degradation of covariance matrix and map ROI optical turbulence profiling in the presence of SHWFS misalignments. For CANARY, AOF, and ELT-scale configurations, a 2-NGS covariance matrix was analytically generated for 11 evenly-spaced SHWFS rotational misalignments. The maximum offset was 5°. The target covariance matrix (the covariance matrix that would be fitted to), $\mathbf{M}$, for each AO system was analytically generated with no noise. This allowed for perfect convergence of centroid cross-covariance measurements to be assumed. Each AO system had $\mathbf{M}$ generated with a NGS angular separation, θ, such that $h_{\max} = 24\,\mathrm{km}$. The NGS position angle in the Field of View (FOV) of the telescope was $\gamma = 0\,\mathrm{rad}$. Median atmospheric parameters documented by the European Southern Observatory (ESO; Kolb et al., 2015) were used to parametrise the optical turbulence profile. The integrated turbulence strength was equal to $r_0 = 0.1\,\mathrm{m}$ at $\lambda = 0.5\,\mu\mathrm{m}$. For consistency between each AO system, we chose to fit seven evenly-spaced layers from 0 to 24 km. The total number of measured layers is given by $N_\mathrm{L} = 7$. The measured altitudes are given by h_i^m, where i denotes the layer number,

i.e. $h_3^{\mathrm{m}} = 8\,\mathrm{km}$. The $C_n^2(h)$ profile for each $\mathbf{M}$ was calculated by binning the 35-layer ESO profile into these seven evenly-spaced layers, i.e. at each altitude the 35-layer ESO profile is integrated between $h_i^{\mathrm{m}} - b_{\mathrm{w}}/2$ and $h_i^{\mathrm{m}} + b_{\mathrm{w}}/2$, where b_{w} is the spacing between each fitted altitude. L_0 for each of the seven layers in $\mathbf{M}$ was 25 m. The parametrised and fitted altitudes were made equal to compensate for each telescope yielding a unique optical turbulence profile resolution (due to their SHWFS sub-aperture configuration). This meant that, for zero SHWFS misalignments in each AO system, both covariance matrix and map ROI fitting would recover the exact optical turbulence profile.

Covariance matrix CAPT was performed for each rotationally offset $\mathbf{M}$. The covariance map ROI was calculated from each $\mathbf{M}$ and covariance map ROI CAPT was also performed. For covariance matrix and map ROI fitting, CAPT assumed a rotational offset of zero. This allowed for the degradation of the measured optical turbulence profile to be monitored as a known rotational offset was introduced. The mean logarithmic deviation, F_{md}, between the fitted and parametrised profile was used to quantify the results. To account for the wide range of turbulence strengths, F_{md} was performed in logarithmic space such that

$$F_{\mathrm{md}} = \frac{1}{N_{\mathrm{L}}} \sum_{i=1}^{N_{\mathrm{L}}} \left| \log_{10} \left(C_n^2(h_i^{\mathrm{m}})^{\mathrm{m}} \Big/ C_n^2(h_i^{\mathrm{m}})^{\mathrm{r}} \right) \right|. \tag{3.2}$$

Put simply, $N_{\mathrm{L}} \cdot F_{\mathrm{md}}$ is the total order of magnitude difference between the measured and reference optical turbulence profiles ($C_n^2(h^{\mathrm{m}})^{\mathrm{m}}$ and $C_n^2(h^{\mathrm{m}})^{\mathrm{r}}$, respectively). In Equation 3.2, $C_n^2(h^{\mathrm{m}})^{\mathrm{r}}$ is the binned 35-layer ESO profile. The F_{md} results for an increasing SHWFS rotational misalignment are shown in Figure 3.6. For the CANARY system, the steep increase in covariance matrix F_{md} is seen as the optical turbulence profiling procedure begins to incorrectly detect zero turbulence at 24 km. The covariance map ROI does not suffer from this. AOF and ELT-scale F_{md} results favour the covariance matrix. The most likely reason for the covariance matrix being more robust is that its number of covariance measurements is inversely proportional to sub-aperture separation. This implies that small sub-aperture separations carry more weight during CAPT. Sub-apertures separated by the largest distance will be most affected by a rotational misalignment and so this weighting benefits covariance matrix fitting. We chose to not weight the covariance map ROI accordingly because in a real-world system this might amplify noise. In Figure 3.6, at a rotational offset of 5°, ELT-scale covariance matrix and map ROI fitting both have F_{md} values of approximately 0.65. However, at $F_{\mathrm{md}} = 0.65$, the measured turbulence profile is entirely unrepresentative of the reference turbulence profile. Therefore, this result is not significant. Furthermore, the plots shown in Figure 3.6 are specific to the parametrised optical turbulence profile, i.e. F_{md} results are dependent on $C_n^2(h_i^{\mathrm{m}})^{\mathrm{r}}$, θ and γ. F_{md} results will also be dependent on the AO system, e.g. sub-aperture diameter, s_{w}. The purpose of Figure 3.6 is to outline the scale of the problem when there is an unknown SHWFS rotational misalignment.

The same investigation was performed but for lateral shifts in SHWFS alignment, i.e. a shift misalignment equal in both x and y. The SHWFSs were conjugate to the pupil of the telescope (see Figure 2.13) and so the lateral shift was set as a function of telescope

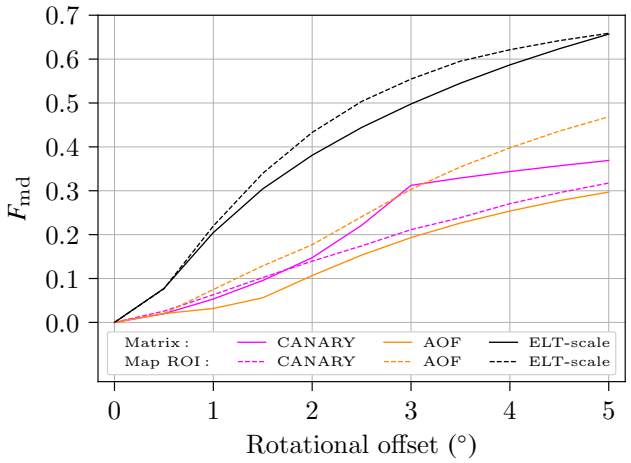

Figure 3.6: The degradation in the accuracy of matrix and map ROI optical turbulence profiling as a SHWFS rotation misalignment is introduced.

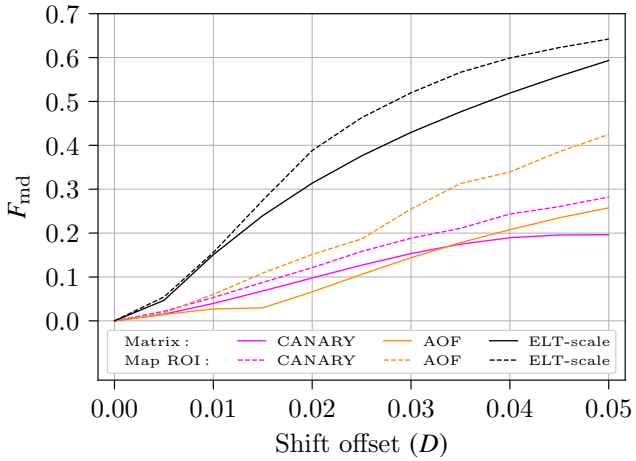

Figure 3.7: The degradation in the accuracy of matrix and map ROI optical turbulence profiling as a SHWFS shift misalignment is introduced.

diameter, D. Having the lateral shift as a function of D meant that the scale of the misalignment was proportional for each AO system. The maximum shift was set at an offset of $0.05\,D$. The results are shown in Figure 3.7. It is clear that there is a resemblance between Figures 3.6 and 3.7. The reason for this is that, in both cases, sub-aperture separation in x and y is dependent on D. This is also why the general trend is for larger telescopes to experience higher F_{md} values. It should again be noted that these F_{md} results are dependent on both the AO system and the parametrised turbulence profile.

To illustrate the degradation of the optical turbulence profile with increasing F_{md} values, $C_n^2(h_i^{\mathrm{m}})^{\mathrm{m}}$ is shown in Figure 3.8 for ELT-scale covariance matrix fitting at SHWFS shifts of 0.00, 0.02, and $0.05\,D$. These shifts correspond to F_{md} values of roughly 0.0, 0.3, and 0.6 (see Figure 3.7). They also correspond to integrated turbulence strengths of $r_0 = 0.10$,

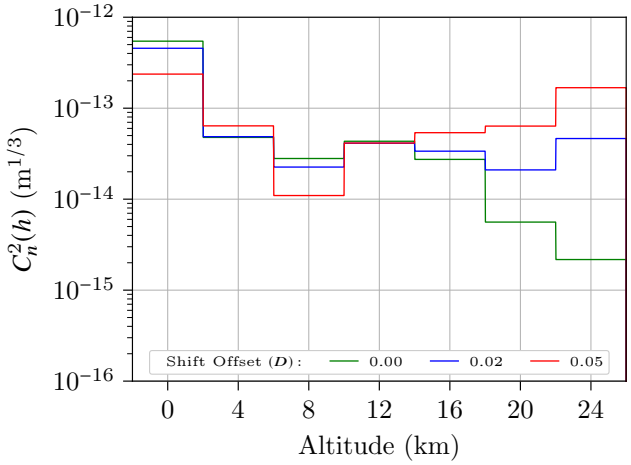

Figure 3.8: The degradation of ELT-scale covariance matrix turbulence profiling as a lateral shift misalignment is introduced. A shift offset of 0.00 D corresponds to $F_{\text{md}} = 0.0$, i.e. the measured turbulence profile is equal to the reference turbulence profile. Shift offsets of 0.02 and 0.05 D correspond to F_{md} values of approximately 0.3 and 0.6, respectively (see Figure 3.7).

0.10, and 0.11 m. It is therefore not suitable to use integrated r_0 as a measure of system performance. This is why F_{md} is the preferred metric for determining the accuracy of the turbulence profile measurement. $C_n^2(h_i^{\text{m}})^{\text{m}}$ at a shift misalignment of 0.00 D ($F_{\text{md}} = 0.0$) is synonymous with the reference optical turbulence profile, $C_n^2(h_i^{\text{m}})^{\text{r}}$. At a shift misalignment of 0.05 D the form of the reference optical turbulence profile has been completely lost. At a shift misalignment of 0.02 D ($F_{\text{md}} = 0.3$) $C_n^2(h_i^{\text{m}})^{\text{m}}$ is beginning to deviate from $C_n^2(h_i^{\text{m}})^{\text{r}}$ - especially at 20 and 24 km. CANARY and AOF reach this level of deviation when they are subject to either an unknown rotational or shift misalignment of around 5° and 0.05 D, respectively. For an ELT-scale system to achieve this level of accuracy, these values must be below 1.5° and 0.02 D. If an ELT-scale system can be optically aligned to this level of accuracy, the measured turbulence profile will not significantly deviate from the real turbulence profile. Alternatively, CAPT can measure and therefore compensate for SHWFS misalignments (see Section 3.5).

3.5 Measuring Shack-Hartmann wavefront sensor misalignments

SHWFS misalignments are a concern for reliably measuring the optical turbulence profile during CAPT 1 and CAPT 2, and are therefore problematic when estimating systematic misregistrations during CAPT 3. Using the same CANARY-scale configuration from Section 3.4, CAPT was performed for 200 datasets that had SHWFS misalignments in both rotation and lateral shift. The value of these misalignments were randomly generated from a uniform distribution. Rotation and shift misalignments had a range of −5° to 5° and −0.05 D to 0.05 D, respectively. Covariance matrix and map ROI CAPT was repeated 15 times for each dataset and F_{md} was calculated at each iteration. For CAPT 1 and CAPT 2

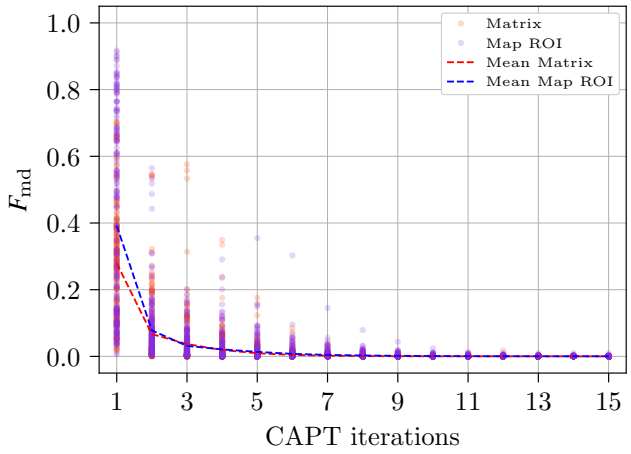

Figure 3.9: Covariance matrix and map ROI F_{md} for 200 datasets over 15 CAPT iterations. The results are shown for a CANARY 2-NGS configuration where the number of layers fitted is $N_{\mathrm{L}} = 7$. The SHWFSs in $\mathbf{M}$ were randomly misaligned in both rotation and lateral shift.

the ROI had $W = 1$ and $L = n_{\mathrm{d}}$. The ROI in CAPT 3 had $W = 3$ and $L = (n_{\mathrm{d}}+1)$ so that there was enough spatial information to fit SHWFS misalignments. F_{md} tending towards 0 implies that CAPT 1 and CAPT 2 are successfully measuring the reference turbulence profile, and that CAPT 3 is accurately measuring the misalignment between the SHWFSs. F_{md} will not equal 0 unless both of these conditions are satisfied. The results in Figure 3.9 show that both covariance matrix and map ROI fitting converge on the solution for all SHWFS misalignments.

The covariance matrix has a lower F_{md} value after the first CAPT iteration for reasons discussed in Section 3.4. On average, both the covariance matrix and map ROI accurately measure the SHWFS misalignment after the first iteration. The outliers imply that there are particular SHWFS misalignments that require a number of CAPT iterations. 15 CAPT iterations guarantees statistical convergence. Unless stated otherwise the remainder of this chapter will operate a system that iterates through CAPT 15 times. During the operation of a real-world system the idea is that SHWFS misalignments will not have to be fitted every time the optical turbulence profile is measured. SHWFS misalignments would be logged periodically so that only CAPT 1 and CAPT 2 have to be performed.

3.6 Turbulence profiling from simulated adaptive optics telemetry

This section investigates the quality of optical turbulence profiling that can be achieved by using CAPT with simulated AO telemetry. NGS SHWFS open-loop centroids were generated for the CANARY configuration in Soapy (see Section 2.2.7). The median results within the ESO documentation were used to parametrise the simulated 35-layer profile.

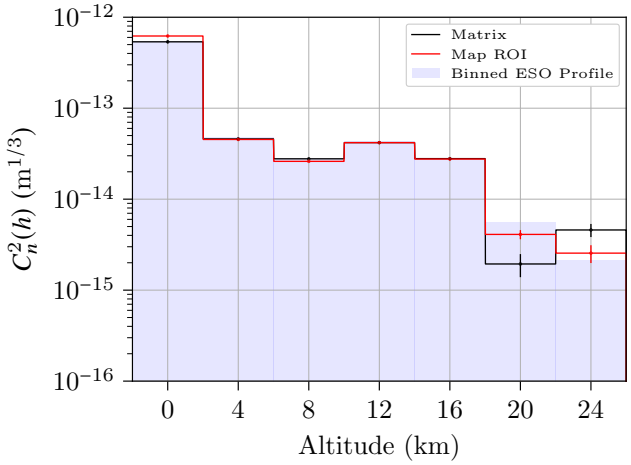

Figure 3.10: Covariance matrix and map ROI optical turbulence profiles from fitting to simulated NGS CANARY cross-covariance arrays. The mean $C_n^2(h_i^{\mathrm{m}})^{\mathrm{m}}$ profiles are shown along with $C_n^2(h_i^{\mathrm{m}})^{\mathrm{r}}$.

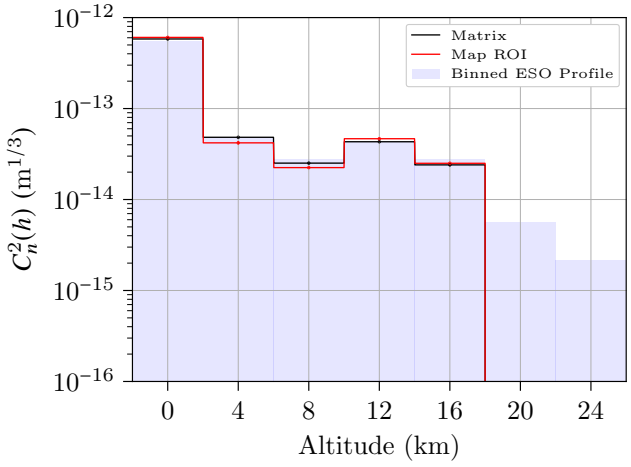

Figure 3.11: Covariance matrix and map ROI optical turbulence profiles from fitting to simulated LGS CANARY cross-covariance arrays. The mean $C_n^2(h_i^{\mathrm{m}})^{\mathrm{m}}$ profiles are shown along with $C_n^2(h_i^{\mathrm{m}})^{\mathrm{r}}$.

The integrated turbulence strength was equal to $r_0 = 0.1\,\mathrm{m}$ at $\lambda = 0.5\,\mu\mathrm{m}$ and L_0 at each of the 35 layers was 25 m. Four optically aligned 7×7 SHWFSs observing independent NGSs at zenith were simulated. The six NGS combinations had position angles of $\gamma = 0$, 45, 90, 90, 135 and 180°. The 4-NGS system had a square layout with $h_{\mathrm{max}} = 24\,\mathrm{km}$. On-sky NGS observations rarely adhere to having such a well-ordered asterism. However, the simulated square layout is an appropriate approximation (see Section 5.2). The values in the Soapy configuration file were the same as those listed in Table 2.2. The simulation was repeated 10 times so that mean CAPT results along with their standard error could be calculated.

Covariance matrix and map ROI fitting procedures were performed on their respective

Table 3.1: Covariance matrix and map ROI optical turbulence profiling results from fitting to simulated NGS and LGS CANARY cross-covariance arrays.

	F_{md}		
	NGS, 0 to 24 km	NGS, 0 to 16 km	LGS, 0 to 16 km
Matrix	0.19 ± 0.03	0.02 ± 0.00	0.03 ± 0.00
Map ROI	0.13 ± 0.03	0.03 ± 0.00	0.05 ± 0.00

cross-covariance arrays. The six SHWFS combinations were fitted to simultaneously. Each algorithm fitted seven evenly-spaced layers from 0 to 24 km. Vibration artefacts and SHWFS misalignments were not included in the simulation and were therefore measured to be negligible. The 35-layer ESO profile was binned to the fitted altitudes so that the measured optical turbulence profile could be compared to a reference. F_{md} was used to quantify profiling accuracy (see Section 3.4). The results are given in Table 3.1. In Figure 3.10, the mean of the measured turbulence profiles is shown alongside the reference turbulence profile. The most noticeable difference between covariance matrix and map ROI optical turbulence profiling is at 20 and 24 km. As there are a reduced number of optical turbulence profile measurements at higher altitudes, the most probable cause for the covariance map ROI being more accurate is that it only considers the highest Signal-to-Noise Ratio (SNR) measurements (see Section 2.3.3.3). If only the first five layers are considered (0 to 16 km; see Table 3.1), covariance matrix fitting is more accurate due to its ground-layer measurement. This is likely caused by autocovariance measurements constraining the model during CAPT 2. However, by studying Figure 3.10, there is little difference in the F_{md} results when analysing the layers fitted from 0 to 16 km.

The NGS study was repeated for sodium LGSs. All of the system parameters were the same except for the apparent magnitude of each LGS in the V band. This was set to 8. Each LGS was side-launched and focussed at an altitude of 90 km. The SHWFSs were simulated to measure at a wavelength of 589 nm (see Section 2.2.1.2). Figure 3.10 is repeated for the LGS results in Figure 3.11. Due to the cone effect, the maximum altitude of sub-aperture optical path intersection was reduced to roughly 19 km. Therefore, a layer was not fitted at 24 km as the turbulence at this altitude is unsensed. The layer fitted at 20 km is not included in the analysis of the measured optical turbulence profile as its bin is centred above the maximum altitude of sub-aperture optical path intersection. The LGS F_{md} results are summarised in Table 3.1. There is little difference between covariance matrix and map ROI fitting.

To investigate whether the covariance map ROI has an optimal size for recovering the optical turbulence profile, CAPT was repeated on the simulated NGS centroids but for all possible ROI widths and lengths. For consistency – and because it was shown to be sufficient in Section 3.5 – the ROI during CAPT 3 kept values of $W = 3$ and $L = (n_{\mathrm{d}} + 1)$. F_{md} is plotted as a function of W and L in Figure 3.12. The trend in Figure 3.12 indicates that profiling accuracy degrades as the ROI considers a greater number of baselines at $W > 1$. This is attributed to the data points along the GS position angle, γ, having the highest SNR. The lowest and highest values within Figure 3.12 are found at $L, W = (11, 1)$

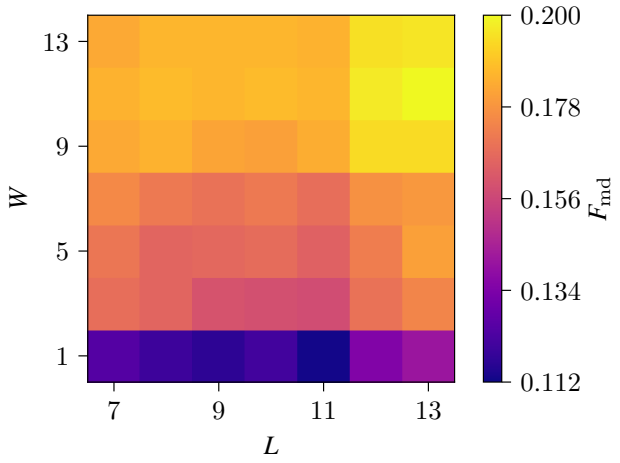

Figure 3.12: Mean deviation, F_{md}, shown as a function of covariance map ROI length, L, and width, W. The results are from CAPT analysis of simulated NGS CANARY data. The turbulence profile reference was the binned form of the 35-layer ESO profile.

and $L, W = (13, 12)$, respectively, where F_{md} equals 0.11 ± 0.04 and 0.20 ± 0.04. It should be remembered that the 35 simulated layers had $L_0 = 25\,\mathrm{m}$. During CAPT 1 it was also assumed that each of the fitted layers have $L_0 = 25\,\mathrm{m}$. As mentioned previously, an ROI of $W = 1$ has reduced $L_0(h)$ information. We can therefore not conclude whether an ELT-scale system would show a similar trend to Figure 3.12. If an ELT-scale system is required to measure $L_0(h)$, it might be beneficial for the covariance map ROI to have a width greater than $W = 1$.

3.7 Computational requirements and efficiency improvements

We have developed detailed algorithms to optimise the efficiency of CAPT. In this section we outline the computational requirements for analytically generating a covariance matrix and a covariance map ROI. We then compare the efficiency of each fitting routine when applied a CANARY, AOF and ELT-scale AO system.

3.7.1 Computational requirements for analytically generating a covariance matrix and map region of interest

For SHWFSs with the same dimensions (in units of sub-apertures), there is a considerable amount of repetition in an analytically generated covariance matrix, e.g. in Figure 2.15a, x_1x_2 is a reflection of x_2x_1 and $x_1x_1 = x_2x_2$. Orthogonal centroid covariance is also repeated for each SHWFS pairing, e.g. $x_1y_2 = x_2y_1$. When accounting for SHWFS misalignments, the number of calculations required to analytically generate a covariance matrix is

$$N_{\mathrm{m}} = 3N_{\mathrm{L}}\left(k_{\mathrm{c}}n_{\mathrm{s}}^2 + m_{\mathrm{n}}\right). \tag{3.3}$$

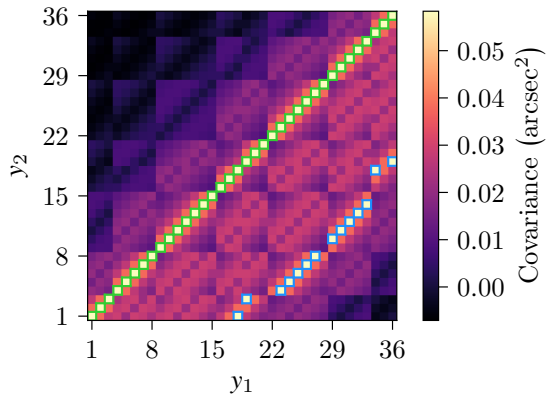

(a) Analytically generated covariance matrix MR (see Section 3.1) with the same parameters used to simulate Figure 2.15a. Outlined in green are the 36 analytically generated data points that are averaged to baseline $x_{\text{sep}}, y_{\text{sep}} = (0, 0)$. Outlined in blue are the 14 data points that are averaged to the baseline $x_{\text{sep}}, y_{\text{sep}} = (0, 3)$.

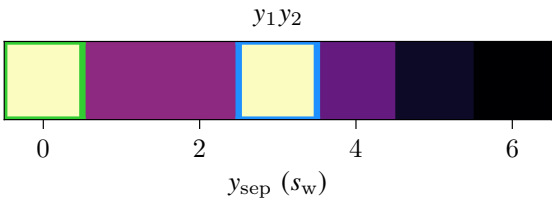

(b) The covariance map ROI from (a). Sub-aperture separations are outlined in green and blue accordingly.

Figure 3.13: Required data points for generating a y_1y_2 covariance map ROI that can account for SHWFS misalignments.

In Equation 3.3, k_{c} represents the number of GS combinations. The number of sub-apertures and sub-aperture baselines in each SHWFS is given by n_{s} and m_{n}, respectively. The first term in Equation 3.3, $3N_{\text{L}}k_{\text{c}}n_{\text{s}}^2$, states that, for every layer in each GS combination, the algorithm must make as many calculation as there are data points in 3 MRs (the factor of 3 comes from xx, yy and xy covariance). Autocovariance regions are insensitive to SHWFS misalignments and so they require as many calculations as they have baselines, i.e. autocovariance regions are Toeplitz matrices. This gives the second term in Equation 3.3, $3N_{\text{L}}m_{\text{n}}$.

Only specific sub-aperture combinations have to be considered when analytically generating the baseline values within a covariance map ROI. For a system that can compensate for SHWFS misalignments, each data point within the covariance map ROI must be the baseline average of all analytically generated covariance values. This is because misaligned SHWFSs will have baselines comprised of independent sub-aperture separations. This averaging is the same process that was outlined in Section 2.3.3.2, however, the model instead averages analytically generated covariance. This is illustrated in Figure 3.13. It follows that only specific covariance data points need to be analytically generated to perform the operation of $\mathbf{T}$ during CAPT 1 (see Sections 3.2 and 3.3). First, the covariance map ROI

must be analytically generated along each value of γ for every GS combination. The autocovariance map ROI for each GS combination must also be generated. A further requirement is that, for each of these combinations, the covariance of all sub-aperture separations that lie along γ and $\gamma + \pi$ must be generated, i.e. $L = (2n_\mathrm{d} - 1)$. There is no mathematical expression for analytical covariance map ROI common-motion subtraction. To perform this operation we have simply created an algorithm that analytically generates only the required covariance data points. These data points are then used to perform the equivalent operation of Equation 3.1 on the covariance map ROI. The number of calculations required to analytically generate a covariance map ROI that can account for SHWFS misalignments during CAPT 1 is

$$N_\mathrm{r} = 2N_\mathrm{L}k_\mathrm{c}^2\left(2r_\mathrm{n} - n_\mathrm{s} + \frac{2n_\mathrm{d} - 1}{k_\mathrm{c}}\right). \tag{3.4}$$

r_n is the number of sub-aperture separation pairings that are within one axis of the covariance map ROI along γ. r_n is independent of L. The second half of Equation 3.4, $2N_\mathrm{L}k_\mathrm{c}(2n_\mathrm{d} - 1)$, is the expression for the number of calculations required to generate the autocovariance regions. The factor of 2 comes from xx and yy axes being considered. Autocovariance regions are insensitive to SHWFS misalignments, giving the term for the length of the ROI, $2n_\mathrm{d} - 1$. The first half of Equation 3.4, $2N_\mathrm{L}k_\mathrm{c}^2(2r_\mathrm{n} - n_\mathrm{s})$, comes from covariance regions that detail the turbulence profile. The first half requires k_c^2 because, for every GS combination, it calculates the ROI at every γ combination. The term $2r_\mathrm{n} - n_\mathrm{s}$ is the number of sub-aperture separation pairings when $L = 2n_\mathrm{d} - 1$.

The number of calculations required to generate a covariance map ROI during CAPT 2 is $2k_\mathrm{c}s_\mathrm{n}$. s_n is the number of sub-aperture separation pairings that are within one axis of the covariance map ROI, e.g. Figure 3.13a can be used to determine that Figure 3.13b has $s_\mathrm{n} = 36 + 28 + 21 + 14 + 11 + 6 + 3 = 119$. The difference between s_n and r_n is that s_n is dependent on L. The number of calculations required to generate a covariance map ROI during CAPT 3 is $2N_\mathrm{L}k_\mathrm{c}s_\mathrm{n}$. If CAPT 3 considers a larger ROI this will increase the value of s_n.

If misalignments are accounted for, Figure 3.14a shows the number of calculations required to generate a single-layer covariance matrix and map ROI during CAPT 1. These are plotted for CANARY, AOF, and ELT-scale AO systems, if each were operating a 2, 4 and 6 GS configuration. The ROI for each AO system has $L = n_\mathrm{d}$ and $W = 1$. As the algorithms consider an increased number of baselines, the number of required calculations increases at a greater rate for the covariance matrix. This makes the reduced computational strain offered by the covariance map ROI especially appealing for ELT-scale instruments. During CAPT 1 it should also be noted that as the system assumes a known outer scale profile, the covariance calculations only need to be performed once. Thereafter, CAPT can iteratively fit the overall strength of the optical turbulence profile. The plot shown in Figure 3.14a is repeated for CAPT 2 and CAPT 3 in Figures 3.14b and 3.14c, respectively. The ROI for the AO systems in Figure 3.14b has $L = n_\mathrm{d}$ and $W = 1$. In Figure 3.14c, $L = (n_\mathrm{d} + 1)$ and $W = 3$.

In an optically aligned system, two-dimensional sub-aperture separation is directly related

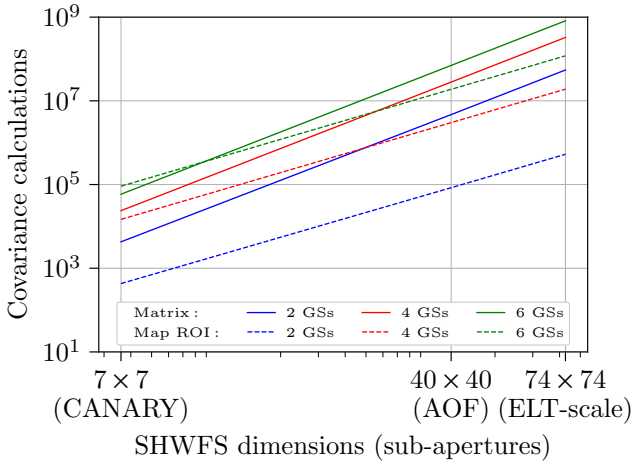

(a) The number of calculations during CAPT 1. The ROI has $L = n_\mathrm{d}$ and $W = 1$.

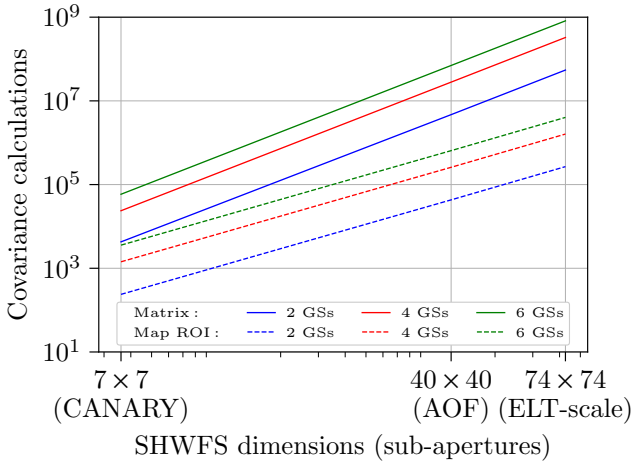

(b) The number of calculations during CAPT 2. The ROI has $L = n_\mathrm{d}$ and $W = 1$.

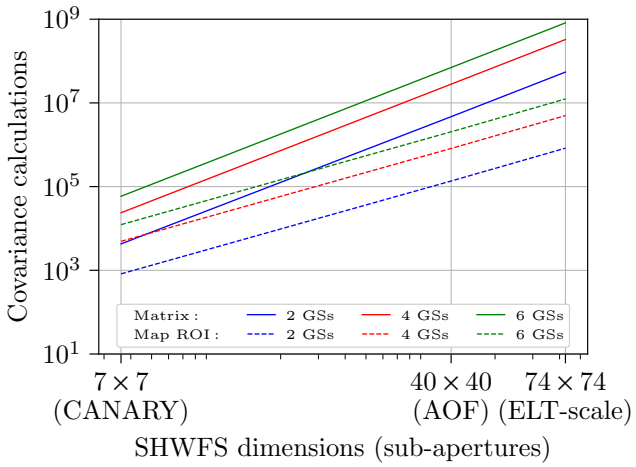

(c) The number of calculations during CAPT 3. The ROI has $L = (n_\mathrm{d} + 1)$ and $W = 3$.

Figure 3.14: The number of calculations to generate a $N_\mathrm{L} = 1$ covariance matrix and map ROI during each stage of the CAPT fitting process.

to its baseline value. This results in many identical values throughout each region of an analytically generated covariance matrix, i.e. each pairing of SHWFS axes (for example, x_1x_2) is a Toeplitz matrix. This implies that covariance maps can be analytically generated directly. If Figure 2.15a was analytically generated for an optically aligned system, all x_1x_2 and y_1y_2 values could be found within Figure 2.15b. The number of calculations required to generate a covariance matrix for optically aligned SHWFSs is equal to Equation 3.3, but with $n_\mathrm{s} = \sqrt{m_\mathrm{n}}$. A further implication of this is that, for each layer, the generation of a covariance map ROI requires as many calculations as it has baselines. For a system that is assumed optically aligned, Equation 3.4 will have $r_\mathrm{n} = (2n_\mathrm{d} - 1 + n_\mathrm{s})/2$. The number of calculations required to generate a covariance map ROI in CAPT 2 becomes $2k_\mathrm{c}LW$.

3.7.2 Demonstration of computational efficiency

The overall computational efficiency of 2-NGS covariance matrix and map ROI optical turbulence profiling is shown here for a CANARY, AOF, and ELT-scale AO system. The target covariance matrix, $\mathbf{M}$, for each AO system had zero SHWFS misalignments. These were the same of those used in Section 3.4. The covariance map ROI was calculated from each $\mathbf{M}$. Seven evenly-spaced turbulent layers were to be fitted from 0 to 24 km. $\mathbf{M}$ was generated for perfectly aligned SHWFSs and, therefore, covariance matrix and map ROI fitting would recover the exact optical turbulence profile. This meant that the efficiency of CAPT would be primarily dependent on computational strain. CAPT covariance matrix and map ROI optical turbulence profiling was timed for the CANARY, AOF, and ELT-scale systems. To start, CAPT assumed perfect optical alignment, i.e. the number of covariance calculations was reduced to a minimum (see Section 3.7.1). Only CAPT 1 and CAPT 2 can be performed in a system that assumes SHWFS optical alignment. To test computational requirements against computational efficiency, CAPT did not take advantage of parallel computing. The fitting process was operated on a Dell Precision Tower 3620 workstation with an Intel Core i7-6700 CPU processor and 64 GB of RAM. The fitting routines were each repeated five times. The standard error of each routine was negligible. Table 3.2 summarises the timing results.

The study was repeated but with CAPT accounting for SHWFS misalignments, i.e. a system that can no longer take advantage of Toeplitz matrix symmetry outside of autocovariance regions (see Section 3.7.1). To test the efficiency against a CAPT system that assumes perfect optical alignment, the analytically generated covariance arrays had zero SHWFS misalignments during CAPT 1 and CAPT 2. The processing time for each step of CAPT is shown in Figure 3.15. Table 3.3 summarises the timing results. The comparison between Tables 3.2 and 3.3 outlines the loss in computational efficiency when SHWFS misalignments are accounted for. In Figure 3.15, all AO systems record CAPT 2 being the fastest stage of CAPT. This is because it is only fitting one layer. CAPT 3 is the most computationally demanding stage as each iteration requires the recalculation of sub-aperture covariance for seven layers. In the fitted model, the starting point for SHWFS misalignments is zero. The target covariance matrix, $\mathbf{M}$, was generated for per-

Table 3.2: CAPT fitting time for covariance matrix and map ROI algorithms that assume an optically aligned system. The results are for a 2-NGS system where $N_{\mathrm{L}} = 7$. Optical turbulence profiling occurs during CAPT 1 and CAPT 2 (CAPT 1+2).

	Time Taken (s)	
	Matrix	Map ROI
AO System	CAPT 1+2	CAPT 1+2
CANARY	0.09	0.02
AOF	381.14	0.04
ELT-scale	1.12×10^4	0.21

Table 3.3: CAPT fitting time for covariance matrix and map ROI algorithms that are accounting for SHWFS misalignments. The results are for a 2-NGS system where $N_{\mathrm{L}} = 7$. Optical turbulence profiling occurs during CAPT 1 and CAPT 2 (CAPT 1+2). SHWFS misalignments are fitted during CAPT 3.

	Time Taken (s)			
	Matrix		Map ROI	
AO System	CAPT 1+2	CAPT 3	CAPT 1+2	CAPT 3
CANARY	0.1	0.67	0.02	0.19
AOF	454.17	801.41	0.56	10.06
ELT-scale	1.21×10^4	1.27×10^4	5.93	338.52

fectly aligned SHWFSs and so CAPT 3 will measure SHWFS misalignments to be zero. Having the starting point for fitting equal to the measurement does not significantly reduce computing time as the LMA in CAPT 3 still has to perform local optimisation.

For CANARY, the efficiency of covariance matrix optical turbulence profiling is not an issue. For the AOF, the covariance matrix fitting procedure takes over 20 minutes. For the ELT-scale system, covariance matrix CAPT takes almost 7 hours. The covariance map ROI reduces ELT-scale CAPT processing time to under 6 minutes, i.e. it improves the computational efficiency of the ELT-scale system by a factor of 72. If SHWFS misalignments have already been logged (see Section 3.5) then the covariance map ROI can perform ELT-scale CAPT optical turbulence profiling (CAPT 1 and CAPT 2) in under 6 seconds. As mentioned throughout, ELT-scale covariance map ROI data analysis might require $W > 1$ for $L_0(h)$ fitting. This will increase the processing times presented, however, using the covariance map ROI for SLODAR data analysis will still be the most efficient technique.

3.8 Summary

To achieve optimal performance, forthcoming ELT AO systems will require efficient, high-precision measurements of the optical turbulence profile. This investigation looked at the differences between using the CAPT fitting procedure for covariance matrix and map ROI optical turbulence profiling. Both techniques were tested under SHWFS misalignments for CANARY, AOF, and ELT-scale AO systems. SHWFS misalignments were shown to significantly degrade the accuracy of optical turbulence profiling. An ELT-scale system measured F_{md} values of approximately 0.6 when SHWFSs were misaligned by a rotation

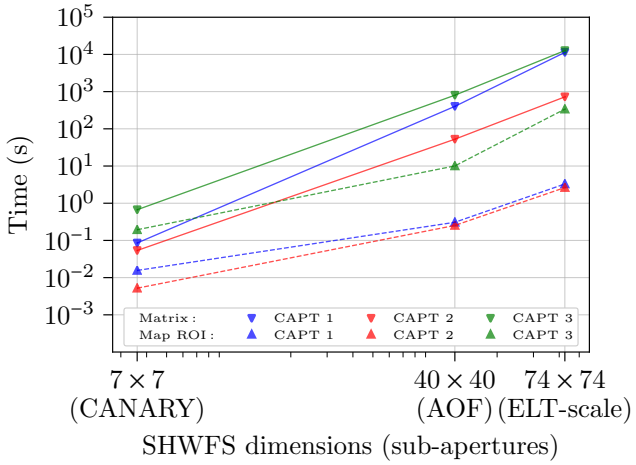

Figure 3.15: Covariance matrix and map ROI fitting times when accounting for SHWFS misalignments. The configuration concerns a 2-NGS system and the fitting of seven layers. Line plots have been overlaid to indicate the general trend across different AO systems.

of 5° or a lateral shift of $0.05\,D$. However, it was also shown that, by iterating through CAPT a number of times, both the covariance matrix and map ROI can measure SHWFS misalignments. We recommend 15 iterations.

Using simulated data for a 4-NGS CANARY system, covariance matrix and map ROI CAPT measured F_{md} to be 0.19 ± 0.03 and 0.13 ± 0.03, respectively. Both techniques were also shown to be applicable to LGS analysis. Results from the simulated data showed that the optimal covariance map ROI has a width of $W = 1$. It was also shown that, compared to the covariance matrix, the covariance map ROI improves the efficiency of an ELT-scale system by a factor of 72.

The covariance map ROI is capable of measuring SHWFS misalignments using an iterative CAPT approach. Using the fitting routine presented, it outperforms the accuracy of covariance matrix optical turbulence profiling. In addition, the covariance map ROI improves the efficiency of an ELT-scale system by almost two orders of magnitude. We conclude from this chapter that AO telemetry optical turbulence profiling should twin CAPT with covariance map ROI data analysis.

— 4 —

Wind velocity profiling from adaptive optics telemetry

The measured wavefront continuously evolves as the wind moves atmospheric turbulence across the light-path of the telescope. The wind speed profile can be used to calculate the required frequency for an Adaptive Optics (AO) system (see Section 2.2.4). Predictive control algorithms can reduce temporal errors by mitigating the latency between the measurement of a wavefront and its successive Deformable Mirror (DM) correction. These algorithms commonly require optical turbulence and wind velocity profile information (Sivo et al., 2014; Jackson et al., 2015). Wind velocity information can also be used to study the Taylor frozen-flow hypothesis (Schöck and Spillar, 2007; Guesalaga et al., 2014).

As discussed in Section 2.3.3.5, calculating the cross-covariance between temporally offset Shack–Hartmann Wavefront Sensor (SHWFS) centroids demonstrates the wind velocity profile. These centroids must be recorded in open-loop or pseudo open-loop (see Section 2.2.4). In the covariance map, this temporal offset causes individual layers to be displaced. Each displacement within a temporally offset covariance map corresponds to the velocity of a specific turbulent layer. It has been shown that, within a spatio-temporal cross-covariance array, the wind velocity profile can be recovered by tracking peaks corresponding to individual turbulent layers (Wang et al., 2008; Osborn et al., 2017; Sivo et al., 2018; Laidlaw et al., 2019). However, current AO systems have a limited altitude-resolution due to their number of SHWFS sub-apertures. Having a limited altitude-resolution results in wind velocity information becoming quickly entangled as individual layers can travel in various directions with different speeds. This makes it difficult to write an algorithm for automated peak tracking. It is also a challenge to track cross-covariance values that can be spread between the baselines of a covariance map (Wang et al., 2008; Sivo et al., 2018; Laidlaw et al., 2019).

In this section we introduce a novel technique for automated wind velocity profiling from AO telemetry. It makes use of the recommend AO parameter estimation technique from Chapter 3, that we use to measure the optical turbulence profile, SHWFS misalignments and vibration artefacts. Once parameter estimation is complete, a temporally offset covariance map can be fitted to by each analytically generated layer running its altitude and baseline position as a free parameter. If frozen-flow is assumed, the change in covariance map location for each layer is synonymous with its velocity (see Figure 2.16). In Section 4.4 we analyse simulated data from CANARY, the AO demonstrator for Extremely Large Telescope-scale (ELT-scale) technologies on the 4.2 m William Herschel Telescope

(WHT; see Section 2.4.1), La Palma. A qualitative study of the wind velocity profiling technique is carried out using simulated Natural Guide Star (NGS) and Laser Guide Star (LGS) data.

4.1 Covariance parametrisation of wind velocity

The SLOpe Detection And Ranging (SLODAR) technique for demonstrating the wind velocity profile is outlined in Section 2.3.3.5. The measured covariance map array with no temporal offset is referred to as M_0. The measured covariance map array after positive and negative temporal offsets is referred to as $M_{\delta t}$, where δt is the size of the temporal offset.

The key to spatio-temporal wind velocity profiling is being able to track turbulent layers from M_0 to $M_{\delta t}$. We have developed a technique that uses the Levenberg-Marquardt Algorithm (LMA; Levenberg, 1944) to iteratively fit an analytical model to temporally offset SHWFS cross-covariance measurements. Multiple NGS or LGS combinations can be fitted to simultaneously and the user decides how many layers to fit and at which altitudes. The model we use for analytically generating sub-aperture covariance is the same as that used by CovAriance Parametrisation of optical Turbulence and SHWFS misalignments (CAPT; Laidlaw et al., 2018; see Section 3.3). The fitting algorithm assumes each layer obeys Taylor frozen-flow. We refer to this wind velocity profiling technique as CovAriance parametrisation of Wind velocity (CAW; Laidlaw et al., 2019). CAW was written to run alongside CAPT and can therefore be implemented on any tomographic AO system. The CAW software package is open-source* (example test cases are included in the open-source package). All of the open-source algorithms are written in Python using the NumPy (Oliphant, 2006) and SciPy (Jones et al., 2001) libraries. The 3 steps of CAW are as follows:

1. Use CAPT to measure the optical turbulence profile along with SHWFS misalignments and vibration artefacts, i.e. the recommended technique outlined in Chapter 3.

2. The temporally offset covariance map array is calculated for SHWFS centroids with subtracted ground-layer isoplanatic turbulence (see Sections 2.3.3.5 and 3.2). The LMA takes $C_n^2(h > 0)$, $L_0(h > 0)$ and SHWFS misalignments from point 1, and fits the wind velocity profile at non-zero altitudes by each analytically generated layer running h, x_{sep} and y_{sep} as a free parameter. The positive and negative temporally offset covariance map arrays are fitted to simultaneously, i.e. the negatively offset covariance map is fitted to by analytically generated layers with the same parameters but at all values of h, $-x_{\text{sep}}$ and $-y_{\text{sep}}$.

3. Wind velocity profile information from point 2 is used in conjunction with parameter estimation from point 1 to analytically generate a covariance map array that dissociates the ground-layer from $M_{\delta t}$. The LMA then takes SHWFS misalignments, vibration artefacts, $C_n^2(0)$ and $L_0(0)$ from point 1, and fits to ground-layer $M_{\delta t}$. It

*https://github.com/douglas-laidlaw/caw

does this by fitting the analytically generated ground-layer with h, x_{sep} and y_{sep} as free parameters. As in point 2, the positive and negative temporally offset covariance map arrays are fitted to simultaneously.

A block diagram of the CAW fitting process is shown in Figure 4.1. In the first step of CAW (CAW 1), each of the fitted altitudes measure the integrated turbulence strength across an altitude range. Within this altitude range, the wind speed and direction, $w_{\text{s}}(h)$ and $w_{\text{d}}(h)$, respectively, will not necessarily be constant. This means that the wind velocity profile in $M_{\delta t}$ might not primarily originate from the altitudes set in CAW 1. This is why h needs to be fitted in conjunction with x_{sep} and y_{sep} during the second and third step of CAW (CAW 2 and CAW 3, respectively). The $C_n^2(h)dh$ noise-floor in CAW 1 is $1 \times 10^{-16}\,\text{m}^{1/3}$. Only $C_n^2(h)$ values greater than the noise-floor are fitted during CAW 2 and CAW 3.

The difference between CAW and peak tracking (outlined in Section 2.3.2.2) is that, for each layer, peak tracking is trying to best-fit a specific value within $M_{\delta t}$. CAW is using the ability to analytically generate sub-aperture covariance to find the 2D least-squares minimum of the entire temporally offset covariance map array. This means that every data point within $M_{\delta t}$ contributes to the detection of a wind velocity measurement - we are not just tracking peaks. CAW is also resistant to turbulent layer cross-covariance being displaced to non-integer baselines. Figure 2.16 is repeated in Figure 4.2a. It can be imagined that Figure 4.2a is the ground-only $M_{\delta t}$ that is fitted to during CAW 3. The analytical fit to Figure 4.2a is shown in Figure 4.2b. It is important to note the limits of x_{sep} and y_{sep} in Figure 4.2. We denote the change in x_{sep} and y_{sep} for each turbulent layer as $\Delta x_{\text{sep}}(h)$ and $\Delta y_{\text{sep}}(h)$. The wind speed profile is therefore given by

$$w_{\text{s}}(h) = \frac{\sqrt{\Delta x_{\text{sep}}(h)^2 + \Delta y_{\text{sep}}(h)^2}}{\delta t}. \tag{4.1}$$

The wind direction profile can be calculated from the individual magnitudes of $\Delta x_{\text{sep}}(h)$ and $\Delta y_{\text{sep}}(h)$.

It should be noted that multiple temporal offset covariance maps can be fitted to simultaneously. It is thought that by fitting to multiple temporal offsets, CAW might be more robust to frozen-flow fragmentation. We do not study multiple temporal offsets in this chapter as our Soapy simulations abide frozen-flow. Instead, this investigation is carried out using on-sky data in Section 5.1.2. In Section 5.1.2 we also study the optimal temporal offset.

4.2 Wind shear

Across each altitude range fitted during CAW 1, $w_{\text{s}}(h)$ and $w_{\text{d}}(h)$ will not necessarily be constant. In on-sky observations, what is measured as a single layer in M_0 can sometimes split into 2 of more layers in $M_{\delta t}$ (Osborn et al., 2017). This process of $C_n^2(h)$ dispersion is known as wind shear. Peak tracking and CAW both assume that each turbulence profile measurement has a constant wind velocity. They are unable to account for wind shear

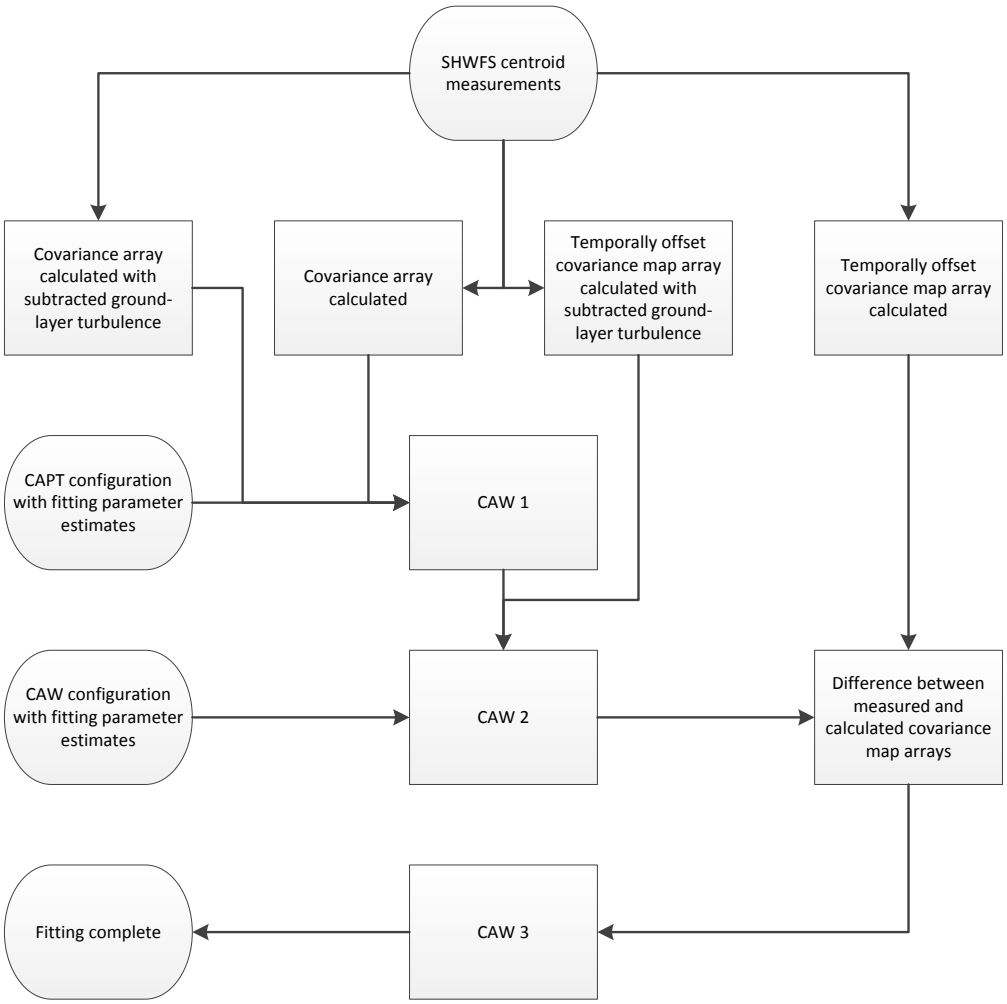

Figure 4.1: Block diagram of the steps involved in the CAW fitting process.

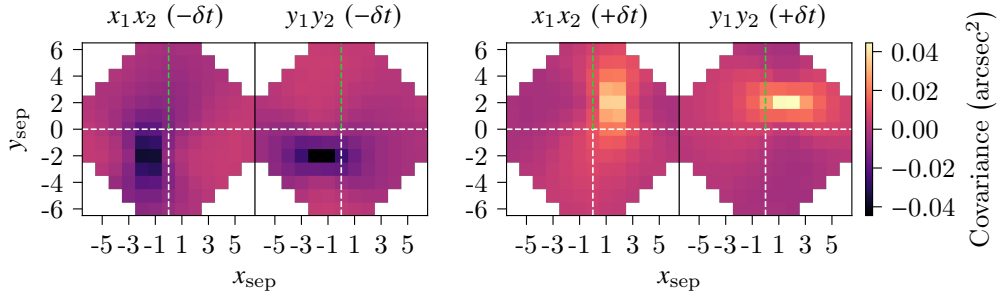

(a) Temporally offset covariance maps from simulated SHWFS centroids for $N_{\text{L}} = 1$ at 0 km. The layer is characterised by $r_0 = 0.1\,\text{m}$ (at $\lambda = 0.5\,\mu\text{m}$) and $L_0 = 25\,\text{m}$. Broken lines have been overlaid to indicate $x_{\text{sep}}, y_{\text{sep}} = (0, 0)$ (white) and the GS position angle, γ (green).

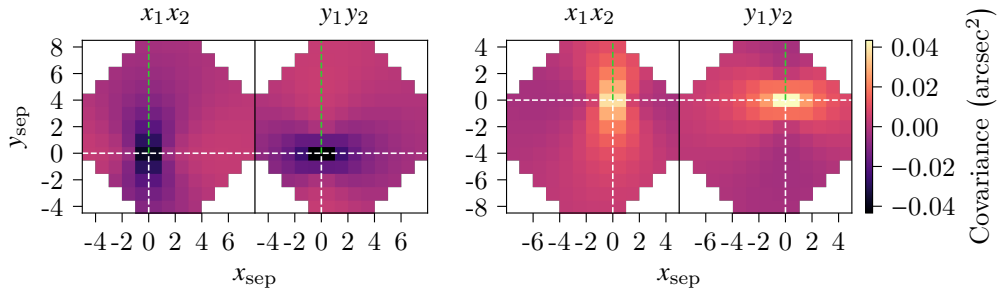

(b) The LMA fit to (a). Analytical covariance has been used to fit to the measured ground-layer by iteratively adjusting h, x_{sep} and y_{sep}. Broken lines have been overlaid to indicate $x_{\text{sep}}, y_{\text{sep}} = (0, 0)$ (white) and the GS position angle, γ (green).

Figure 4.2: The process by which CAW iteratively fits the wind velocity profile.

because the range of $w_{\text{s}}(h)$ and $w_{\text{d}}(h)$ is unknown. Furthermore, it is not possible to predetermine how the turbulence strength is divided between the dispersed layers. If wind shear occurs during peak tracking, the wind velocity at that specific altitude is unresolved. However, as CAW is a least-squares fitting algorithm, it will always return a value. In this section we study how wind shear influences the wind velocity profiling results from CAW.

Figure 4.3 illustrates the process of wind shear (in either xx or yy covariance-space). At a temporal offset of $\delta t = 0$, the turbulence strength is $C_n^2(h)_0$. After a positive temporal offset, $+\delta t$, the integrated turbulence strength at $C_n^2(h)_0$ is shown to come from two individual layers such that $C_n^2(h)_1 + C_n^2(h)_2 = C_n^2(h)_0$. The dispersed layers have independent wind velocities. The wind shear angle is given by α.

4.2.1 Theoretical influence of wind shear

Under the influence of wind shear (and if we assume $C_n^2(h)_0$ is measured exactly), CAW will be unable to perfectly fit to $M_{\delta t}$ as it is relying on the conservation of turbulence strength. However, it is possible to theoretically estimate the influence of wind shear on CAW wind velocity profiling. If CAW is searching for a least-squares fit to 2 dispersed layers, the minimum will be found at a point along the shortest distance vector. In Figure 4.3, this

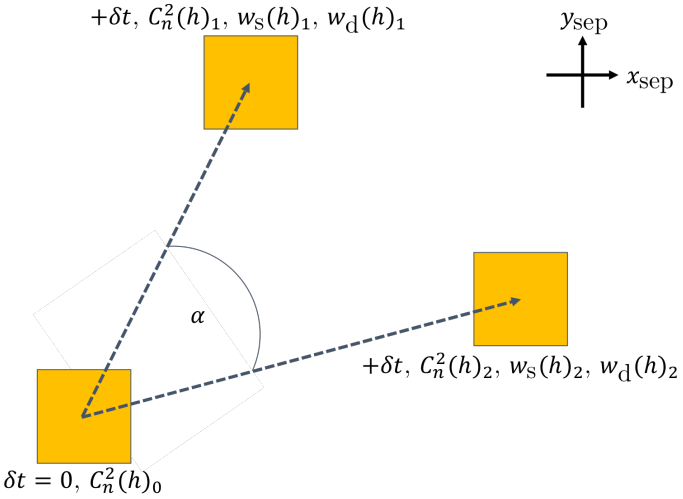

Figure 4.3: The yellow square in the bottom left illustrates a turbulent layer measurement within M_0 (similar to the peaks shown in Figure 2.15b, for example). After a positive temporal offset, $+\delta t$, has been applied, the turbulent layer is shown to in fact be made of two independent layers. These two layers have different strengths and velocities. The yellow squares corresponding to these layers (top middle and middle right) are an illustration of how they have been displaced after a positive temporal offset, i.e. how they could appear in $M_{\delta t}$.

is the vector between $C_n^2(h)_1$ and $C_n^2(h)_2$. If $C_n^2(h)_1 = C_n^2(h)_2$ then the least-squares minimum will be found when CAW analytically fits $C_n^2(h)_0$ to the middle of the vector that connects $C_n^2(h)_1$ and $C_n^2(h)_2$. For 2-layer wind shear, the theoretical output for the wind speed and wind direction measurement are given by $e_s(h)$ and $e_d(h)$, respectively, where

$$e_s(h) = \left[w_s(h)_1^2(p-1)^2 + w_s(h)_2^2 p^2 + 2p w_s(h)_1 w_s(h)_2 \cos\alpha(1-p)\right]^{1/2}, \tag{4.2}$$

$$e_d(h) = \sin^{-1}\left(\frac{p \sin\alpha w_s(h)_2}{e_s(h)}\right), \tag{4.3}$$

and

$$p = \frac{C_n^2(h)_2}{C_n^2(h)_1 + C_n^2(h)_2}. \tag{4.4}$$

Equations 4.2 and 4.3 make the approximation that both layers are at the same altitude. Wind shear can involve more than 2 layers. This complicates the theoretical output model outlined above however, the underlying principle remains the same. For example, 3-layer wind shear would form a triangle within $M_{\delta t}$, and CAW would find the least-squares fit to be at the centre of gravity of this triangle. Therefore, if there are more than 2 wind shear layers, the system is stabilised by the turbulent layers being more evenly weighted. By studying 2-layer wind shear, we can understand the extent to which wind shear can reduce the accuracy of CAW.

When $p = 0.5$, the CAW measurement will be split between the 2 wind shear layers, i.e. it will not be favourable tethered to a specific turbulent layer. To demonstrate the adverse

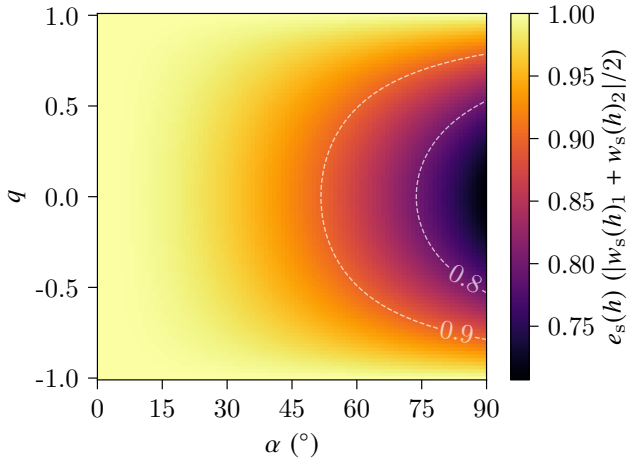

Figure 4.4: The theoretical wind speed measurement from CAW, $e_s(h)$, when it is fitting a single layer under 2-layer wind shear. The wind shear angle, α (see Figure 4.3), is plotted against wind speed contrast, q, where $q = (w_s(h)_1 - w_s(h)_2)/(w_s(h)_1 + w_s(h)_2)$. The 2 wind shear layers have equal strengths. $e_s(h)$ is in units of the mean wind speed because measuring the mean would be the optimal result. The results show that up to roughly $\alpha = 50°$, CAW has a wind speed measurement accuracy of 90 %.

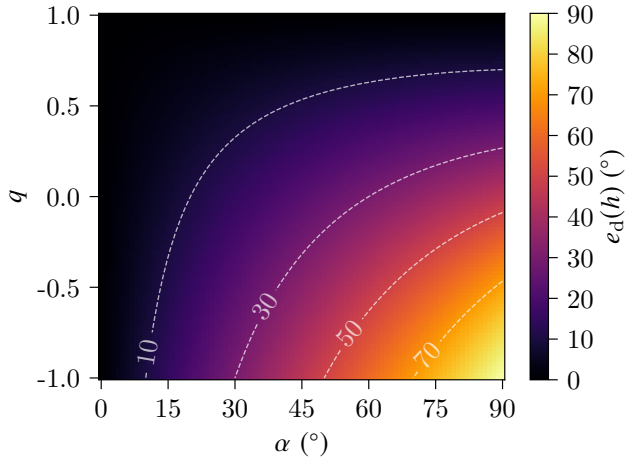

Figure 4.5: The theoretical wind direction measurement from CAW, $e_d(h)$, when it is fitting a single layer under 2-layer wind shear. The wind shear angle, α (see Figure 4.3), is plotted against wind speed contrast, q, where $q = (w_s(h)_1 - w_s(h)_2)/(w_s(h)_1 + w_s(h)_2)$. The 2 wind shear layers have equal strengths. The results show that CAW wind direction profiling is sensitive to wind shear. If the two layers are moving at equal speeds then $e_d(h) = \alpha/2$.

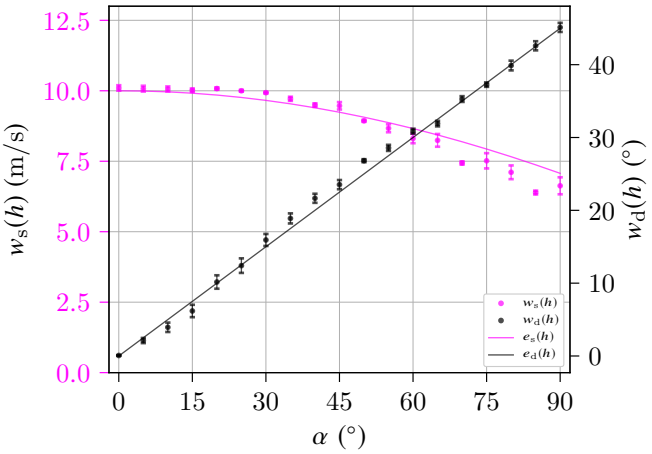

Figure 4.6: Measured CAW wind speed and direction at different wind shear angles, α. $C_n^2(h)_1 = C_n^2(h)_2$, $w_s(h)_1 = w_s(h)_2 = 10\,\mathrm{m/s}$ and $w_d(h)_1 = 0°$. The theoretical predictions are shown alongside.

effects of this scenario to wind speed profiling, Figure 4.4 plots the wind shear angle, α (see Figure 4.3), against the wind speed contrast, q, where $q = (w_s(h)_1 - w_s(h)_2)/(w_s(h)_1 + w_s(h)_2)$. These variables are shown as a function of the theoretical CAW wind speed measurement, $e_s(h)$. Figure 4.4 shows that CAW wind speed profiling is robust to wind shear. An optimised system would measure the wind speed to be the mean of the 2 wind shear layers. Across all wind shear speeds and up to a wind shear angle of approximately 50°, CAW is expected to achieve 90 % wind speed accuracy. The corresponding plot for wind direction profiling is shown in Figure 4.5. The CAW wind direction measurement is clearly sensitive to wind shear. If $w_s(h)_1 = w_s(h)_2$ and $C_n^2(h)_1 = C_n^2(h)_2$, $e_d(h) = \alpha/2$.

To test the theoretical model, 2-layer wind shear was simulated for a 2-NGS CANARY system in Soapy. The simulation was parameterised by the values listed in Table 2.2. Two layers were simulated at $h = 0\,\mathrm{km}$ with $C_n^2(h)_1 = C_n^2(h)_2$ and $w_s(h)_1 = w_s(h)_2$. Integrated r_0 was 0.1 m, $w_s(h)_1 = 10\,\mathrm{m/s}$ and $w_d(h)_1 = 0°$. The 2-layer simulation was repeated over wind shear angles ranging from 0 to 90. For each α value, the simulation was repeated 10 times so that the mean along with its standard error could be calculated. Ground-layer CAW (CAW 3) was performed on each simulation (the same process that was used to calculate Figure 4.2b). The measured wind speeds and directions are shown in Figure 4.6. The theoretical output measurements from CAW are in agreement.

4.2.2 Expected wind shear on-sky

In Section 5.1.2 we study on-sky data from CANARY. Our wind velocity profiling results are compared to profiles from the European Centre for Medium-Range Weather Forecasts (ECMWF). In this section we use the ECMWF data from Section 5.1.2 to demonstrate the range of possible wind shear values on-sky.

When analysing both simulated and on-sky CANARY data, we fit 7 evenly-spaced layers between 0 and 24 km. The fitted ground-layer during CAW 3 therefore has the integrated turbulence strength from 0 to 2 km (see Figure 3.10). Using the ECMWF wind velocities from Section 5.1.2, we can calculate the values of q and α between 0 to 2 km. A 2D histogram of the results is shown in Figure 4.7a. In total, 27 ECMWF wind velocity profiles have been analysed. The corresponding plots for the layers fitted at 10 and 20 km are shown in Figure 4.7b and Figure 4.7c, respectively. So that they can be easily compared to Figures 4.4 and 4.5, the plots in Figure 4.7 are shown for $q = -1$ to 1 and $\alpha = 0$ to 90°.

For the layer fitted at the ground, Figure 4.7a shows that the maximum value of the wind shear angle, α, is roughly 50°. The most detrimental scenario is when $p = 0.5$ (see Section 4.2.1) and by studying Figure 4.4, this can result in a 10% error in the wind speed measurement. If the layers are travelling at equal speeds, Figure 4.5 shows that the wind direction measurement would have an approximate error of 30°. The layer fitted at 10 km has a similar spread of values (see Figure 4.7b) however, its maximum value of α is approximately 75°. For the layer fitted at 20 km, there is a wider range of values in both q and α.

It should be noted that a large fraction of the data points do not indicate significant wind shear. The influence of the outliers is also entirely dependent on their turbulence strength. From Figure 4.7 it can be concluded that at higher altitudes there is a greater likelihood for significant wind shear. The best way to reduce the influence of wind shear is by fitting more turbulent layers that therefore have a smaller altitude range. Assuming that the GS asterism is fixed, this requires larger SHWFS sub-aperture dimensions, i.e. as AOF and ELT-scale instruments have more spatial information, they can fit more layers and will therefore be less susceptible to wind shear.

4.3 Validating wind velocity measurements

It is unrealistic to assume that the analytical model will perfectly match SHWFS cross-covariance measurements during CAW. There are a number of reasons for this, e.g. the measured turbulence not being fully developed and therefore having non-Kolmogorov statistics (see Section 3.2). As the LMA is performing a 2D least-squares fit, there must be a system in place to validate wind velocity profiling detections. The presented solution runs CAW twice: once at the studied temporal offset, ω/f, and once at $(\omega - 1)/f$. The wind velocity measurements from ω/f and $(\omega - 1)/f$ are given the superscript m and v, respectively, i.e. the wind speed measurement $w_{\mathrm{s}}^{\mathrm{m}}(h^{\mathrm{m}})$ is validated by $w_{\mathrm{s}}^{\mathrm{v}}(h^{\mathrm{v}})$. A wind velocity measurement is deemed false if any of the following conditions are satisfied:

1. The absolute difference between the wind speed measurements is greater than 5 m/s, i.e. $|w_{\mathrm{s}}^{\mathrm{m}}(h^{\mathrm{m}}) - w_{\mathrm{s}}^{\mathrm{v}}(h^{\mathrm{v}})| > 5\,\mathrm{m/s}$.

2. The absolute difference between the wind direction measurements is greater than 30°, i.e. $|w_{\mathrm{d}}^{\mathrm{m}}(h^{\mathrm{m}}) - w_{\mathrm{d}}^{\mathrm{v}}(h^{\mathrm{v}})| > 30°$

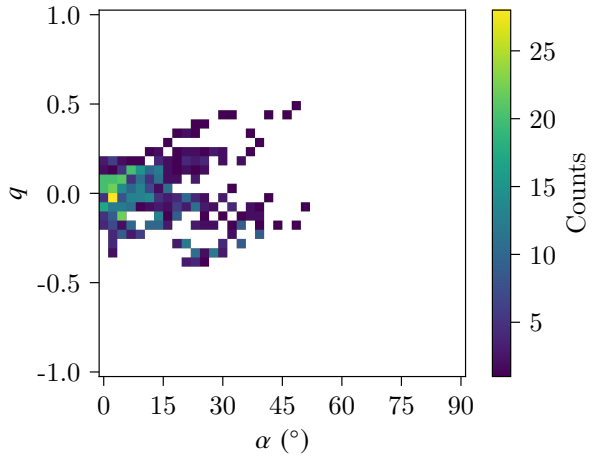

(a) Between 0 and 2 km.

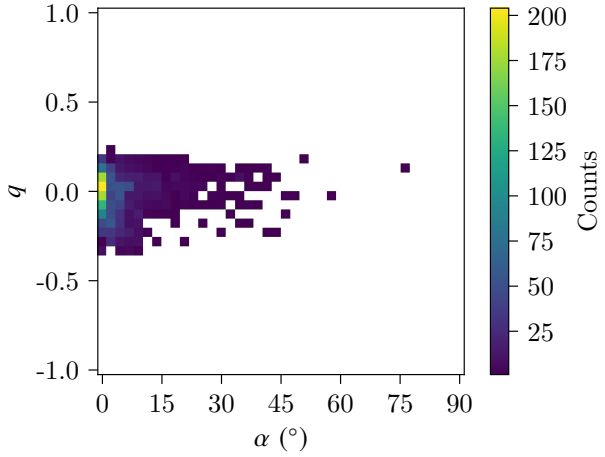

(b) Between 8 and 12 km.

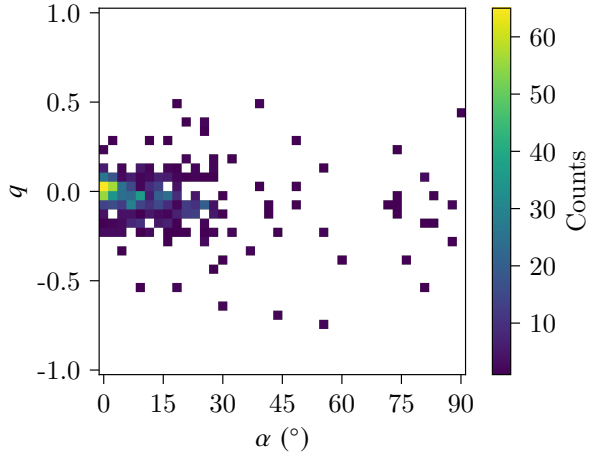

(c) Between 18 and 22 km.

Figure 4.7: Possible values for the wind shear angle, α, and the wind speed contrast, q. 27 ECMWF wind velocity profiles from La Palma were used to calculate α and q.

3. The absolute difference between the altitude measurements is greater than $h_{\max}/10$, i.e. $|h^{\mathrm{m}} - h^{\mathrm{v}}| > h_{\max}/10$

4. Either altitude measurement is above the maximum observable altitude, i.e. $h^{\mathrm{m}} > h_{\max}$ or $h^{\mathrm{v}} > h_{\max}$.

5. Either wind speed measurement is greater than 100 m/s, i.e. $w_{\mathrm{s}}^{\mathrm{m}}(h^{\mathrm{m}}) > 100\,\mathrm{m/s}$ or $w_{\mathrm{s}}^{\mathrm{v}}(h^{\mathrm{v}}) > 100\,\mathrm{m/s}$.

6. The location of the turbulent layer is not within $M_{\delta t}$.

The values chosen to satisfy 1 to 4 were selected through testing CAW in simulation. Conditon 5 is included as 100 m/s is the upper limit of the expected atmospheric wind speed. For the values listed, an incorrect detection would always satisfy multiple conditions. It should also be noted that this validation technique is independent of AO system parameters, e.g. the number of SHWFS sub-apertures.

4.4 Wind velocity profiling from simulated adaptive optics telemetry

Open-loop SHWFS centroids were simulated for a 4-NGS CANARY configuration in Soapy. Each SHWFS had 7×7 sub-apertures. The median results within the European Southern Observatory (ESO) documentation (Kolb et al., 2015) were used to parameterise the simulated 35-layer optical turbulence and wind speed profile. The 35-layer ESO profile does not include wind direction and so the simulated wind direction profile followed an example radiosonde measurement from Hirsch et al., 2011. The outer scale of every simulated layer was 25 m and the integrated turbulence strength was $r_0 = 0.1\,\mathrm{m}$ at $\lambda = 0.5\,\mu\mathrm{m}$. The 4-NGS system had a square layout with $h_{\max} = 24\,\mathrm{km}$. On-sky NGS observations rarely adhere to having such a well-ordered asterism. However, the simulated square layout is an appropriate approximation (see Section 5.2). The values in the Soapy configuration file were the same as those listed in Table 2.2. The simulation was repeated 10 times so that mean CAW results along with their standard error could be calculated. The CAW fitting procedure was performed using the simulated SHWFS centroids. The six 7×7 SHWFS combinations were fitted to simultaneously using 7 evenly-spaced layers from 0 to 24 km.

The optical turbulence profiling results from CAW 1 are shown in Figure 4.8a. The wind velocity results are shown in Figure 4.8b and Figure 4.8c. For reasons discussed in Section 5.1.2, CAW was operated with $\omega = 8$, where ω is the number of SHWFS frames that have been offset. The wind velocity profile was fitted for all layers above the noise-floor. Out of the 10 simulations, the layers fitted at 20 and 24 km were validated (see Section 4.3) 6 and 0 times, respectively. This is why only 6 measured layers are shown for the NGS results in Figure 4.8b and Figure 4.8c. This is mainly attributed to the fact that the layers that failed to be validated are the weakest and therefore carry the least weight during CAW 2. They are also positioned towards the edge of the covariance map

Table 4.1: Comparing NGS and LGS CAW results to the simulated 35-layer profile. The CAW results were obtained by fitting to spatio-temporal covariance maps with $\omega = 8$. F_{md} is the mean logarithmic deviation between the measured and the reference turbulence profile (see Section 3.4). The measured turbulence profile is equal to the reference turbulence profile when $F_{\mathrm{md}} = 0$.

	F_{md}	R_{w}	A_{rms} (m/s)	B (m/s)
NGS	0.11 ± 0.02	0.80 ± 0.02	2.2 ± 0.3	0.2 ± 0.2
LGS	0.06 ± 0.01	0.75 ± 0.04	2.0 ± 0.1	1.1 ± 0.2

where the Signal-to-Noise Ratio (SNR) is lowest. The number of validated wind velocity profile candidates divided by the total number of candidates is denoted R_{w}. The layers that have been validated closely follow the trend of the simulated wind velocity profile. The relatively large errors at 21 km are thought to originate from CAW fitting near the maximum altitude of NGS sub-aperture optical path intersection, $h_{\max}$.

The NGS study was repeated for sodium LGSs that had an apparent magnitude of 8 and were focussed at an altitude of 90 km. The SHWFSs were simulated to measure a monochromatic wavelength of 589 nm. All of the other simulated parameters were the same as those listed in Table 2.2. Due to the cone effect, the maximum altitude of sub-aperture optical path intersection was roughly 19 km. Therefore, when repeating the CAW 1 measurement on the simulated dataset, a layer was not fitted at 24 km. The LGS optical turbulence profiling results are shown in Figure 4.8a. As the layer fitted at 20 km has its peak value above the maximum altitude of sub-aperture optical path intersection, it is not included in LGS F_{md} analysis. The 6 layers fitted in CAW 1 were fitted during CAW 2 and CAW 3. Out of the 10 simulations, the layers fitted at 16 and 20 km were validated (see Section 4.3) 6 and 0 times, respectively. The mean of each validated layer is shown alongside the NGS results in Figure 4.8b and Figure 4.8c.

We use the mean logarithmic deviation, F_{md}, from Equation 3.2 (see Section 3.4) to quantify the optical turbulence profiling results. The root mean square deviation, A_{rms}, and bias, B, are used to quantify the accuracy of $w_{\mathrm{s}}^{\mathrm{m}}(h^{\mathrm{m}})$, where

$$A_{\mathrm{rms}} = \sqrt{\frac{1}{R_{\mathrm{w}} N_{\mathrm{L}}} \sum_{i=1}^{R_{\mathrm{w}} N_{\mathrm{L}}} \left(w_{\mathrm{s}}^{\mathrm{m}}(h_i^{\mathrm{m}}) - w_{\mathrm{s}}^{\mathrm{r}}(h_i^{\mathrm{r}}) \right)^2}, \tag{4.5}$$

$$B = \frac{1}{R_{\mathrm{w}} N_{\mathrm{L}}} \sum_{i=1}^{R_{\mathrm{w}} N_{\mathrm{L}}} \left(w_{\mathrm{s}}^{\mathrm{m}}(h_i^{\mathrm{m}}) - w_{\mathrm{s}}^{\mathrm{r}}(h_i^{\mathrm{r}}) \right). \tag{4.6}$$

In Equations 4.5 and 4.6, the superscript r denotes the reference altitude and wind speed, i.e. $w_{\mathrm{s}}^{\mathrm{r}}(h^{\mathrm{r}})$ is the reference wind speed profile. i denotes the layer number and each value of h_i^{r} is the nearest neighbour to h_i^{m}. As $w_{\mathrm{d}}^{\mathrm{m}}(h^{\mathrm{m}})$ is given in polar coordinates, it is not possible to quantify the accuracy of $w_{\mathrm{d}}^{\mathrm{m}}(h^{\mathrm{m}})$ for all wind directions. The CAW results from the NGS and LGS simulated datasets are summarised in Table 4.1. LGS F_{md} is less than NGS F_{md}. However, NGS $F_{\mathrm{md}} = 0.03$ if only the layers from 0 to 16 km are considered.

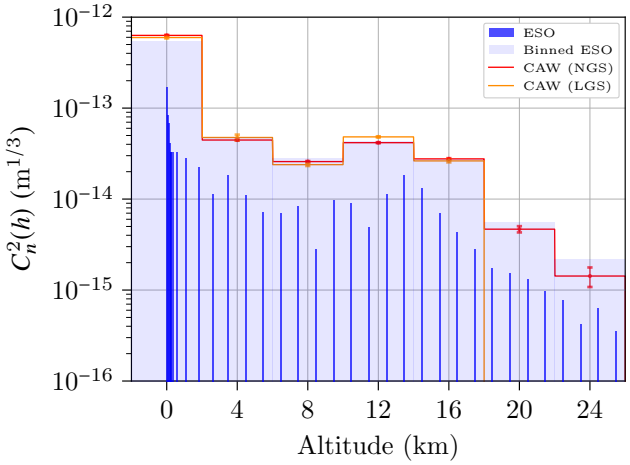

(a) Optical turbulence profiling results from CAW 1.

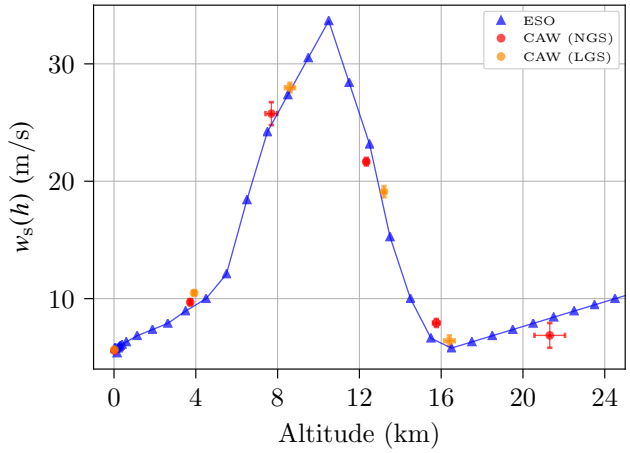

(b) Wind speed profiling results from CAW 2 and CAW 3.

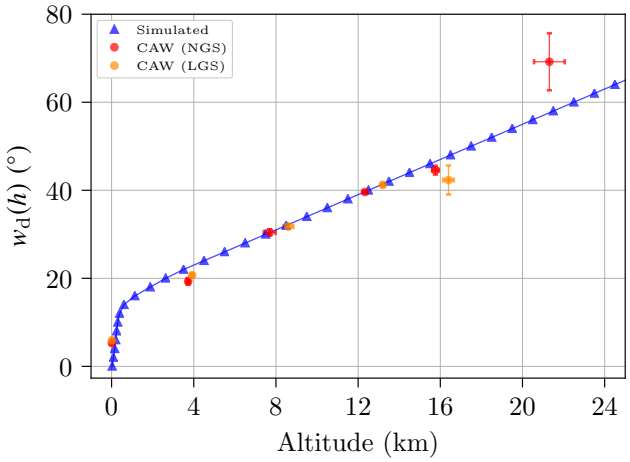

(c) Wind direction profiling results from CAW 2 and CAW 3.

Figure 4.8: CAW results from fitting to simulated NGS and LGS CANARY centroid cross-covariance arrays. The simulated 35-layer profile is shown alongside.

4.5 Summary

We have presented a novel technique for automated wind velocity profiling from AO telemetry. This enables AO system control techniques that significantly improve image resolution. The introduced wind velocity profiling technique is referred to as CAW and it relies on accurate AO parameter estimation. We used the parameter estimation technique recommended in Chapter 3.

We addressed the problem of wind shear by developing a theoretical model for how it influences the measurements from CAW. Using on-sky forecasts from the ECMWF, it was shown that significant wind shear is more likely to occur at higher altitudes. CAW was then tested using simulated data from CANARY. The simulations were parameterised with the 35-layer ESO profile. For the NGS simulations, the wind speed bias and root mean square deviation were measured to be $B = 0.2 \pm 0.2\,\mathrm{m/s}$ and $A_{\mathrm{rms}} = 2.2 \pm 0.3\,\mathrm{m/s}$, respectively. CAW was also shown to be equally applicable to LGS analysis.

— 5 —

On-sky turbulence and wind velocity profiling from adaptive optics telemetry

We have developed detailed algorithms for turbulence and wind velocity profiling. These are referred to as CovAriance Parametrisation of optical Turbulence and SHWFS misalignments (CAPT; see Chapter 3; Laidlaw et al., 2018) and CovAriance parametrisation of Wind velocity (CAW; see Chapter 4; Laidlaw et al., 2019). In this chapter we use these algorithms to analyse on-sky data.

In Section 5.1 we study on-sky data from CANARY, the Adaptive Optics (AO) demonstrator for Extremely Large Telescope-scale (ELT-scale) technologies on the 4.2 m William Herschel Telescope (WHT; see Section 2.4.1), La Palma. The Multi-Object Adaptive Optics (MOAO; see Section 2.2.6.2) capabilities of CANARY have been previously published (Gendron et al., 2011; Vidal et al., 2014; Martin et al., 2017). In Section 5.1.1 we investigate how to optimise the accuracy of the CAPT turbulence profiling procedure. The optimal temporal offset for CAW wind velocity profiling is investigated in Section 5.1.2. Reference turbulence and wind velocity profiles were measured by the Stereo-SCIDAR instrument (see Section 2.3.2) that was being operated on the 2.5 m Isaac Newton Telescope (INT), La Palma. The measured wind velocity profiles are also compared against results from the European Centre for Medium-Range Weather Forecasts (ECMWF).

In Section 5.2 we apply CAPT and CAW to on-sky data from the Adaptive Optics Facility (AOF). The AOF is on the 8.2 m Yepun telescope at the Very Large Telescope (VLT; see Section 2.4.2), Paranal. The AOF data was recorded by Ground Atmospheric Layer Adaptive Corrector for Spectroscopic Imaging (GALACSI; Stuik et al., 2006), a Ground-Layer Adaptive Optics (GLAO; see Section 2.2.6.1) module for the Multi-Unit Spectroscopic Explorer (MUSE; McDermid et al., 2008). We present AOF GALACSI time sequences that show detailed examples of turbulence and wind velocity profiles at the VLT. In Section 5.2.2, the wind velocity profiles from AOF GALACSI are compared against results from the ECMWF.

5.1 CANARY

During each observation, CANARY observed four Natural Guide Stars (NGSs). Each NGS was monitored by an independent 7×7 Shack–Hartmann Wavefront Sensor (SHWFS).

Within every dataset each SHWFS recorded 10,000 open-loop centroid measurements at a frame rate of approximately 150 Hz.

The results from CANARY are compared to contemporaneous measurements from the Stereo-SCIDAR instrument. Stereo-SCIDAR was being operated roughly 400 m east of the WHT. The time interval between a measurement from Stereo-SCIDAR and CANARY centroid-data retrieval was limited to 20 minutes. It was assumed that both the turbulence and wind velocity profile would not drastically alter within this timescale (Jia et al., 2018). In total there were 27 useful datasets. These observations were made in July and October of 2014 across 4 and 3 nights, respectively. Although all of the datasets could be used to compare optical turbulence profile measurements, Stereo-SCIDAR post-processing had filtered out the wind velocity measurements from 4 of them, i.e. only 23 wind velocity profiles could be compared between CANARY and Stereo-SCIDAR. To substantiate CAW wind velocity profiling, we compare all 27 profiles to the ECMWF.

5.1.1 Turbulence profiling

Using the CAPT fitting algorithm, covariance matrix and map Region of Interest (ROI) optical turbulence profiling was performed on the CANARY dataset. Seven evenly-spaced layers were fitted from 0 to 24 km. The six SHWFS combinations were fitted to simultaneously. For each observation, no layer above the maximum observable altitude, $h_{\max}$, was fitted. Data from Stereo-SCIDAR was assumed to be a high-resolution measure of the reference optical turbulence profile and therefore – as with the simulated profile in Section 3.6 – its measurements were binned to the fitted altitudes to give $C_n^2(h^{\mathrm{m}})^{\mathrm{r}}$. The noise floor for $C_n^2(h^{\mathrm{m}})^{\mathrm{r}}dh$ was set at $10^{-16}\,\mathrm{m}^{1/3}$. To be included in the analysis of F_{md}, the fitted layer was required to be centred at or below $h_{\max}$. It had to also not extend past the maximum altitude bin of Stereo-SCIDAR. All remaining measurements were used to calculate the mean value of F_{md} along with its standard error (see Section 3.4).

The results in Table 5.1 quantify the relation between Stereo-SCIDAR and CANARY AO telemetry optical turbulence profiling. These results show the mean logarithmic deviation between the measured and reference turbulence profiles, F_{md}, after 1 and 15 CAPT iterations (see Section 3.5). It is clear from Table 5.1 that fitting SHWFS misalignments has not noticeably improved the system. For covariance matrix fitting, the absolute mean was calculated from the measured SHWFS misalignments. The results are shown in Table 5.2. The corresponding results for covariance map ROI fitting are shown in Table 5.3. The standard error on each SHWFS misalignment measurement was negligible. From Tables 5.2 and 5.3, it can be concluded that there is no change in F_{md} because the mean rotation and shift misalignments are at most 2.11° and $0.03\,D$, respectively. However, it is important to note that similar misregistrations would significantly impact an ELT-scale AO system (see Figures 3.6 to 3.8). Covariance matrix fitting found xx and yy vibration artefacts to account for an average of 0.011 ± 0.001 and $0.011 \pm 0.001\,\mathrm{arcsec}^2$ per observation. The covariance map ROI measured these vibration artefacts to be 0.012 ± 0.001 and $0.011 \pm 0.001\,\mathrm{arcsec}^2$.

Table 5.1: Covariance matrix and map ROI optical turbulence profiling results from fitting to on-sky CANARY cross-covariance arrays. F_{md} is the mean logarithmic deviation between the measured and the reference turbulence profile (see Section 3.4). The measured turbulence profile is equal to the reference turbulence profile when $F_{\mathrm{md}} = 0$.

	F_{md}	
	1 CAPT Iteration	15 CAPT Iterations
Matrix	0.46 ± 0.04	0.46 ± 0.04
Map ROI	0.38 ± 0.04	0.38 ± 0.04

Table 5.2: Mean absolute SHWFS misalignment results from using covariance matrix CAPT to fit to on-sky CANARY data. SHWFS 4 is the zeroth point for all SHWFS shift misalignments.

	Shift offset in x (D)	Shift offset in y (D)	Rotational offset (°)
SHWFS 1	0.01	0.02	1.33
SHWFS 2	0.02	0.00	1.14
SHWFS 3	0.01	0.00	1.08
SHWFS 4	0.00	0.00	1.06

Table 5.3: Mean absolute SHWFS misalignment results from using covariance map ROI CAPT to fit to on-sky CANARY data. SHWFS 4 is the zeroth point for all SHWFS shift misalignments.

	Shift offset in x (D)	Shift offset in y (D)	Rotational offset (°)
SHWFS 1	0.02	0.02	1.80
SHWFS 2	0.03	0.01	2.11
SHWFS 3	0.01	0.01	1.27
SHWFS 4	0.00	0.00	1.56

If Stereo-SCIDAR measurements are assumed to be the reference turbulence profiles, CAPT is able to more accurately measure the turbulence profile when it is twinned with covariance map ROI data analysis. However, the associated uncertainties prevent this from being a definitive conclusion. The on-sky results are not as accurate as those from Section 3.6. This is attributed to a number of additional factors: the INT and WHT will both have unique dome and local environmental seeing conditions; the telescopes are not observing the same direction; the on-sky NGS asterisms have a range of position angles, separations and apparent magnitude values; the data retrieved for profiling has not been recorded at the exact same instant.

The investigation into the optimal size of the covariance map ROI (see Section 3.6) was repeated with the on-sky CANARY data. The results are shown in Figure 5.1b. Figure 3.12 has been repeated in Figure 5.1a so that it can be easily compared to Figure 5.1b. If binned Stereo-SCIDAR is considered to be the reference turbulence profile, both simulation and on-sky results agree that the system does not benefit from including baselines at an ROI width greater than $W = 1$. To reiterate the discussion in Section 3.6: future investigations should proceed with caution as ELT outer scale fitting might require $W > 1$. The slight discrepancies between Figures 5.1a and 5.1b can be attributed to the reasons previously listed. The lowest and highest F_{md} values within Figure 5.1b are 0.38 ± 0.04 and 0.44 ± 0.04,

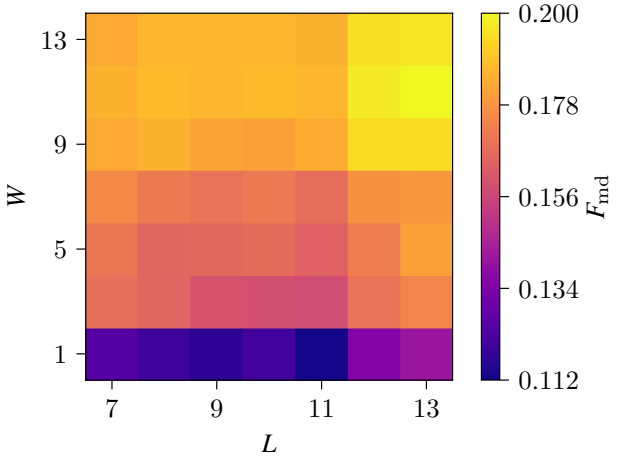

(a) CAPT analysis of simulated data from Section 3.6. The optical turbulence profile reference is the binned form of the 35-layer European Southern Observatory (ESO) profile.

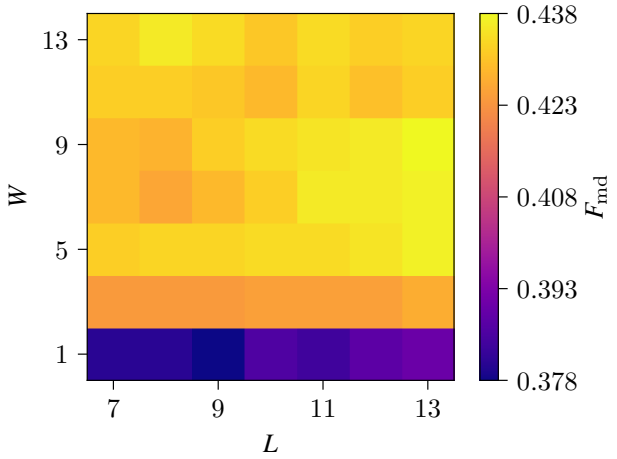

(b) CAPT analysis of on-sky data. The optical turbulence profile reference is the binned form of the corresponding Stereo-SCIDAR observation.

Figure 5.1: Mean deviation, F_{md}, shown as a function of covariance map ROI length, L, and width, W. The results are from CAPT analysis of simulated and on-sky NGS CANARY data.

respectively, and can be found at $L, W = (9, 1)$ and $L, W = (13, 9)$.

Figure 5.2a shows the log-log plot between Stereo-SCIDAR and CANARY covariance matrix optical turbulence profiling. Each data point shows an individual turbulence layer strength that has been measured by CAPT and Stereo-SCIDAR (after the Stereo-SCIDAR measurements have been binned across the corresponding altitude range). The data point colours highlight the altitudes at which the turbulence strengths were measured. Turbulent layers that are at the noise floor are not shown in the plot but are included in the calculation of F_{md}. The corresponding plot for the covariance map ROI is shown in Figure 5.2b.

The Stereo-SCIDAR observations have a median integrated r_0 of 0.15 m. Covariance matrix

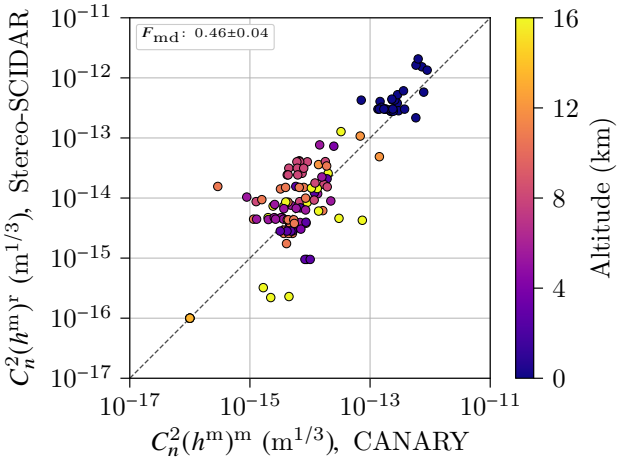

(a) Results from covariance matrix fitting.

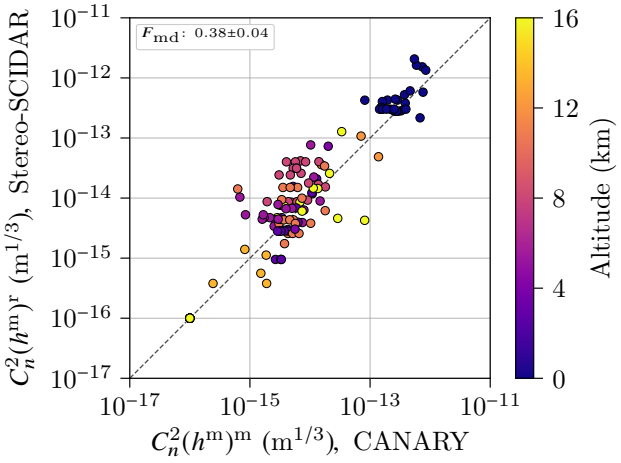

(b) Results from covariance map ROI fitting.

Figure 5.2: Log-log plots of binned Stereo-SCIDAR and CANARY optical turbulence profiling. The black broken lines plot where the measured and reference turbulence profiles are equal. The individual layer strengths from CAPT are compared to Stereo-SCIDAR measurements that have been binned across each corresponding altitude range. The colour of each data point highlights the altitude at which the turbulence strength was measured.

Table 5.4: Notation used frequently throughout Section 5.1.2.

Ω	The highest number of SHWFS frames that have been offset
$M_{\delta t}$	Temporally offset covariance map array
Δt	Maximum temporal offset
N_o	The number of temporally offset covariance map arrays studied at one time
m_o	Offset order (the range of values from 1 to N_o)
F_md	Mean logarithmic deviation
R_w	Fraction of validated wind velocity measurements
B	Wind speed bias
A_rms	Wind speed root mean square deviation

and map ROI fitting measure median integrated r_0 to be 0.18 and 0.17 m, respectively. At 0 km there is an expected bias because Stereo-SCIDAR and CANARY are operating out of different telescope domes that are separated by roughly 400 m.

5.1.2 Wind velocity profiling

Towards the end of Section 4.1 we discussed the possibility of our wind velocity profiling algorithm, CAW, fitting multiple temporal offsets at once. For example, temporally offset covariance map arrays $M_{3/f}$, $M_{6/f}$ and $M_{9/f}$ can be summed together, giving the location of each turbulent layer at 3 separate instances. CAW can then fit the expected value of each turbulent layer 3 times. For frozen-flow and zero wind shear, each turbulent layer should track a linear path. The number of temporal offsets studied at one time is given by N_o. The maximum temporal offset within the N_o dataset is denoted Δt. The highest number of frames that are offset is Ω. Therefore, the example outlined above has $N_\mathrm{o} = 3$, $\Delta t = 9/f$ and $\Omega = 9$. Its wind velocity measurements are verified (see Section 4.3) by using CAW to fit to temporally offset covariance maps that have their number of offset frames equal to $(\Omega - N_\mathrm{o})m_\mathrm{o}/N_\mathrm{o}$, where m_o is the offset order, i.e. for $N_\mathrm{o} = 3$, $m_\mathrm{o} = 1, 2, 3$. This implies that, for the example above, the covariance map array used to verify the CAW measurements would be the summation of $M_{2/f}$, $M_{4/f}$ and $M_{6/f}$. The system is defined such that $\Omega > N_\mathrm{o}$ and $\Omega/m_\mathrm{o} \in \mathbb{Z}$. To summarise our notation, the characters we use frequently throughout this section are defined in Table 5.4.

CAW 2 and 3 were performed on the CANARY dataset from Section 5.1.1. The CAW 1 measurements were the covariance map ROI results from Section 5.1.1. Wind velocity profiling was carried out for all combinations within $\Omega = 1$ to 30 and $N_\mathrm{o} = 1$ to 15. There are no data points at $\Omega = N_\mathrm{o}$ because these wind velocity measurements can not be validated, i.e. $(\Omega - N_\mathrm{o})m_\mathrm{o}/N_\mathrm{o} = 0$. The fraction of validated candidates, R_w, is shown in Figure 5.3. The corresponding results for the bias, B, between CAW and Stereo-SCIDAR, and CAW and the ECMWF, are shown in Figure 5.4. As in Section 4.4, the values for the reference wind velocity profiles came from nearest neighbour measurements. The results for the root mean square deviation, A_rms, are shown in Figure 5.5. In Figures 5.4 and 5.5, fitting $N_\mathrm{o} > 1$ tends to decrease the accuracy of CAW. This implies that the inclusion of multiple temporal offsets overcomplicates the fitting algorithm.

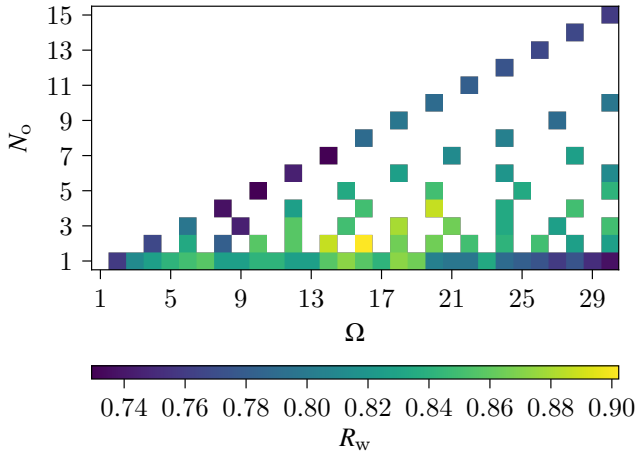

(a) R_w as a function of N_o and Ω.

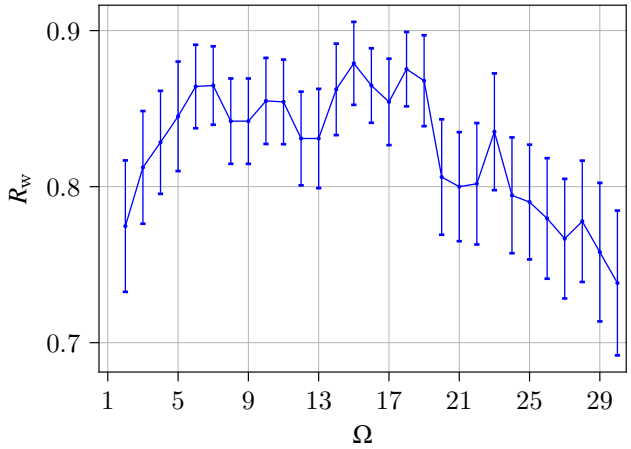

(b) R_w as a function of Ω at $N_o = 1$.

Figure 5.3: Fraction of CANARY wind velocity measurements that have been validated. In total, 27 datasets were analysed.

From Figures 5.3, 5.4 and 5.5, it can be seen that the optimal temporal offset is between $\Omega = 6$ and $\Omega = 16$. Within this range the highest fraction of CAW measurements are validated, and both B and A_{rms} are minimised. In Figure 5.5, the comparisons to Stereo-SCIDAR and the ECMWF have a common minimum when $\Omega = 8$ and $N_o = 1$. The $N_o = 1$ A_{rms} measurement is shown as a function of Ω in Figure 5.5c. The high A_{rms} result at small values of Ω implies that the temporal offset is not large enough for the wind velocity profile to be accurately measured, i.e. the turbulent layers have not been given enough time to disentangle from the Guide Star (GS) position angle, γ. At $\Omega > 8$, the most likely reason for the increase in A_{rms} is the fragmentation of the frozen-flow approximation, i.e. the turbulent phase has started to decay from its fixed state. The influence of wind shear will also increase with the size of the temporal offset. The stability of the frozen-flow approximation might vary with turbulence strength and wind speed however, $\Omega = 8$ is

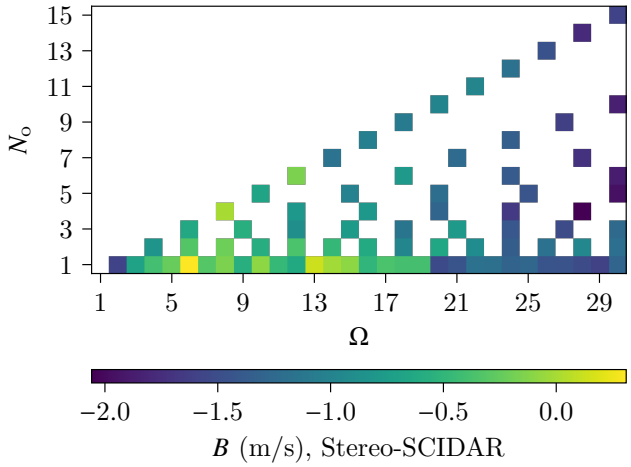

(a) Stereo-SCIDAR bias as a function of N_o and Ω.

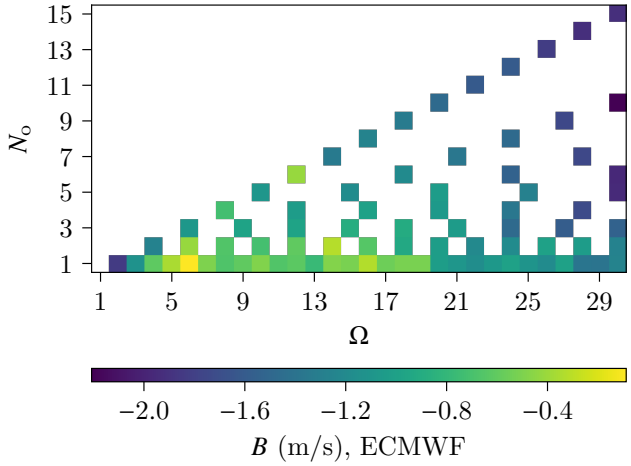

(b) ECMWF bias as a function of N_o and Ω.

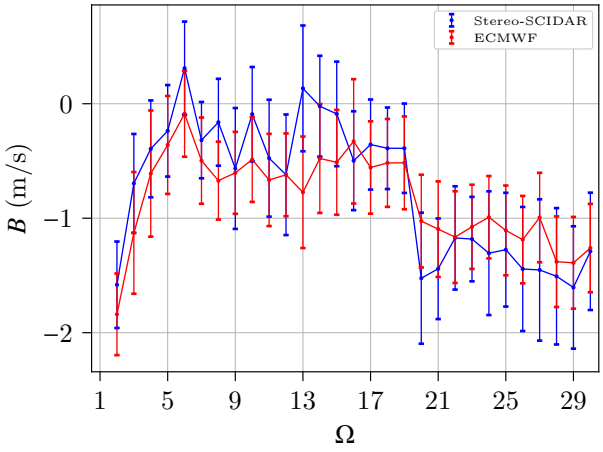

(c) Bias as a function of Ω at $N_o = 1$.

Figure 5.4: Average bias, B, between the measurements from CAW and the wind velocity profiling results from Stereo-SCIDAR and the ECMWF.

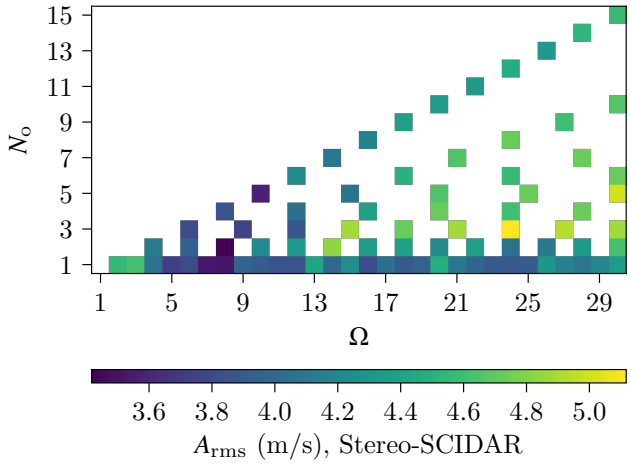

(a) Stereo-SCIDAR root mean square deviation as a function of N_o and Ω.

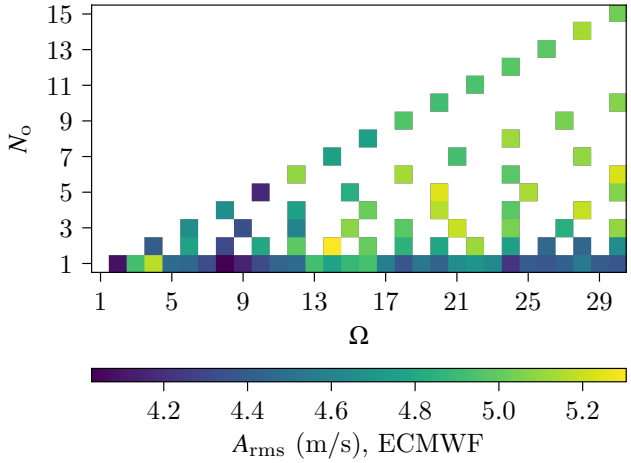

(b) ECMWF root mean square deviation as a function of N_o and Ω.

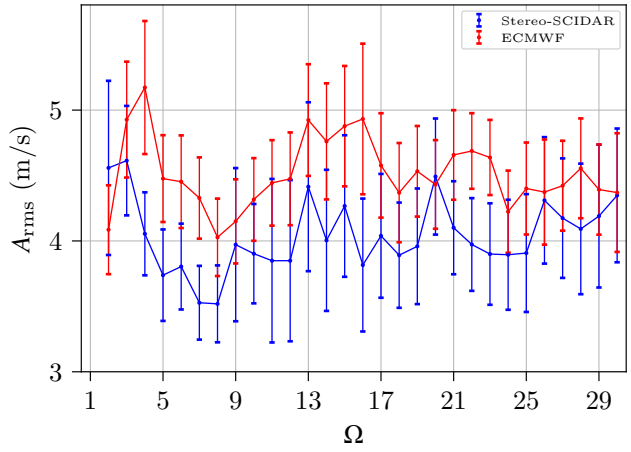

(c) Root mean square deviation as a function of Ω at $N_o = 1$.

Figure 5.5: Average root mean square deviation, A_{rms}, between the measurements from CAW and the wind velocity profiling results from Stereo-SCIDAR and the ECMWF.

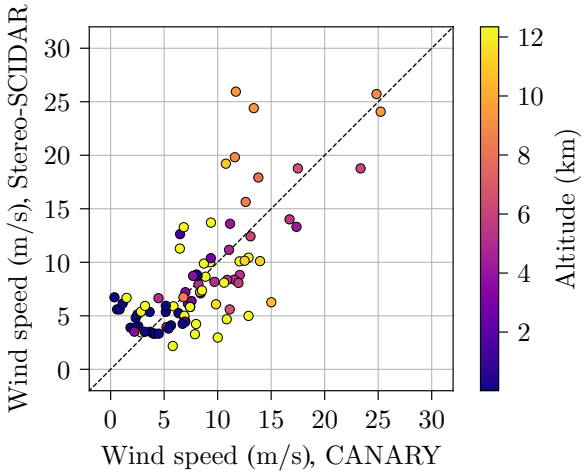

(a) The results between CAW and Stereo-SCIDAR.

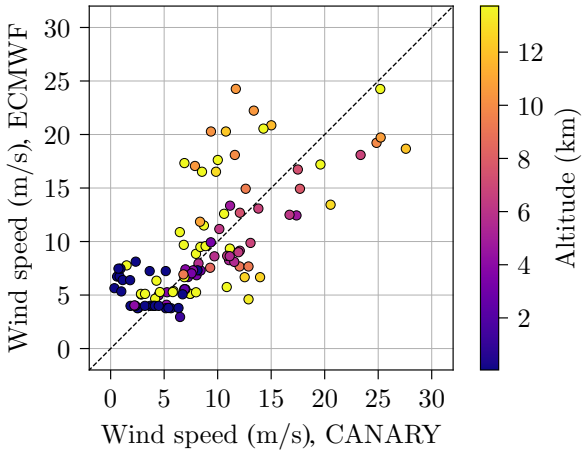

(b) The results between CAW and the ECMWF.

Figure 5.6: Stereo-SCIDAR and ECMWF versus the on-sky CANARY results from using CAW with $\Omega = 8$ and $N_o = 1$. Stereo-SCIDAR and ECMWF wind speeds are taken as the nearest neighbours to the measured altitudes. The black broken line plots equal wind speeds.

found to be the best-fit average across all altitudes. For CANARY, $\Omega = 8$ corresponds to roughly 0.05 s.

The wind speed scatter plots for CANARY against Stereo-SCIDAR and CANARY against ECMWF are shown in Figure 5.6a and 5.6b, respectively. The CANARY results are from CAW being operated with $N_o = 1$ and $\Omega = 8$. Only the validated candidates are shown. Discrepancies between the measurements in Figure 5.6a can be attributed to the reasons listed in Section 5.1.1. Wind shear will also be affecting the results in Figure 5.6. The results from Figure 5.6 are quantified in Table 5.5. A plot of Stereo-SCIDAR wind speeds versus the ECMWF is shown in Figure 5.7. These wind speeds correspond to the nearest

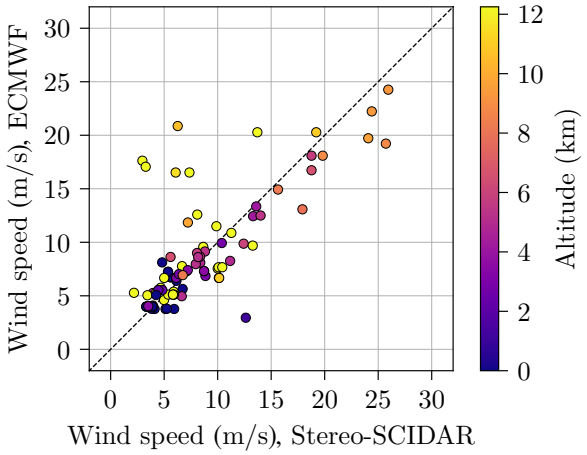

Figure 5.7: Stereo-SCIDAR wind speed measurements versus the ECMWF. The results correspond to the nearest neighbour wind speeds from Figure 5.6 The black broken line plots equal wind speeds.

Table 5.5: Stereo-SCIDAR and ECMWF compared to on-sky CANARY measurements from using CAW with $\Omega = 8$ and $N_o = 1$. Stereo-SCIDAR and ECMWF wind speeds are taken as the nearest neighbours to the measured altitudes.

	F_{md}	R_{w}	B (m/s)	A_{rms} (m/s)
Stereo-SCIDAR	0.38 ± 0.04	0.85 ± 0.03	-0.2 ± 0.4	3.5 ± 0.3
ECMWF	-	0.84 ± 0.03	-0.7 ± 0.3	4.0 ± 0.3

neighbour measurements in Figure 5.6.

5.1.3 Acknowledgements

The WHT and the INT are operated on the island of La Palma by the Isaac Newton Group in the Spanish Observatorio del Roque de los Muchachos of the Instituto de Astrofísica de Canarias. The work carried out at both of these telescopes was supported by the UK Science and Technology Funding Council (grant CG ST/P000541/1) and the European Commission (FP7 Infrastructures OPTICON grant 226604, 312430, and H2020 grant 730890).

5.2 The adaptive optics facility

The AOF is on the 8.2 m Yepun telescope at the VLT, Paranal. In this section we analyse data that was recorded at the AOF by GALACSI (Stuik et al., 2006), a GLAO module for MUSE (McDermid et al., 2008). GALACSI was being operated in closed-loop Wide Field Mode (WFM). Its 4-LGS square asterism is illustrated in Figure 5.8. Having a square asterism results in 6 SHWFS combinations. There are 2 altitude resolutions within these

Table 5.6: System parameters for the AOF GALACSI dataset.

Pupil diameter	8.2 m
Air mass	1.092
Monochromatic wavelength	589 nm
Frame rate	1 kHz
Number of frames	60,000
Distance to each LGS	95 km
SHWFS sub-apertures	40×40

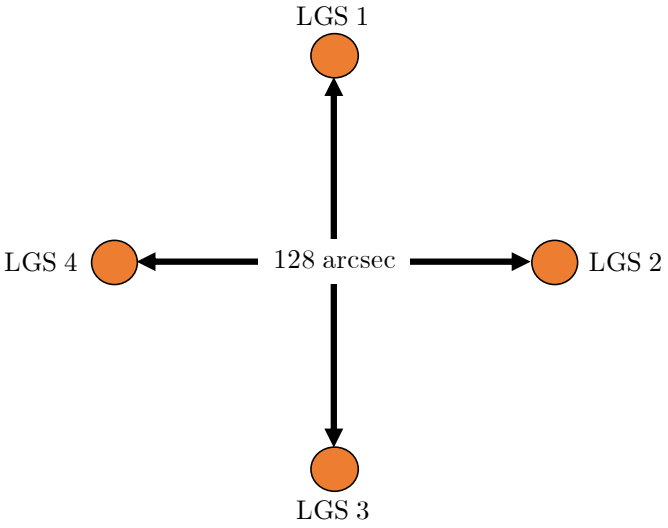

Figure 5.8: The 4-LGS asterism for the AOF GALACSI instrument in WFM.

6 combinations. The system parameters are listed in Table 5.6. Using Equation 2.23, the maximum observable altitude was 14 km.

5.2.1 Additional considerations

The AOF has four 40×40 SHWFSs that are each monitoring an independent LGS. Having a large number of sub-apertures means that, compared to CANARY, the AOF has more sub-aperture separation baselines. This increases the number of data points that both CAPT and CAW must fit to. To illustrate the increase in the number of sub-aperture separation baselines, example CANARY and AOF covariance maps are shown in Figure 5.9. These covariance maps have been analytically generated for a 2-NGS configuration. They both show a layer at the integer baselines that correspond to altitudes of 0 km and $h_{\max}/2$. Each layer has $r_0 = 0.1$ m and $L_0 = 25$ m. The AOF has an increased spatial scale compared to CANARY. This makes fitting to AOF data much more computationally intensive. However, for optical turbulence profiling, it was shown in Section 3.7.2 that CAPT can efficiently handle AOF data.

In Figure 5.9b, both SHWFSs have dimensions of 40×40 and a total of 1240 active sub-apertures (see Section 2.2.2). However, within the GALACSI dataset, there was a custom

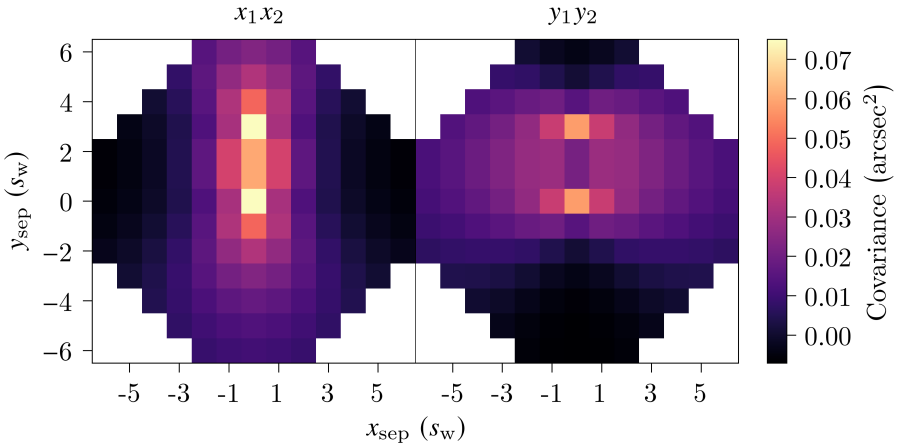

(a) Spatial scale of a covariance map from CANARY.

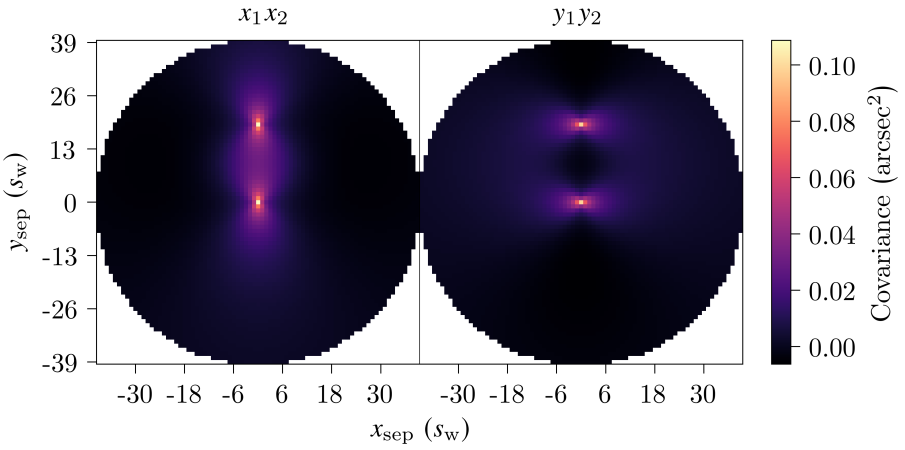

(b) Spatial scale of a covariance map from AOF GALACSI.

Figure 5.9: Analytically generated 2-NGS covariance map for CANARY (7×7 SHWFSs) and AOF GALACSI (40×40 SHWFSs). They both show a layer at the integer baselines that correspond to altitudes of 0 and $h_{\max}/2$. Each layer has $r_0 = 0.1\,\text{m}$ and $L_0 = 25\,\text{m}$.

pupil mask for each observation. There are a number of possible reasons for why GALACSI had a reduced number of active sub-apertures: sub-aperture light paths are being blocked by Deformable Secondary Mirror (DSM; see Section 2.2.3) struts; the Charge Coupled Device (CCD; see Section 2.2.2) has recorded a low number of photons; the DSM is not able to perform wavefront correction at certain sub-aperture locations (the source of this might be a faulty actuator). The GALACSI dataset did not state the reason for the additional inactive sub-apertures. Inactive sub-apertures were often found in the inner and outer ring of the pupil mask. To have a fixed telescope diameter, D, we set the outer 2 sub-apertures in every observation as inactive. This reduced D from 8.2 m to 7.38 m. It follows that the maximum observable altitude was reduced from 14 to 12.775 km. In each observation, the same pupil mask was applied to every SHWFS. The pupil mask from 17/06/2017 at 06:59:49 is shown in Figure 5.10.

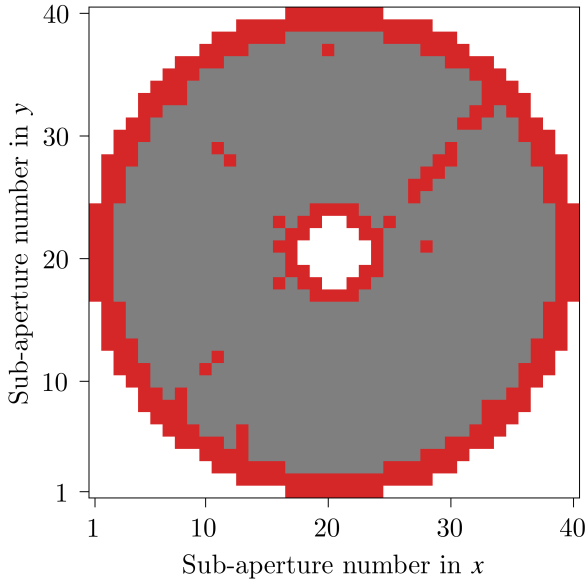

Figure 5.10: AOF GALACSI pupil mask from 17/06/2017 at 06:59:49. Here we show sub-apertures that are active (grey), inactive (red) and outside of the telescope light-path (white). Inactive sub-apertures have reduced the number of active sub-apertures from 1240 to 939.

In Section 5.1.2 the results from CANARY indicated that CAW wind velocity profiling is optimised when it is used to study a single temporal offset of approximately 0.05 s. If we assuming that this is for a maximum observable altitude of $h_{\max} = 24$ km then for GALACSI, this temporal offset scales to 0.027 s. The maximum expected wind speed is 100 m/s (see Section 4.3). Within the covariance map, a temporal offset of 0.027 s should see a 100 m/s layer have a displacement of 2.7 m. For the AOF this is roughly a sub-aperture separation distance of 13. Therefore, if the data from GALACSI is studied with a temporal offset of 0.027 s, the entire covariance map does not have to be fitted to. This improves the efficiency of the system. In Section 5.1.1 it was also shown that the covariance map ROI has optimal results when its width, W, is minimised. Therefore, for GALACSI in WFM, the ROI during CAW 2 and CAW 3 has a width and length equal to $W = 27$ and $L = 52$, respectively. The size of this ROI is demonstrated with on-sky data in Figure 5.11. The ROI in Figure 5.11 is for SHWFS centroids that have not been temporally offset. This covariance map ROI is calculated from LGS 1 and LGS 3 (see Figure 5.8) pseudo open-loop centroids (see Section 2.2.4). In Figure 5.11, there are noticeable layers at altitudes of approximately 0, 4 and 8 km.

5.2.2 Turbulence and wind velocity profiling

The AOF GALACSI dataset had observations from 15/06/2017, 17/06/2017, 18/06/2017, 13/07/2017 and 15/07/2017. These dates had 46, 118, 92, 14 and 41 observations, respectively, giving a total of 311. The AOF was being operated in closed-loop. Using the

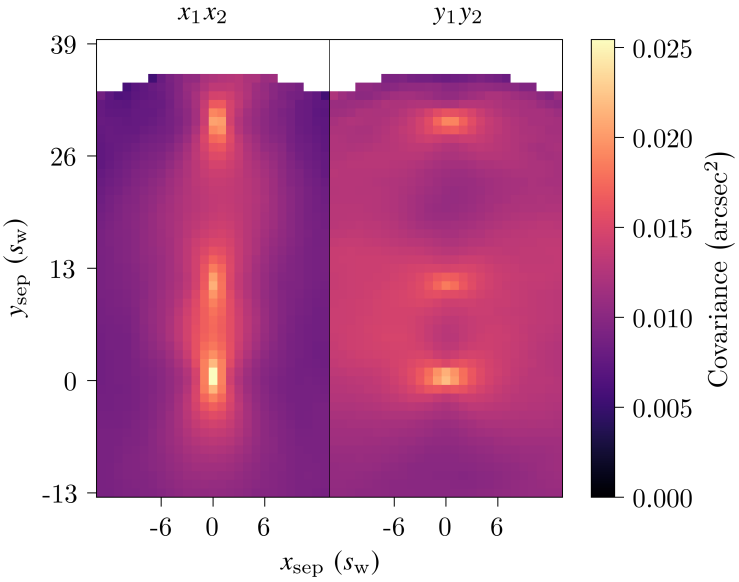

Figure 5.11: AOF GALACSI covariance map ROI calculated with pseudo open-loop centroids from LGS 1 and LGS 3. The ROI has a width and length of $W = 27$ and $L = 52$, respectively. The data is from 17/06/2017 at 06:59:49. Inactive sub-apertures (see Figure 5.10) have reduced the number sub-aperture separation baselines (see Figure 5.9b).

interaction matrix (see Section 2.2.4) the first step was to calculate the pseudo open-loop centroids for each observation. After this we were able to use CAPT to calculate the turbulence profiles along with SHWFS misalignments. We chose to fit 15 evenly-spaced layers between 0 and 12.6 km. By fitting 15 layers we could have a detailed measure of both the turbulence and wind velocity profile, while making sure CAW had sufficient time to process all 311 observations. Optimising the efficiency of CAW is the subject of a future investigation.

During CAPT 1 and CAPT 2, the ROI had $W = 1$ and $L = n_{\text{d}}$, where n_{d} is the number of SHWFS sub-apertures in one dimension. So that there was enough spatial information to measure SHWFS misalignments, the ROI during CAPT 3 had $W = 3$ and $L = n_{\text{d}} + 1$. Table 5.7 shows the mean absolute SHWFS shift misalignment in x at each of the available dates. The corresponding results for the shift misalignment in y are given in Table 5.8. The SHWFS rotational misalignment results are in Table 5.9. Without accounting for SHWFS misalignments, we would expect the measured misalignments to degrade the turbulence profile measurement by a mean logarithmic deviation of approximately $F_{\text{md}} = 0.1$ (see Section 3.4). After studying Figure 5.11, it is in fact possible to see the slight rotational misalignment that is outlined in Table 5.9. Both SHWFS 1 and SHWFS 3 have a measured rotation of 1.82°. If both SHWFSs are rotated in the same direction then this is equivalent to changing the GS position angle, γ. The rotational misalignment is particularly noticeable at the highest visible layer, that should be centred along $x_{\text{sep}} = 0$.

The observations from 17/06/2017 and 18/06/2017 were recorded over roughly 10 hours. We can therefore use these observations to visualise how the turbulence and wind velocity

Table 5.7: Mean absolute SHWFS shift in x, in units of metres conjugate to the telescope pupil. Misalignment results are from using CAPT to fit to on-sky AOF GALACSI cross-covariance arrays. SHWFS 4 is the zeroth point for all SHWFS shift misalignments.

	SHWFS 1	SHWFS 2	SHWFS 3	SHWFS 4
15/06/2017	0.04	0.04	0.02	0.00
17/06/2017	0.04	0.00	0.05	0.00
18/06/2017	0.01	0.01	0.00	0.00
13/07/2017	0.00	0.02	0.01	0.00
15/07/2017	0.00	0.01	0.01	0.00

Table 5.8: Mean absolute SHWFS shift in y, in units of metres conjugate to the telescope pupil. Misalignment results are from using CAPT to fit to on-sky AOF GALACSI cross-covariance arrays. SHWFS 4 is the zeroth point for all SHWFS shift misalignments.

	SHWFS 1	SHWFS 2	SHWFS 3	SHWFS 4
15/06/2017	0.00	0.00	0.02	0.00
17/06/2017	0.02	0.01	0.00	0.00
18/06/2017	0.00	0.01	0.00	0.00
13/07/2017	0.00	0.02	0.01	0.00
15/07/2017	0.00	0.02	0.01	0.00

Table 5.9: Mean absolute degree of SHWFS rotation. Misalignment results are from using CAPT to fit to on-sky AOF GALACSI cross-covariance arrays.

	SHWFS 1	SHWFS 2	SHWFS 3	SHWFS 4
15/06/2017	0.80	1.20	1.89	1.20
17/06/2017	1.82	1.62	1.82	1.68
18/06/2017	1.38	1.67	1.13	0.73
13/07/2017	0.53	1.35	0.50	0.91
15/07/2017	1.43	0.60	0.78	0.89

profiles change during an evening. These atmospheric parameters directly influence the isoplanatic angle, θ_0 (see Section 2.2.1.3), and the coherence time, τ_0 (see Section 2.2.5). Figure 5.12 shows the results from 17/06/2017. To highlight features, the 118 observations have been binned to a time resolution of 10 minutes. The 43 turbulence profiles shown are the mean of the measured turbulence profiles within each bin. Figure 5.11 shows notable layers at roughly 0, 4 and 8 km, and these are clearly visible at 7 UTC in Figure 5.12.

For each observation, CAW was used to fit to a single temporal offset of 0.027 s (see Section 5.2.1). To be consistent with the results in Section 5.1.2, wind velocity measurements were validated (see Section 4.3) using measurements from a single temporal offset of 0.02 s. During CAW wind velocity profiling, each of the fitted layers runs its altitude, h^{m}, as a free parameter. To illustrate the wind speed profile, we assume that each layer retains its altitude width defined during CAPT (in this case 900 m). This causes some of the wind speed measurements to overlap. In Figure 5.12, the mean wind speed is calculated at any of these overlapping altitudes. The wind velocity profiles then underwent the same binning process as above and the results are shown in Figure 5.12. A wind speed measurement of 0 m/s indicates that the layer fitted at this altitude has not been validated. However,

Table 5.10: ECMWF compared to on-sky AOF GALACSI measurements from using CAW to study a temporal offset of 0.027 s. ECMWF wind speeds are taken as the nearest neighbours to the measured altitudes.

	R_{w}	B (m/s)	A_{rms} (m/s)
ECMWF	0.50 ± 0.01	-3.7 ± 0.3	7.2 ± 0.3

CAW has managed to track all of the layers with the strongest turbulence, i.e. by studying the top and middle plots of Figure 5.12, the layers with the strongest turbulence always have a wind speed measurement. The corresponding values for θ_0 and τ_0 are shown in the bottom of Figure 5.12. These values are limited by the fact that we are unable to measure the strength and velocity of any turbulent layers above 12.775 km (see Section 5.2.1).

Figure 5.12 is repeated in Figure 5.13 but with the results from 18/06/2017. The 92 observations have been binned to a 10 minute resolution, giving a total of 43 turbulence and wind velocity profiles. CAW has again managed to track the strongest layers of turbulence. Compared to Figure 5.12, Figure 5.13 shows larger changes in both θ_0 and τ_0. The turbulence strength and wind speed are relatively low at 9 UTC, resulting in better seeing conditions. This demonstrates how CAPT and CAW can be used as a basis for selecting science targets.

The dates from AOF GALACSI did not overlap with observations from the Stereo-SCIDAR instrument at Paranal (Osborn et al., 2018). The other site monitoring instruments at Paranal were also offline during these dates. We were therefore unable to compare our turbulence profile measurements with any other instrument. However, we were able to compare our wind speed profile measurements to the ECMWF. The AOF GALACSI dataset did not come with the telescope position information required to compare wind direction profiles. In Figure 5.14a, we show the wind speed scatter plot between ECMWF and the measurements from CAW. ECMWF wind speeds are taken as the nearest neighbours to the measured altitudes from CAW. In Figure 5.14a, it can be seen that the trend is for faster wind speeds to be at higher altitudes. The results in Figure 5.14a are quantified in Table 5.10.

The layers fitted during AOF GALACSI and CANARY data analysis had altitude widths of 0.9 and 4 km, respectively. This will result in AOF GALACSI measuring more layers with lower strengths and so we expect AOF GALACSI to fit fewer wind velocities (see Section 4.4). This is reflected in Table 5.10 by the fraction of validated wind velocity candidates, R_{w}. Table 5.10 and Figure 5.14a show a bias to lower wind velocity measurements from CAW. The AOF has dome turbulence and so we expect a wind velocity bias at the ground. At higher altitudes, the most likely cause of this bias is wind shear (see Section 4.2). Turbulent layers above the maximum observable altitude might also be appearing in the temporally offset covariance map, negatively influencing CAW wind velocity measurements. To better visualise this bias, the probability density function from Figure 5.14a is shown in Figure 5.14b. This was calculated using a Gaussian kernel density estimate.

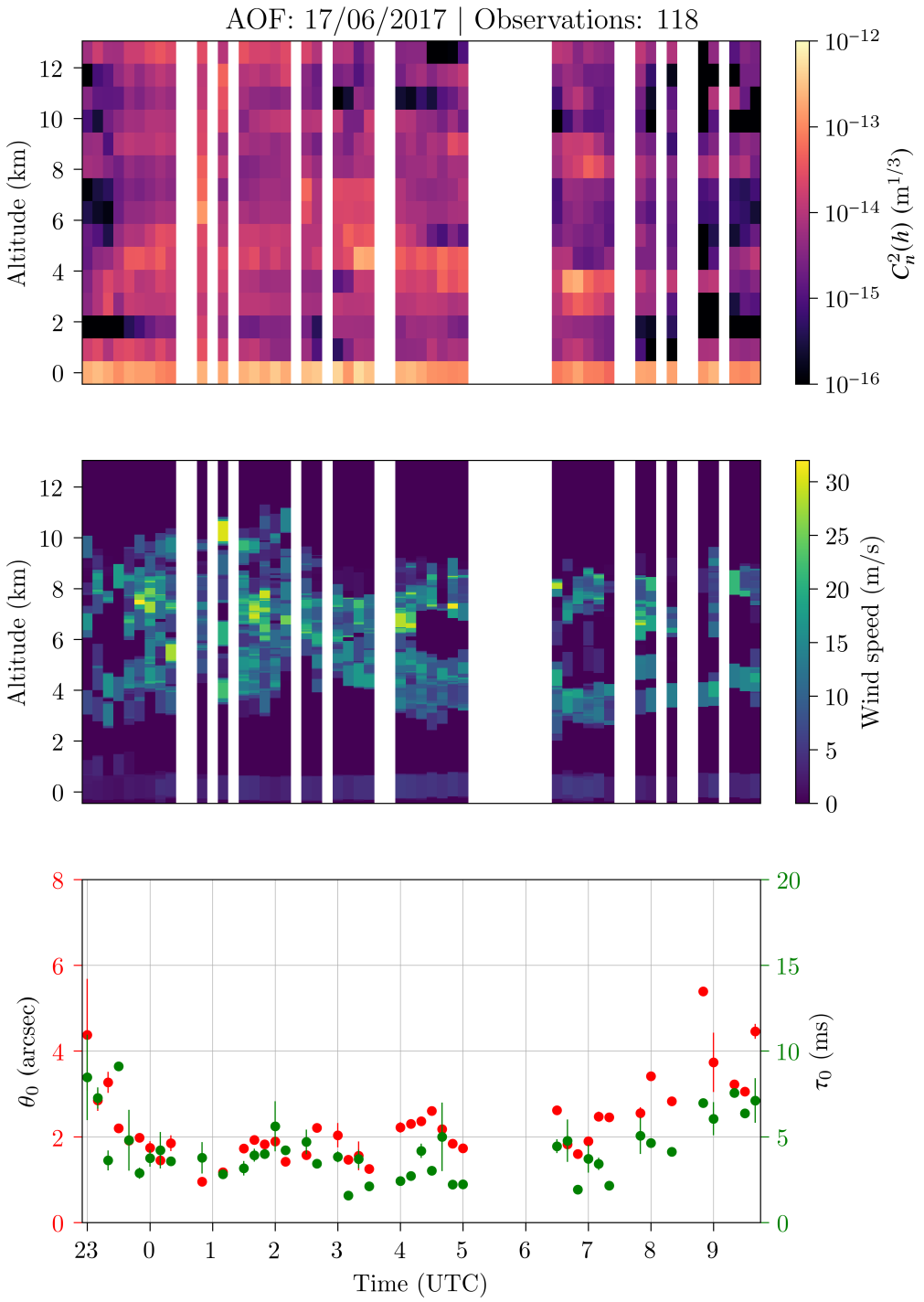

Figure 5.12: Optical turbulence (top) and wind velocity (middle) profiles from the AOF GALACSI instrument on 17/06/2017. During turbulence profiling, 15 evenly-spaced layers were fitted from 0 to 12.6 km. The highest observable altitude was 12.775 km. The isoplanatic angle, θ_0, and the coherence time, τ_0, evolve with these changing profiles (bottom). The profiles from 118 observations have been binned to a 10-minute resolution and the mean calculated, giving a total of 43 profiles. The binned profiles have been used to calculate the mean and standard error values for θ_0 and τ_0.

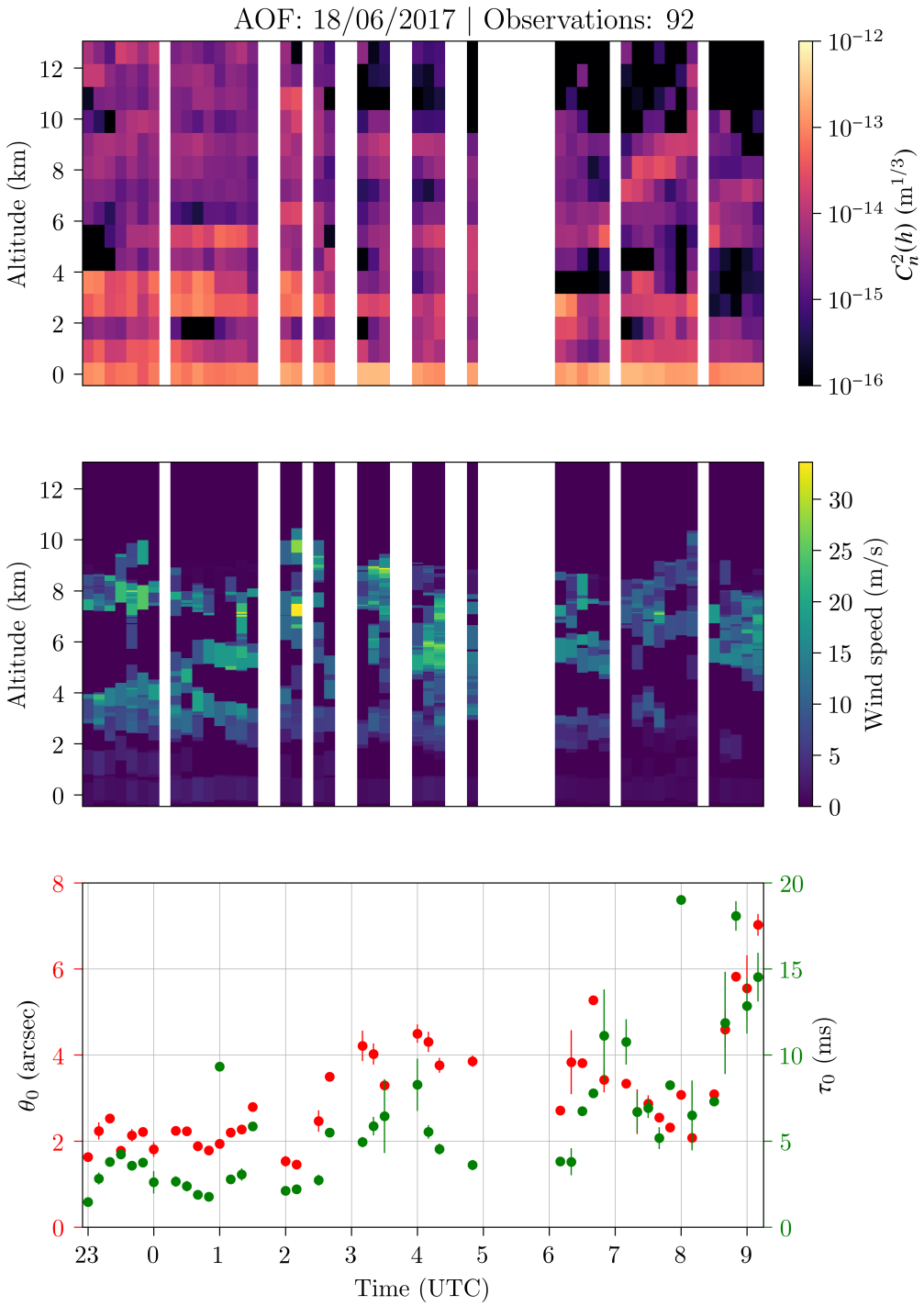

Figure 5.13: Optical turbulence (top) and wind velocity (middle) profiles from the AOF GALACSI instrument on 18/06/2017. During turbulence profiling, 15 evenly-spaced layers were fitted from 0 to 12.6 km. The highest observable altitude was 12.775 km. The isoplanatic angle, θ_0, and the coherence time, τ_0, evolve with these changing profiles (bottom). The profiles from 92 observations have been binned to a 10-minute resolution and the mean calculated, giving a total of 43 profiles. The binned profiles have been used to calculate the mean and standard error values for θ_0 and τ_0.

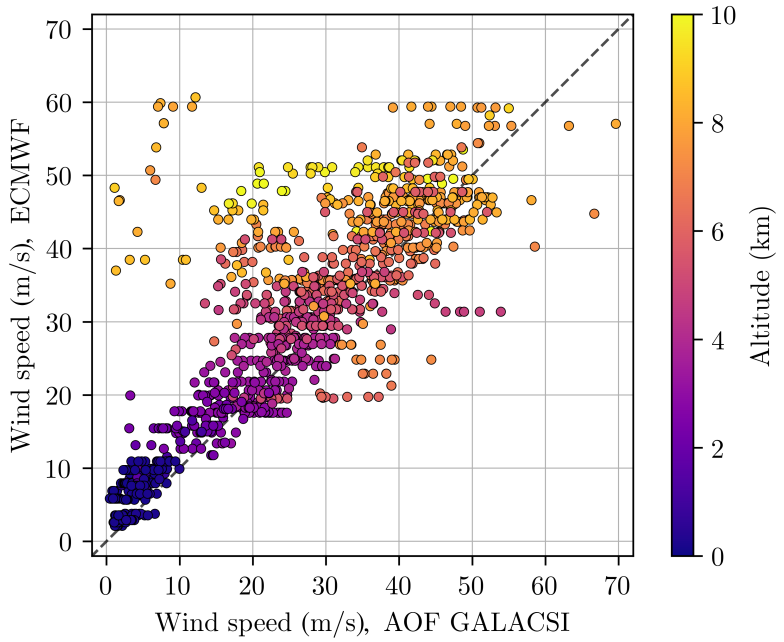

(a) Wind speed scatter plot between AOF GALACSI and ECMWF.

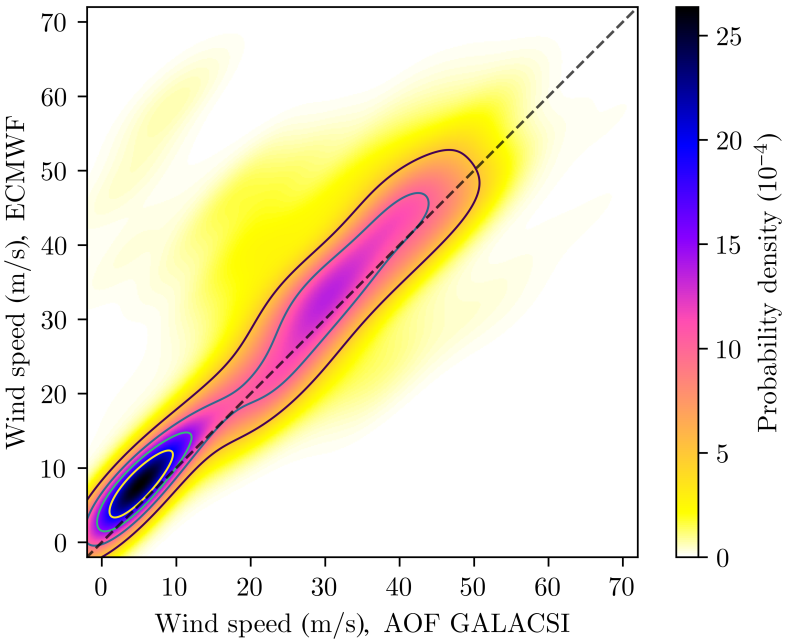

(b) Wind speed probability density function between AOF GALACSI and ECMWF.

Figure 5.14: Comparison between ECMWF and the wind speed measurements from applying CAW to the AOF GALACSI dataset. CAW was used to study a temporal offset of 0.027 s. A total of 311 observations have been studied, giving a total of 1,379 wind velocity measurements. ECMWF wind speeds are taken as the nearest neighbours to the measured altitudes. The black broken lines plot equal wind speeds.

5.2.3 Acknowledgements

The VLT is operated by ESO on Cerro Paranal in the Atacama Desert. The AOF GALACSI data was made available by the Pontificia Universidad Católica de Chile.

5.3 Summary

CAPT and CAW have been used to measure turbulence and wind velocity profiles from CANARY, the AO demonstrator for ELT-scale technologies at the 4.2 m WHT, La Palma. We have also applied these algorithms to on-sky data from the AOF GALACSI instrument, an AO module for the 8.2 m Yepun telescope at the VLT, Paranal.

Measurements from on-sky CANARY data showed that its SHWFSs had slight misalignments. Results from simulated and on-sky CANARY data showed that the optimal covariance map ROI has a width of $W = 1$. Comparing the measured optical turbulence profiles to contemporaneous measurements from Stereo-SCIDAR indicated that CAPT is optimised when fitting to a covariance map ROI instead of a covariance matrix. For the on-sky optical turbulence profiles, covariance matrix and map ROI CAPT measured F_{md} to be 0.46 ± 0.04 and 0.38 ± 0.04, respectively.

On-sky CANARY wind speed profiling results from CAW were compared against wind speed profiles from Stereo-SCIDAR and the ECMWF. In both comparisons, the root mean square deviation, A_{rms}, was minimised when studying a single temporal offset at $\Omega = 8$. This minimum suggested that, for CANARY, 0.05 s is the optimal temporal offset for frozen-flow to describe the wind velocity profile. When compared to Stereo-SCIDAR, $A_{\mathrm{rms}} = 3.5 \pm 0.3\,\mathrm{m/s}$ and the bias was equal to $B = -0.2 \pm 0.4\,\mathrm{m/s}$. When compared to the ECMWF, $A_{\mathrm{rms}} = 4.0 \pm 0.3\,\mathrm{m/s}$ and $B = -0.7 \pm 0.3\,\mathrm{m/s}$.

Large on-sky datasets from AOF GALACSI were studied using CAPT and CAW. The results were used to show the evolution of turbulence and wind speed profiles at the VLT. Measurements from VLT site monitors were not available for the dates we had so we could not compare our turbulence profile measurements to a separate instrument. However, we were able to compare our wind speed profiles to the ECMWF. After studying 311 observations, A_{rms} and B were calculated to be $7.2 \pm 0.3\,\mathrm{m/s}$ and $-3.7 \pm 0.3\,\mathrm{m/s}$, respectively. Due to dome turbulence there was an expected bias at the ground. The bias at higher altitudes is mainly attributed to wind shear. However, with the maximum observable altitude being 12.775 km, there is also the possibility that unmeasured layers are appearing in the covariance map after a temporal offset has been applied. CAW is a least squares fitting algorithm and so this will be negatively influencing the results.

— 6 —

Conclusions

The subject of this thesis has been the development of modified SLOpe Detection And Ranging (SLODAR) techniques for both turbulence and wind velocity profiling. We have concentrated on SLODAR-based techniques because they require Adaptive Optics (AO) telemetry and are therefore applicable to instruments being designed for the upcoming generation of Extremely Large Telescopes (ELTs). These techniques have been made into open-source software packages that are referred to as CovAriance Parametrisation of optical Turbulence and SHWFS misalignments (CAPT) and CovAriance parametrisation of Wind velocity (CAW). The measurements from CAPT and CAW enable AO system control techniques that can significantly improve image resolution and the smart scheduling of science cases. In this chapter we conclude our findings and discuss future work.

6.1 Turbulence profiling

The initial focus was developing an algorithm for measuring the optical turbulence profile along with Shack-Hartmann Wavefront Sensor (SHWFS) misalignments. The algorithm we developed is referred to as CAPT and it was written to be applicable to all tomographic AO systems. It was shown that by using CAPT, SHWFS misalignments can be successfully measured when analytically fitting to either a covariance matrix or a covariance map Region of Interest (ROI). The accuracy of covariance matrix and map ROI optical turbulence profiling was tested using simulated data from CANARY, an AO demonstrator for ELT-scale technologies on the 4.2 m William Herschel Telescope (WHT), La Palma. The simulation results indicated that CAPT is able to more accurately measure the turbulence profile when fitting to a covariance map ROI instead of a covariance matrix. This was attributed to the covariance map ROI only considering sub-aperture separations over which turbulence profile information is primarily projected. It is believed that by averaging SHWFS cross-covariance measurements as a function of baseline, the turbulence profile in the covariance map ROI has a higher Signal-to-Noise Ratio (SNR) than in the covariance matrix. We went on to show that CAPT is applicable to both Natural Guide Star (NGS) and Laser Guide Star (LGS) analysis.

CAPT computational efficiency was demonstrated for both the covariance matrix and the covariance map ROI. Three different scales of AO system were considered: CANARY on

the 4.2 m WHT, La Palma; the Adaptive Optics Facility (AOF) on the 8.2 m Yepun telescope at the Very Large Telescope (VLT), Paranal; and an instrument designed for the 39 m European ELT, Cerro Armazones. Fewer calculations are required when analytically generating a covariance map ROI. It was shown that fitting to the covariance map ROI improves the efficiency of an ELT-scale system by almost two orders of magnitude. Covariance map ROI analysis was therefore shown to be the most accurate as well as the fastest fitting technique. This is a significant result because optimised ELT performance will require efficient, high-precision measurements of the optical turbulence profile.

CAPT was first demonstrated on-sky using NGS CANARY data from 2014. It was shown that the CANARY SHWFSs had slight misalignments. The optical turbulence profile measurements were compared to contemporaneous measurements from the Stereo-SCIDAR instrument that was being operated on the 2.5 m Isaac Newton Telescope (INT). When compared to Stereo-SCIDAR, turbulence profiles from covariance matrix and map ROI fitting had a mean logarithmic deviation, F_{md}, of 0.46 ± 0.04 and 0.38 ± 0.04, respectively. It was concluded that CAPT is able to more accurately measure the turbulence profile when fitting to a covariance map ROI instead of a covariance matrix.

CAPT was then applied to LGS datasets from the Ground Atmospheric Layer Adaptive Corrector for Spectroscopic Imaging (GALACSI) instrument at the AOF. Two example dates were used to show how the turbulence profile can evolve over 10 hours and how these changes influence the isoplanatic angle. To verify the optical turbulence profiles from the AOF, there are ongoing discussions for a future campaign to run our fitting algorithms alongside the Stereo-SCIDAR instrument at Paranal.

Neither CANARY or the AOF have the spatial scale to accurately resolve the outer scale profile. Any outer scale measurement would be unrepresentative and so we did not fit this parameter during CAPT. For its expected values, the outer scale profile has little to no effect on both CANARY and AOF turbulence profiling. However, this might not be true for an ELT-scale system. An investigation is needed into the influence of the outer scale on ELT turbulence profiling. If the outer scale profile has to be fitted then this will increase the CAPT fitting times presented. To prepare for this possibility, there is future work planned for CAPT to be upgraded with parallel computing functionality.

6.2 Wind velocity profiling

We have introduced a novel technique for wind velocity profiling using SLODAR data analysis. This technique is referred to as CAW. In this study, CAW relied on CAPT for parameter estimation. By introducing a time delay between SHWFS cross-covariance measurements, a temporally offset covariance map array can be calculated. Using the information from CAPT, CAW can iteratively fit to this array by using an analytical model for sub-aperture covariance. To perform this 2D least-squares fit, each analytically generated layer runs its altitude and baseline as a free parameter. The displacement of each layer can then be used to calculate its velocity.

We studied the effect of wind shear and developed a theoretical model for how it can influence wind velocity measurements from CAW. Using the European Centre for Medium-Range Weather Forecasts (ECMWF), we were able to show that wind shear is more likely to have a significant effect at higher altitudes. Simulated CANARY data was used to test CAW. It was shown that CAW can accurately measure the wind velocity profile and that it is applicable to both NGS and LGS analysis.

CAW was demonstrated on-sky using the same NGS CANARY data that was used by CAPT during the optical turbulence profiling study. The results were compared against contemporaneous wind velocity profiles from the ECMWF and Stereo-SCIDAR. If the ECMWF and Stereo-SCIDAR are assumed to be the profile truth, the optimal temporal offset was found to be approximately 0.05 s. At this temporal offset, the fraction of validated wind velocity measurements, R_{w}, was 0.84 ± 0.03. When compared to Stereo-SCIDAR, the root mean square deviation, A_{rms}, and bias, B, were 3.5 ± 0.3 and -0.2 ± 0.4, respectively. When compared to the ECMWF, $A_{\mathrm{rms}} = 4.0 \pm 0.3$ and $B = -0.7 \pm 0.3$. The negative bias was attributed to dome turbulence and wind shear.

We went on to apply CAW to the AOF GALACSI dataset. Two example dates were used to show how the wind speed profile can evolve over 10 hours and how these changes influence the coherence time. The wind speed profile measurements were compared against the ECMWF and we calculated R_{w}, B and A_{rms} to be 0.50 ± 0.01, $-3.7 \pm 0.3\,\mathrm{m/s}$ and $7.2 \pm 0.3\,\mathrm{m/s}$, respectively. The AOF SHWFSs have more sub-apertures compared to CANARY, resulting in more sub-aperture separation baselines. This allowed us to fit more layers with a smaller altitude width, which meant there were more layers of a lower relative strength. The simulation results showed that layers of a lower relative strength are more likely to be fitted unsuccessfully. For this reason, we expected the fraction of validated wind velocity measurements, R_{w}, to be less than the results from CANARY. A further attributing factor was the maximum observable altitude being 12.775 km. This meant that after applying a temporal offset, turbulent layers above the maximum observable altitude might now appear in the target covariance map array. There is no system in place to account for this and so this scenario will complicate the CAW fitting process. This scenario along with wind shear helped explain the bias at high altitudes. The bias at the ground was attributed to dome turbulence.

As mentioned previously, there are ongoing discussions to run our fitting algorithms alongside the Stereo-SCIDAR instrument at Paranal. This will allow for high-resolution measurements from Stereo-SCIDAR to be compared against the results from both CAPT and CAW. We have to improve the efficiency of CAW before it can process wind velocity profiles in real-time. As with CAPT, there is future work planned for CAW to be upgraded with parallel computing functionality. Having this capability means we will be able to quickly process large datasets, allowing us to verify the optimal temporal offset for all AO systems. Improving the efficiency of CAW will also allow us to fit more layers during AOF and ELT data processing. This will help eradicate the problem of wind shear. The goal is to improve the efficiency of CAW such that it can be used by the ELTs for real-time wind velocity profiling.

Bibliography

Assémat, F., Wilson, R. W., and Gendron, E. (2006). Method for simulating infinitely long and non stationary phase screens with optimized memory storage. *Prog. Optics Mon. Not. R. Astron. Soc. Appl. Opt. Appl. Opt. Waves Random Media Astron. Astrophys. A. Tokovinin Publ. Astron. Soc. Pac. D. L. Fried Statistics of a Geometric Representation of Wavefront Distortion J. Opt. Soc. Am. OPTICS EXPRESS.*

Bardou, L. (2018). The eso wendelstein laser guide star unit.

Bardou, L., Gendron, É., Rousset, G., Gratadour, D., Basden, A. G., Bonaccini Calia, D., Buey, J.-T. M., Centrone, M., Chemla, F., Gach, J.-L., Geng, D., Hubert, Z., Laidlaw, D. J., Morris, T. J., Myers, R. M., Osborn, J., Reeves, A. P., Townson, M. J., and Vidal, F. (2018). Error breakdown of ELT-elongated LGS wavefront-sensing using CANARY on-sky measurements.

Basden, A. G., Bardou, L., Buey, J.-T. M., Castro-Almazán, J. A., Centrone, M., Chemla, F., Bonaccini Calia, D., Gach, J.-L., Gendron, É., Geng, D., Hubert, Z., Laidlaw, D. J., Lombardi, G., Morris, T. J., Myers, R. M., Osborn, J., Reeves, A. P., Rousset, G., Sevin, A., Townson, M. J., and Vidal, F. (2018). Closed loop operation with extremely elongated LGS spots in CANARY Phase D.

Beckers, J. M. (1988). Increasing the size of the isoplanatic patch with multiconjugate adaptive optics. In *Very Large Telescopes and their Instrumentation*, pages 693–703.

Beghi, A., Cenedese, A., and Masiero, A. (2008). Stochastic realization approach to the efficient simulation of phase screens. *Journal of the Optical Society of America A.*

Bouchez, A. H., Angeli, G. Z., Ashby, D. S., Bernier, R., Conan, R., McLeod, B. A., Quiros-Pacheco, F., and van Dam, M. A. (2018). An overview and status of gmt active and adaptive optics. volume 10703, pages 10703 – 10703 – 16.

Boyer, C. (2018). Adaptive optics program at tmt. volume 10703, pages 10703 – 10703 – 13.

Butterley, T., Wilson, R. W., and Sarazin, M. (2006). Determination of the profile of atmospheric optical turbulence strength from SLODAR data. *Monthly Notices of the Royal Astronomical Society.*

Calçada, L. (2014). Artist's impression of the european extremely large telescope.

Chauvin, G., Lagrange, A.-M., Dumas, C., Zuckerman, B., Mouillet, D., Song, I., Beuzit, J.-L., and Lowrance, P. (2004). A giant planet candidate near a young brown dwarf. *Astronomy & Astrophysics*.

Clampin, M. (2008). The James Webb Space Telescope (JWST). *Advances in Space Research*.

Cortés, A., Neichel, B., Guesalaga, A., Osborn, J., Rigaut, F., and Guzman, D. (2012). Atmospheric turbulence profiling using multiple laser star wavefront sensors. *Monthly Notices of the Royal Astronomical Society*.

ESO (2017). Comparison of domes for future large telescopes.

Farley, O. J., Osborn, J., Morris, T., Sarazin, M., Butterley, T., Townson, M. J., Jia, P., and Wilson, R. W. (2018). Representative optical turbulence profiles for ESO Paranal by hierarchical clustering. *Monthly Notices of the Royal Astronomical Society*.

Fried, D. L. (1965). Statistics of a Geometric Representation of Wavefront Distortion. *Journal of the Optical Society of America*.

Gendron, E., Vidal, F., Brangier, M., Morris, T., Hubert, Z., Basden, A., Rousset, G., Myers, R., Chemla, F., Longmore, A., Butterley, T., Dipper, N., Dunlop, C., Geng, D., Gratadour, D., Henry, D., Laporte, P., Looker, N., Perret, D., Sevin, A., Talbot, G., and Younger, E. (2011). MOAO first on-sky demonstration with CANARY. *Astronomy & Astrophysics*.

Greenwood, D. P. (1977). Bandwidth specification for adaptive optics systems. *Journal of The Optical Society of America*, 67:390–393.

Guesalaga, A., Neichel, B., Correia, C. M., Sauvage, J.-F., Fusco, T., Osborn, J., Butterley, T., and Masciadri, E. (2016). Online estimation of the wavefront outer scale profile from adaptive optics telemetry. *Monthly Notices of the Royal Astronomical Society*, 465(2):1984–1994.

Guesalaga, A., Neichel, B., Cortés, A., Béchet, C., and Guzmán, D. (2014). Using the C_{n}^2 and wind profiler method with wide-field laser-guide-stars adaptive optics to quantify the frozen-flow decay. *Monthly Notices of the Royal Astronomical Society*.

Haiden, T., Janousek, M., Bauer, P., Bidlot, J., Ferranti, L., Hewson, T., Prates, F., Richardson, D. S., and Vitart, F. (2014). Evaluation of ecmwf forecasts, including 2013-2014 upgrades. *Research and Forecast Department*.

Haiden, T., Janousek, M., Bidlot, J., Ferranti, L., Prates, F., Vitart, F., Bauer, P., and Richardson, D. S. (2017). Evaluation of ecmwf forecasts, including 2016-2017 upgrades. *Forecast Department*.

Hardy, J. W. (1998). *Adaptive optics for astronomical telescopes*.

Hirsch, E., Agassi, E., and Koren, I. (2011). A novel technique for extracting clouds base height using ground based imaging. *Atmospheric Measurement Techniques*.

Horálek, P. (2018). Four lasers light up paranal.

Jackson, K., Correia, C., Lardière, O., Andersen, D., and Bradley, C. (2015). Linear prediction of atmospheric wave-fronts for tomographic adaptive optics systems: modelling and robustness assessment. *Optics Letters*.

Janson, M., Bergfors, C., Goto, M., Brandner, W., and Lafrenière, D. (2010). Spatially resolved spectroscopy of the exoplanet HR 8799 c. *Astrophysical Journal Letters*.

Jia, P., Osborn, J., Kong, L., Laidlaw, D., Li, C., Farley, O., and Xue, G. (2018). Modelling synthetic atmospheric turbulence profiles with temporal variation using Gaussian mixture model. *Monthly Notices of the Royal Astronomical Society*.

Jones, E., Oliphant, T., Peterson, P., et al. (2001). SciPy: Open source scientific tools for Python. [Online; accessed <today>].

Kamphues, F. (2016). Pillars of light atop Paranal.

Kolb, J., Marchetti, E., Schneller, D., Sarazin, M., and Cirasuolo, M. (2015). Relevant atmospheric parameters for e-elt ao analysis and simulations, eso-258292, version 2. In *E-ELT Technical Archive*.

Kolmogorov, A. (1941). The local structure of turbulence in incompressible viscous fluid for very large Reynolds' numbers. *Doklady Akademiia Nauk SSSR*, 30:301–305.

Laidlaw, D. J., Osborn, J., Morris, T. J., Basden, A. G., Beltramo-Martin, O., Butterley, T., Gendron, E., Reeves, A. P., Rousset, G., Townson, M. J., and Wilson, R. W. (2018). Optimizing the accuracy and efficiency of optical turbulence profiling using adaptive optics telemetry for extremely large telescopes. *Monthly Notices of the Royal Astronomical Society*, 483(4):4341–4353.

Laidlaw, D. J., Osborn, J., Morris, T. J., Basden, A. G., Gendron, E., Rousset, G., Townson, M. J., and Wilson, R. W. (2019). Automated wind velocity profiling from adaptive optics telemetry. *Monthly Notices of the Royal Astronomical Society*, 491(1):1287–1294.

Lehtonen, J., Correia, C. M., and Helin, T. (2018). Limits of turbulence and outer scale profiling with non-kolmogorov statistics. volume 10703.

Levenberg, K. (1944). A method for the solution of certain non-linear problems in least squares. *Quarterly of Applied Mathematics*, 2(2):164–168.

Maire, J., Ziad, A., Borgnino, J., and Martin, F. (2007). Measurements of profiles of the wavefront outer scale using observations of the limb of the Moon. *Monthly Notices of the Royal Astronomical Society*.

Martin, O. (2014). *On-sky demonstration of multi-objet adaptive optics using laser guide stars by CANARY*. Thesis, Université Paris-Diderot - Paris VII.

Martin, O., Gendron, É., Rousset, G., and Vidal, F. (2012). Temporal convergence of phase spatial covariance matrix measurements in tomographic adaptive optics. In *Adaptive Optics Systems III*.

Martin, O. A., Correia, C. M., Gendron, E., Rousset, G., Vidal, F., Morris, T. J., Basden, A. G., Myers, R. M., Ono, Y. H., Neichel, B., and Fusco, T. (2016a). William herschel telescope site characterization using the moao pathfinder canary on-sky data. volume 9909, pages 9909 – 9909 – 15.

Martin, O. A., Gendron, É., Rousset, G., Gratadour, D., Vidal, F., Morris, T. J., Basden, A. G., Myers, R. M., Correia, C. M., and Henry, D. (2017). Wave-front error breakdown in laser guide star multi-object adaptive optics validated on-sky by Canary. *Astronomy & Astrophysics*.

Martin, O. A., M., C. C., Gendron, E. amd Rousset, G., Gratadour, D., Vidal, F., Morris, T. J., Basden, A. G., Myers, R. M., Neichel, B., and Fusco, T. (2016b). Psf reconstruction validated using on-sky canary data in moao mode. volume 9909, pages 9909 – 9909 – 13.

Masciadri, E., Lascaux, F., and Fini, L. (2013). MOSE: Operational forecast of the optical turbulence and atmospheric parameters at european southern observatory ground-based sites - i. overview and vertical stratification of atmospheric parameters at 0-20km. *Monthly Notices of the Royal Astronomical Society*.

Masciadri, E., Lascaux, F., Turchi, A., and Fini, L. (2017). Optical turbulence forecast: Ready for an operational application. *Monthly Notices of the Royal Astronomical Society*.

McDermid, R. M., Bacon, R., Bauer, S., Boehm, P., Boudon, D., Brau-Nogué, S., Caillier, P., Capoani, L., Carollo, C. M., Champavert, N., Contini, T., Daguisé, E., Delabre, B., Devriendt, J., Dreizler, S., Dubois, J., Dupieux, M., Dupin, J. P., Emsellem, E., Ferruit, P., Franx, M., Gallou, G., Gerssen, J., Guiderdoni, B., Hahn, T., Hofmann, D., Jarno, A., Kelz, A., Koehler, C., Kollatschny, W., Kosmalski, J., Laurent, F., Lilly, S. J., Lizon, J. L., Loupias, M., Manescau, A., Monstein, C., Nicklas, H., Parès, L., Pasquini, L., Pécontal-rousset, A., Pécontal, E., Pello, R., Petit, C., Picat, J. P., Popow, E., Quirrenbach, A., Reiss, R., Renault, E., Roth, M., Schaye, J., Soucail, G., Steinmetz, M., Stroebele, S., Stuik, R., Weilbacher, P., Wisotzki, L., Wozniak, H., and de Zeeuw, P. T. (2008). MUSE: A second-generation integral-field spectrograph for the VLT. In *ESO Astrophysics Symposia*.

Morris, T., Gendron, E., Basden, A., Beltramo-Martin, O., Osborn, J., Henry, D., Hubert, Z., Sivo, G., Gratadour, D., Chemla, F., Sevin, A., Cohen, M., Younger, E., Vidal, F., Wilson, R., Butterley, T., Bitenc, U., Reeves, A., and Bharmal, N. (2014). Canary phase b: on-sky open-loop tomographic lgs ao results. volume 9148, page 91481I.

Neichel, B., Fusco, T., and Conan, J.-M. (2009). Tomographic reconstruction for wide-field adaptive optics systems: Fourier domain analysis and fundamental limitations. *J. Opt. Soc. Am. A*, 26(1):219–235.

Newman, A. R. (1990). The Hubble Space Telescope. *Analytical Chemistry*.

Oberti, S., Kolb, J., Madec, P.-Y., Haguenauer, P., Le Louarn, M., Pettazzi, L., Guesalaga, A., Donaldson, R., Soenke, C., Jeram, B., Valles, M. S., Kiekebusch, M., Argomedo, J., La Penna, P., Paufique, J., Arsenault, R., Hubin, N., and Vernet, J. (2018). The ao in aof. volume 10703, pages 10703 – 10703 – 20.

Oliphant, T. (2006). NumPy: A guide to NumPy. USA: Trelgol Publishing. [Online; accessed <today>].

Ono, Y. H., Correia, C. M., Andersen, D. R., Lardière, O., Oya, S., Akiyama, M., Jackson, K., and Bradley, C. (2016). Statistics of turbulence parameters at Maunakea using the multiple wavefront sensor data of RAVEN. *Monthly Notices of the Royal Astronomical Society*.

Osborn, J., Butterley, T., Perera, S., Fohring, D., and Wilson, R. W. (2015). Observations of the dynamic turbulence above la palma using stereo-scidar. *Journal of Physics: Conference Series*, 595(012022).

Osborn, J., Butterley, T., Townson, M. J., Reeves, A. P., Morris, T. J., and Wilson, R. W. (2017). Turbulence velocity profiling for high sensitivity and vertical-resolution atmospheric characterization with Stereo-SCIDAR. *Monthly Notices of the Royal Astronomical Society*.

Osborn, J., Wilson, R., Butterley, T., Shepherd, H., and Sarazin, M. (2010). Profiling the surface layer of optical turbulence with SLODAR. *Monthly Notices of the Royal Astronomical Society*.

Osborn, J., Wilson, R. W., Butterley, T., Avila, R., Dhillon, V. S., Morris, T. J., and Shepherd, H. W. (2013). Stereo Scidar : Profiling Atmospheric Optical Turbulence With Improved Altitude Resolution. *Third AO4ELT Conference - Adaptive Optics for Extremely Large Telescopes Florence,*.

Osborn, J., Wilson, R. W., Sarazin, M., Butterley, T., Chacón, A., Derie, F., Farley, O. J., Haubois, X., Laidlaw, D., LeLouarn, M., Masciadri, E., Milli, J., Navarrete, J., and Townson, M. J. (2018). Optical turbulence profiling with Stereo-SCIDAR for VLT and ELT. *Monthly Notices of the Royal Astronomical Society*.

Paufique, J., Bruton, A., Glindemann, A., Jost, A., Kolb, J., Jochum, L., Le Louarn, M., Kiekebusch, M., Hubin, N., Madec, P.-Y., Conzelmann, R., Siebenmorgen, R., Donaldson, R., Arsenault, R., and Tordo, S. (2010). GRAAL: a seeing enhancer for the NIR wide-field imager Hawk-I. In *Adaptive Optics Systems II*.

Reeves, A. (2016). Soapy: an adaptive optics simulation written purely in Python for rapid concept development. In *Adaptive Optics Systems V*.

Roddier, F. (1999). *Adaptive optics in astronomy*. Cambridge University Press.

Schmidt, J. D. (2010). *Numerical Simulations of Optical Wave Propagation with examples in MATLAB*. Society of Photo-Optical Instrumentation Engineers (SPIE).

Schöck, M. and Spillar, E. J. (2007). Method for a quantitative investigation of the frozen flow hypothesis. *Journal of the Optical Society of America A*.

Shepherd, H. W., Osborn, J., Wilson, R. W., Butterley, T., Avila, R., Dhillon, V. S., and Morris, T. J. (2013). Stereo-SCIDAR: Optical turbulence profiling with high sensitivity using a modified SCIDAR instrument. *Monthly Notices of the Royal Astronomical Society*.

Sivo, G., Kulcsár, C., Conan, J.-M., Raynaud, H.-F., Gendron, É., Basden, A., Vidal, F., Morris, T., Meimon, S., Petit, C., Gratadour, D., Martin, O., Hubert, Z., Sevin, A., Perret, D., Chemla, F., Rousset, G., Dipper, N., Talbot, G., Younger, E., Myers, R., Henry, D., Todd, S., Atkinson, D., Dickson, C., and Longmore, A. (2014). First on-sky SCAO validation of full LQG control with vibration mitigation on the CANARY pathfinder. *Optics Express*.

Sivo, G., Turchi, A., Masciadri, E., Guesalaga, A., and Neichel, B. (2018). Towards an automatic wind speed and direction profiler for Wide Field adaptive optics systems. *Monthly Notices of the Royal Astronomical Society*.

Stuik, R., Bacon, R., Conzelmann, R., Delabre, B., Fedrigo, E., Hubin, N., Le Louarn, M., and Ströbele, S. (2006). GALACSI - The ground layer adaptive optics system for MUSE.

Tallon, M., Foy, R., and Vernin, J. (1992). 3-d wavefront sensing for multiconjugate adaptive optics. 42:517.

Tamai, R., Koehler, B., Cirasuolo, M., F., B.-M., Tuti, M., and Herrera, J. C. G. (2018). The eso's elt construction status. volume 10700, pages 10700 – 10700 – 11.

Tatarskii, V., I. (1961). Wave propagation in a turbulent medium. *New York : McGraw-Hill*, page 285.

Taylor, G. I. (1938). The Spectrum of Turbulence. *Proceedings of the Royal Society A - Mathematical, Physical and Engineering Sciences*.

Tokovinin, A. (2002). From Differential Image Motion to Seeing. *Publications of the Astronomical Society of the Pacific*.

Tokovinin, A. (2004). Seeing improvement with ground-layer adaptive optics. *Publications of the Astronomical Society of the Pacific*, 116(824):941–951.

Tyson, R. K. (2010). *Principles of Adaptive Optics*.

Vernin, J. and Roddier, F. (1973). Experimental determination of two-dimensional spatiotemporal power spectra of stellar light scintillation Evidence for a multilayer structure of the air turbulence in the upper troposphere. *J. Opt. Soc. Am.*

Vidal, F., Gendron, E., Brangier, M., Sevin, A., Rousset, G., and Hubert, Z. (2010). Tomography reconstruction using the learn and apply algorithm. *http://dx.doi.org/10.1051/ao4elt/201007001*.

Vidal, F., Gendron, É., Rousset, G., Morris, T., Basden, A., Myers, R., Brangier, M., Chemla, F., Dipper, N., Gratadour, D., Henry, D., Hubert, Z., Longmore, A., Martin, O., Talbot, G., and Younger, E. (2014). Analysis of on-sky MOAO performance of CANARY using natural guide stars. *Astronomy & Astrophysics*.

Villecroze, R., Fusco, T., Bacon, R., and Madec, P. Y. (2012). Psf reconstruction for muse in wide field mode. volume 8447, pages 8447 – 8447 – 15.

Wang, L., Schöck, M., and Chanan, G. (2008). Atmospheric turbulence profiling with slodar using multiple adaptive optics wavefront sensors. *Applied Optics*.

Wilson, R. W. (2002). SLODAR: Measuring optical turbulence altitude with a Shack-Hartmann wavefront sensor. *Monthly Notices of the Royal Astronomical Society*.

Wilson, R. W., Butterley, T., and Sarazin, M. (2009). The durham/eso slodar optical turbulence profiler. *Monthly Notices of the Royal Astronomical Society*, 399(4):2129–2138.

Ziad, A., Schö, M., Chanan, G. A., Troy, M., Dekany, R., Lane, B. F., Borgnino, J., and Martin, F. O. (2004). Comparison of measurements of the outer scale of turbulence by three different techniques. *Applied optics*.

Colophon

This thesis was typeset with LaTeX 2_ε. It was created using the memoir package, maintained by Lars Madsen, with the dash chapter style. The font used is Latin Modern, derived from fonts designed by Donald E. Kunith.